



Universidad de Granada

**MULTISCALE ANALYSIS OF MORPHODYNAMIC
PROCESSES IN ESTUARIES AND THEIR
INTEGRATION INTO DREDGING PROJECTS**

Miguel Ángel Reyes Merlo

Advisor: Manuel Díez Minguito

Programa de Doctorado de Dinámica de Flujos
Biogeoquímicos y sus Aplicaciones

November 2016

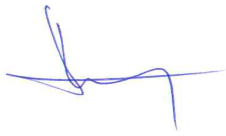
Editor: Universidad de Granada. Tesis Doctorales
Autor: Miguel Ángel Reyes Merlo
ISBN: 978-84-9163-072-2
URI: <http://hdl.handle.net/10481/44593>

El doctorando **Miguel Ángel Reyes Merlo** y el director de la tesis **Manuel Díez Minguito** garantizamos, al firmar esta tesis doctoral, que el trabajo ha sido realizado por el doctorando bajo la dirección de los directores de la tesis y hasta donde nuestro conocimiento alcanza, en la realización del trabajo, se han respetado los derechos de otros autores a ser citados, cuando se han utilizado sus resultados o publicaciones.

Granada, a 4 de noviembre de 2016

Director de la Tesis

Doctorando

A handwritten signature in blue ink, consisting of a stylized 'M' followed by a horizontal line and a vertical stroke.A handwritten signature in blue ink, featuring a large, circular flourish at the top and several loops below.

Fdo.: Manuel Díez Minguito

Fdo.: Miguel Ángel Reyes Merlo

A mi madre y a mi padre, a mis hermanos y a mi abuela, a mis buenos amigos.

A paradigm, in the more general sense, is the way we “see” the world—not in terms of our visual sense of sight, but in terms of perceiving, understanding, interpreting.

Stephen Covey

Acknowledgments

I have a lot to thank and to a lot of different people. For the purpose of being concise, I will try to focus only on professional aspects.

I am grateful to the Environmental Fluid Dynamics Group of the University of Granada for all the support received during these years and for giving me the opportunity to turn my scientific curiosity into facts. Thanks primarily to Miguel Ángel Losada, who believed in my abilities and taught me that high quality results can only be achieved with a thorough scientific knowledge.

Amongst the rest of the members, special mention to the following:

- Thanks to Montse Vílchez for the help and advice in the last stage of this Thesis, which has been, for me, the most demanding one so far.
- Thanks to Marian Serrano, my Thesis' travel mate, you made smoother the writing challenge.
- Thanks to Antonio Moñino for the scientific dialectics during these years.
- Thanks to Pedro Magaña for his patience and help with all the imaginable and unimaginable IT problems during this period. The fanciness of the figures of Chapter 2 is all his.
- Thanks to Miguel Ortega Sánchez for relying on me for the project *Dragaport*, for trusting me and being patient with my work, teaching me relevant aspects of management, and encouraging me to be efficient and concise. Without him, I would be probably still be coding my manuscript in Matlab right now.

I am also grateful to the Institute for Marine and Atmospheric research of Utrecht (IMAU), particularly the Coastal and Shelf Sea Dynamics Group for all their support during and after my research stay; not only in the scientific aspects, I have to point out. I would like to highlight Professor Huib de Swart, from whom I received great help in multiple aspects and improved my paradigm of regarding science.

Last but not least, to my advisor, Manuel Díez Minguito. It is difficult to find the appropriate words to thank you. You lead me through one of the most important "Chapters" of my life. What really matters is not the end, but the path. Thanks for walking with me. Oh and by the way... we did it!

Abstract

Estuaries are crucial areas from a socio-environmental point of view, being the ecosystem for a wide range of life forms, the economic foundation of many coastal nations, and the connection between land and open sea. Communities inhabiting these areas need to transport people and commodities by water, thus entailing the dredging of waterways to inland ports. Deepening of navigation channels in estuaries usually results in the alteration of tidal behavior and related morphodynamic processes. The knowledge of the spatio-temporal response of estuaries to dredging activities is still limited; therefore there is a real need to use and combine different methods and tools when exploring the effects of such interventions. It is the aim of this Thesis to enhance the understanding of the main morphodynamic processes involved in the dredging activities, and the implementation of multiple tools when assessing these projects in estuaries. This Thesis achieved the objective using data and field measurements in two Andalusian estuaries, where both the role of the forcings and the dredging strategies differ: the Guadalquivir estuary and the Punta Umbría inlet.

In the case of the Guadalquivir estuary, whose inland port belongs to the Spanish Port System, the presence of numerous stakeholders pose a challenge when managing dredging projects. The recent proposal to deepen the navigation channel confront the interests of different parties due to the possible environmental impacts in the system. This concern attains the effects of tides and freshwater discharge into the turbidity, saline intrusion and, generally, the ecological and chemical state of water masses. In the case of Punta Umbría inlet, the Regional Government of Andalusia manages the inland port. A database specifically designed to assess the dredging projects in these regional ports was used. The evaluation of all these dredging activities executed in the past twenty years pointed Punta Umbría as a particularly problematic port. Indeed, it has one of the highest average prices per intervention, where the volume of mobilized sediment in the navigation channels is the second highest.

The estuarine circulation and the tidal-fluvial interaction in the Guadalquivir estuary at multiple spatio-temporal scales was analyzed, especially regarding the possible implications of deepening into the salinity and suspended matter distributions. The salt flux driving mechanisms were discussed, and the exchange flow was identified and characterized by means of estimates of the effective vertical turbulent viscosity. Power-law relationships were obtained to assess the relative influence of tides, river flow, and wind conditions on the saline intrusion. Non-stationary analysis of observations was performed in terms of a short-time harmonic analysis and continuous wavelet transform. These analyses allowed for the evaluation of spatial and frequency-dependent responses in water levels, currents, tidal ellipse parameters, and related variables; revealing the dominant processes of the tidal-fluvial interaction affected by high discharges.

Empirical relationships between forcing agents in the Guadalquivir estuary were used to predict mid-term possible shifts, both in the saline intrusion and the subtidal water levels regimes, as a response to deepening the navigation channel. Due to the stochastic nature of the freshwater discharge and the saline intrusion, non-stationary distributions and Markov Chains were implemented. Deterministic models for the tidal motion, as well as heuristic methods and common regression models for the saline intrusion and subtidal levels, were combined

to predict the behavior of the variables. The simulations of different scenarios are based on Markov Chain Monte Carlo methods. Since the significance of the freshwater discharge in the estuarine morphodynamics is notable, a management scenario considering the expected freshwater discharge reduction for the next decades was also addressed.

Different scale and processes present the Punta Umbría inlet to the Guadalquivir estuary. In the past decades, three different navigation channels were dredged to ensure the operational capacity and security through the inlet to the inland port. Since the economic and environmental impacts are high, regional managers are demanding a more efficient alternative. Hydrodynamic measurements, and eighteen detailed bathymetries, were used. These allowed the identification and quantification of different states of the inlet regarding the dredging interventions and the morphological activity in the bed. To better understand bathymetric complexities and their interrelation to hydrodynamics, a numerical model was calibrated and validated. The relative influence of tides and waves was compared computing both the tidal and wave energy fluxes. The divergence of these energy fluxes was related to the morphological activity of the inlet. It was found that the locations with greater sedimentation tendency correspond to those with higher (negative) divergence in the energy fluxes. This Thesis proposed an efficient alternative to present channel designs, based on minimizing the divergence of the energy fluxes responsible of the sedimentation tendency in the inlet.

Resumen

Los estuarios son enclaves de un alto valor social y medioambiental, siendo la base para multitud de formas de vida, el pilar económico de muchas regiones costeras y el nexo de unión entre la tierra y el mar. Las poblaciones que habitan estos entornos necesitan del transporte marítimo para su mantenimiento, lo que implica la ejecución de canales de navegación hacia los puertos que estén en su interior. La profundización de estos canales de navegación en los estuarios normalmente conlleva una alteración del comportamiento de la marea y de distintos procesos morfodinámicos. El conocimiento de la respuesta tanto espacial como temporal de los estuarios frente a estas intervenciones de dragado es aún limitado; existiendo una necesidad real de emplear, y combinar, distintas técnicas y herramientas para conocer el efecto de dichas actividades. Por ello, el objetivo de esta Tesis es profundizar en el conocimiento de los principales procesos que se ven afectados por la actividades de dragado, implementando una amplia variedad de métodos a la hora de evaluar estos proyectos en estuarios. Para la consecución de objetivo, se han empleado datos y medidas de dos estuarios andaluces, en lo que tanto el papel de los forzamientos como las estrategias de dragado difieren: el estuario del Guadalquivir y la ría de Punta Umbría.

En el caso del estuario del Guadalquivir, en donde la Autoridad Portuaria que gestiona el puerto interior pertenece al Sistema Portuario Español, la presencia de multitud de agentes sociales, económicos y medioambientales hacen que la gestión del dragado sea una tarea compleja. La reciente propuesta para profundizar el canal de navegación ha supuesto un conflicto de intereses entre distintos sectores, debido al posible impacto medioambiental que ello implicaría sobre el estuario. La mayor preocupación se centra en los efectos que pueden tener la marea y la descarga de agua dulce sobre la turbidez, intrusión salina y, en general, el estado ecológico de las masas de agua. En el caso de la ría de Punta Umbría, los puertos interiores están gestionados por la Agencia Pública de Puertos de Andalucía. El estudio de todas las actividades de dragado llevadas a cabo en Andalucía durante los últimos veinte años, mediante una base de datos específicamente desarrollada para este fin, señala al de Punta Umbría como un puerto especialmente problemático. De hecho, se trata de un enclave en donde el coste medio por intervención es de los más altos, y en el que el volumen dragado en el canal de acceso es el segundo mayor de toda la Comunidad.

En este trabajo, se analiza la circulación estuarina y la interacción mareo-fluvial en el estuario del Guadalquivir a múltiples escalas espacio-temporales, haciendo especial énfasis en las posibles implicaciones que tendría una profundización sobre la salinidad y los sólidos en suspensión. Para ello, se discuten los distintos mecanismos que controlan el flujo de sal, caracterizando esta circulación a través del coeficiente de viscosidad turbulenta. Además, se obtienen leyes potenciales para conocer la influencia relativa de las mareas, caudal de agua dulce y regímenes de viento sobre la intrusión salina. En este trabajo también se aplican técnicas no estacionarias de análisis, como el análisis armónico a corto plazo y la transformada de ondícula (transformada walet). Estos análisis permitieron la identificación de cambios frecuenciales en distintos puntos a lo largo del estuario en las señales de elevaciones, corrientes así como de los parámetros de elipses de marea; mostrando cuáles son los principales procesos afectados, desde una perspectiva mareo-fluvial, por valores altos de descarga de agua dulce.

A continuación, se emplearon ciertas relaciones empíricas entre los distintos agentes forzadores en el Guadalquivir para predecir los posibles cambios, a medio plazo, en la intrusión salina y

en los niveles submareales como consecuencia de una profundización en el canal de navegación. Debido a la naturaleza estocástica de la descarga de agua dulce y de la intrusión, se emplearon métodos no-estacionarios y cadenas de Markov. Para las mareas se emplearon modelos deterministas, métodos heurísticos y modelos de regresión para la intrusión y las elevaciones. Las simulaciones de los distintos escenarios se basaron en métodos de cadenas de Markov Monte Carlo. Además, se estudia el efecto que tendría sobre el estuario una disminución en el aporte de caudal de agua dulce para los próximos años.

Distinta escala y procesos presenta la ría de Punta Umbría en comparación con el estuario del Guadalquivir. Durante la última década, se han diseñado y ejecutado tres canales de navegación diferentes en la desembocadura para asegurar la operatividad y seguridad a través de la misma. Debido a los altos costes económicos y medioambientales asociados, los gestores demandan alternativas más eficientes. Para ello, se emplearon medidas hidrodinámicas y dieciocho batimetrías detalladas de la zona. Así pues, se pudieron identificar y cuantificar distintos estados de la desembocadura, considerando tanto las actuaciones de dragado como la evolución del lecho. Un modelo numérico fue calibrado y validado para esta área de estudio, dada la necesidad de conocer mejor la interrelación existente entre los cambios morfológicos y la hidrodinámica. La influencia tanto de la marea como del oleaje se evaluó mediante el cálculo de sendos flujos de energía. La divergencia de estos flujos se relacionó con la actividad morfológica del lecho, encontrando que existe una correspondencia entre las zonas que presentan una mayor sedimentación y aquéllas que tienen una mayor divergencia (negativa) en los flujos. De esta manera, esta Tesis propone una alternativa a los presentes diseños cuya eficiencia radica en minimizar la divergencia de los flujos de energía.

CONTENTS

Contents	xvi
Chapter one: Introduction	1
1.1 Motivation	1
1.2 Background	2
1.3 Objectives	3
1.4 Outline of the Thesis	4
1.5 Studies associated with this Thesis	4
Chapter two: Social, economic and environmental aspects of dredging	7
2.1 Dredging, a global overview	8
2.2 Dredging at Andalusian ports: operations database and Punta Umbría inlet	11
Database methodology	12
Database results	15
The case of the Punta Umbría inlet	19
2.3 Dredging at Andalusian ports: the case of the Guadalquivir estuary	20
Guadalquivir estuary historical overview	20
The Guadalquivir estuary nowadays	21
2.4 Results & Conclusions	25
Chapter three: Analysis of processes in the Guadalquivir estuary	27
3.1 The Guadalquivir-river estuary: Study area	28
3.2 Saline intrusion mechanisms	29
Hydrodynamics and salt structure classification	30
Baroclinic circulation	30
Saline intrusion Power Law	32
3.3 Tidal-fluvial interaction: spatial and frequency-dependent response of currents and water levels	34
Water level and Current responses	36
Remarks	46
3.4 Effects of a dredging intervention in the Guadalquivir estuary	48
Tidal amplification	48
Increased suspended matter concentrations	49
Increased stratification	50
Drag reduction	51
Remarks	52
3.5 Results & Conclusions	52

Appendices	53
3.A Data Collection	53
3.B Time Series Analysis Methods	54
Chapter four: Simulation of management scenarios in the Guadalquivir estuary.	
Deepening implications	57
4.1 River discharge: Non-stationary modeling	58
Stationary modeling	58
Non-stationary modeling	58
4.2 Saline intrusion: Markov Chain Monte Carlo methods & Management Scenarios Simulations	59
Markov Chain Monte Carlo Simulations	59
Management Scenarios Simulations	62
4.3 Subtidal levels and currents: Regression models & Management Scenarios simulations	64
Regression models	64
Management Scenario Simulations	66
4.4 Results & Conclusions	70
Appendices	71
4.A Non-Stationary discharge distribution	71
4.B Markov Chain Monte Carlo methods	72
Monte Carlo Simulation	72
Autoregressive processes and Markov Chain	72
4.C Subtidal regression models	73
4.D Regression models associated results	76
Chapter five: Analysis of processes and dredging alternatives in the Punta Umbría inlet	79
5.1 Tidal inlets: A management approach	80
5.2 The Punta Umbría inlet: Study Area	80
5.3 Materials and Methods	81
Data	82
Numerical Model	83
Morphodynamics	84
5.4 Morphology and tidal-wave competition	86
Forcings hydrodynamics	86
Navigational channels and natural state	86
Morphological activity index and states	88
Energy fluxes and Divergence	90
Morphodynamics	92
5.5 Dredging alternative in the Punta Umbría inlet	94
5.6 Results & Conclusions	96
Appendices	96
5.A Wave and tidal description	96
5.B Tidal wave interaction: Wave seasonal variability and tidal effects	97
Chapter six: General conclusions and future research	101

6.1	General conclusions	101
6.2	Future research	103
	Bibliography	105

INTRODUCTION

1.1 Motivation

An estuary is the transition between the river and the sea (Savenije, 2005). These semienclosed bodies of water show a great diversity of size, shape and depth (Valle-Levinson, 2010); which receives sediments from both fluvial and marine sources and contains facies influenced by tides, waves and fluvial processes (Dalrymple, Zaitlin, and Boyd, 1992), amongst others. These areas are crucial for societies as well as for the environment, being the ecosystem for a wide range of life forms, the economic foundation of coastal nations and the waterway between land and open sea. The interaction between the different forcings and processes is rather complex, comprising multiple spatio-temporal scales.

Communities in the vicinity of large rivers and coastal areas need to transport people, equipment and commodities by water. This fact usually implies the deepening of waterways, thus increasing the access to harbors and inland ports. The demographic developments and growth rates indicate that human involvement with water-related issues will continue to increase in the near future (Bray and Cohen, 2010). This increase will place a greater demand on residential, employment and recreational facilities, as well as on the environment, beach protection and other health and safety requirements. In fact, land reclamation, beach nourishment, seaborne world trade and the need of maintaining water depths would increase in future, which are the major drivers for dredging (IADC, 2014). In Europe, ports are of vital economic interest, handling up to 90% of Europe's international trade and 40% of the volume of ton-kilometers carried out in intra-Community trade (The European Commission, 2012). Hence, it seems that neither the dredging activities associated to inland ports nor the consequent alteration in the estuarine morphodynamics would diminish.

Dredging activities have increased in recent decades. This increase agrees with the rising in the complexity of their management, with higher demands for considering multiple economic, environmental and ecological factors: tidal flats occupation and modification, overexploitation of natural resources and pollution, highlight. Thus, a better understanding of the forcings affecting

the dredging and the sediment budget derived from it is required: tidal motion, waves, winds and human activity, are amongst them (CEDA, 2012). The constant changes in the forcings conditions, their interrelation at multiple scales, and the uncertainties when foreseeing their effects on the morphology of the medium to be dredged, make these projects a challenging task for the scientific and the engineering community.

One of the most common effects of deepening the navigation channels in estuaries is the amplification of the tidal range. There are records in European ports inside estuaries, situated more than 50 km from the mouth, which point the ongoing deepening and canalization as the responsible of the tidal amplifications, shifting them towards a hyperturbid state. These higher suspended matter concentrations in the water column are a necessary condition for the feed-back between hydraulic drag reduction and tidal amplification (Winterwerp and Wang, 2013).

The knowledge about the response of estuaries to dredging activities is still limited. Therefore, there is a real need to use and combine multiple methods and tools when exploring the effects of such interventions at different spatio-temporal scales (Jonge et al., 2014). Thus, the main driver motivation for this thesis is this lack that still exists when understanding and assessing the impacts of dredging projects into the main morphodynamic processes in estuaries. The southwestern of the Iberian Peninsula, close to the axis of one of the world's major maritime routes, accounts for several estuaries and tidal inlets. In the region of Andalusia, the natural balance of some of these is deeply affected by human activities. These alterations are especially noticeable in the Guadalquivir estuary and the Punta Umbría inlet, then selected for the current study. This dissertation uses multiple spatio-temporal approaches, based on field measurements, to better understand and characterize the main estuarine processes and forcings interaction; accounting for simulation techniques and numerical models when quantifying the response of estuaries to dredging projects.

1.2 Background

For several years the *Environmental Fluid Dynamics Group* (GDFA) of the University of Granada has been working on estuarine dynamics and coastal environments. The following studies provided valuable information and techniques to this Thesis.

In 2007 a scientific committee was formed to assess the environmental impact of the project to improve access to the inland port presented by the Port Authority of Seville. This committee included members of the Spanish National Research Council (CSIC) and the University of Granada and the University of Córdoba, through the GDFA and the research group of Fluvial Dynamics and Hydrology, respectively. A comprehensive research study was carried out in this estuary, resulting in the publication of the report Ruiz and Losada (2010): Methodological proposal for the diagnosis and forecast of human action in the Guadalquivir estuary.

Since then, a large number of valuable information about the state and behavior of the Guadalquivir estuary has been revealed, based on the data from a real-time, remote monitoring network (Navarro et al., 2011) deployed between 2008–2011. With these measurements, Díez-Minguito et al. (2012) discussed the tidal wave propagation along the whole estuary and the role of tidal reflection, friction and channel convergence. The authors also analyzed the dynamics of the estuary under different forcing natural agents and distinguished normal, extreme and

exceptional conditions, according to the effect of the freshwater discharge on tides. Díez-Minguito et al. (2013) analyzed the salinity distribution, as well as the variation of the saline intrusion in comparison to the freshwater discharge and other hydrodynamic variables. Salt flux transport mechanisms were identified for different flow regimes. Regarding the turbidity in the estuary, Díez-Minguito et al. (2014) studied the transport of suspended particulate matter (SPM) during low river flow conditions. The main mechanisms that contribute to longitudinal SPM transport were identified and quantified, describing the estuary turbidity maxima in the estuary. Other investigations discussed the trophic state of the system (Navarro et al., 2012; Ruiz et al., 2013), the thermal energy exchange between the estuary and the continental shelf (García-Lafuente et al., 2012), the global thermal energy transport in the estuary (Padilla et al., 2015) and the river sediment load influence to events of extreme turbidity (Contreras and Polo, 2012), amongst others.

The GDFA has also been working on decision-making processes for dredging activities in other Andalusian ports. The Regional Government, through the Agencia Pública de Puertos de Andalucía, promoted the project G-GI3002/IDII *"Dragados en el sistema portuario andaluz: método para la gestión y toma de decisiones"* (*Dragaport: Dredging in the Andalusian port system: methods for the management and decision-making*). Between 2013–2015, GDFA applied an ample range of tools and analysis, such as the development of a database to support dredging activities management, with analogous methodology to that applied in Magaña et al. (2014); non-stationary wave climate analysis and multivariate time series simulations with the methodology of Solari (2011); and the implementation of numerical modeling in different ports, similar to those applied in other highly-human altered coastal environment (Zarzuelo et al., 2015).

1.3 Objectives

The overall objective of this thesis is the analysis of the main estuarine morphodynamic processes, at different spatio-temporal scales, and their influence on the dredging projects. The studied cases correspond to two different estuaries in the southwestern of the Iberian Peninsula, namely in the Andalusia region: the Guadalquivir estuary and the Punta Umbría inlet.

The following specific objectives were defined to accomplish the main objective:

- Social, economic and environmental aspects of dredging: Assessment of the dredging interventions for the study areas and their relevance from a global to a regional point of view.
- Salt intrusion mechanisms: Analysis of the estuarine circulation and the dependence of the salt intrusion on the climate forcing agents.
- Tidal and subtidal regime shifts: Analysis and modeling of the controlling mechanisms of the non-stationary response of tidal and subtidal water levels and currents in estuaries.
- Effects of deepening navigation channels: Analysis of the changes in the estuarine processes as a consequence of the feed-back loop between tidal motion and suspended matter concentrations.

- Management scenarios simulations: Prediction of the mid-term effects of both deepening the navigation channel and freshwater discharge reduction applying Markov Chain Monte Carlo methods, quantifying salt intrusion and subtidal water levels shifts.
- Tidal-wave competition: Analysis and modeling of tidal and wave energy fluxes in inlets, focusing on their relationship with both the morphodynamics and the dredging projects.
- Efficient dredging designs: Development of alternatives to present navigation channel designs able to minimize the environmental and socio-economic impacts in estuaries.

1.4 Outline of the Thesis

Apart from the introduction (Chapter 1), this Thesis is organized as follows:

Chapter 2 presents an overview of the dredging activity from a fully-integrated perspective, with particular emphasis on the region of Andalusia and the selected studies areas, the Guadalquivir estuary and the inlet of Punta Umbría.

Chapter 3 is dedicated to the analysis of different processes, at different spatio-temporal scales, in the Guadalquivir estuary. The estuarine circulation and the tidal-fluvial interaction, as well as the implications of the dredging interventions into the estuarine morphodynamics, are assessed.

Chapter 4 completes the previous one through simulation techniques. Non-stationary modeling and Markov Chain Monte Carlo methods are used to predict the mid-term effects, on the subtidal water levels and saline intrusion distribution, of different management scenarios in the Guadalquivir estuary; including the deepening of the navigation channel.

Chapter 5 studies the morphodynamics in the Punta Umbría inlet and the tidal-wave competition. Numerical modeling is used to propose an alternative management strategy to the present navigation channel designs.

Finally, Chapter 6 summarized the main conclusions of this Thesis and future research.

1.5 Studies associated with this Thesis

Journal Papers

- **Reyes-Merlo, M. Á.**, Díez-Minguito, M., Ortega-Sánchez, M., Baquerizo, A., and Losada, M. Á., (2013). On the relative influence of climate forcing agents on the saline intrusion in a well-mixed estuary: Medium-term Monte Carlo predictions. *Journal of Coastal Research*, 65(sp2), 1200-1205.
- Losada, M.Á., Díez-Minguito, M. and **Reyes-Merlo, M.Á.**, (2016). Tidal-fluvial interaction in the Guadalquivir Estuary: Spatial and frequency-dependent response of currents and water levels. *Journal of Geophysical Research - Oceans* (Under review).

- Ortega-Sánchez, M., Magaña, P., **Reyes-Merlo, M.Á.**, Tintoré-Parra, Á., Zarzuelo, C., and Díaz-Carrasco, P., (2016). Assessment of civil engineering maintenance activities: a methodological approach. *Submitted to Environmental Modelling and Software*.
- **Reyes-Merlo, M. Á.**, Ortega-Sánchez, M., Díez-Minguito, M., and Losada, M. Á., (2016). Optimization of tidal inlet navigation channels: the case of Punta Umbría, Southwestern Spain (Under preparation).

International conferences

- **Reyes-Merlo, M. Á.**, Díez-Minguito, M., Ortega-Sánchez, M., Baquerizo, A., and Losada, M. Á., (2013). On the relative influence of climate forcing agents on the saline intrusion in a well-mixed estuary. *Proceedings of the 12th ICS- International Coastal Symposium*. Plymouth (England).
- **Reyes-Merlo, M. Á.**, Díez-Minguito, M., Baquerizo, A., and Losada, M. Á., (2015). Markov Chain Monte Carlo predictions of the saline intrusion in a well-mixed estuary. *Aquatic Science Meeting, organized by the ASLO- Association for the Sciences of Limnology and Oceanography*. Granada (Spain).
- Tintoré-Parra, Á., **Reyes-Merlo, M. Á.**, Jiménez, M.Á., Ortega-Sánchez, M., and Losada, M. Á., (2015). Management strategies for highly altered estuaries: the case of Punta Umbría (Huelva, Spain). *Aquatic Science Meeting, organized by the ASLO- Association for the Sciences of Limnology and Oceanography*. Granada (Spain).
- **Reyes-Merlo, M. Á.**, Tintoré-Parra, Á., Díez-Minguito, M., Ortega-Sánchez, M., and Losada, M. Á., (2015). Morphodynamic evolution and influence of dredging activities in small-scale mesotidal estuaries: the case of Punta Umbría (Southwestern Spain). *Proceedings of the 36th IAHR-International Association for Hydro-Environment Engineering and Research*. The Hague (the Netherlands).
- **Reyes-Merlo, M. Á.**, Díez-Minguito, M., and Losada, M. Á., (2016). Predictions of subtidal water levels and currents with nonstationary Monte Carlo simulations. *18th PECS- Physics of Estuaries and Coastal Seas Conference*. The Hague (the Netherlands).

National conferences

- **Reyes-Merlo, M. Á.**, Díez-Minguito, M., Ortega-Sánchez, M., Baquerizo, A., and Losada, M. Á., (2013). Influencia relativa de los agentes forzadores en la intrusión salina en un estuario bien mezclado: análisis a medio plazo mediante simulación de Monte-Carlo. *XII Jornadas Españolas de Ingeniería de Costas y Puertos*. Cartagena, Spain (in spanish).
- **Reyes-Merlo, M. Á.**, Tintoré-Parra, Á., Mocres-Moya, M.A., Ortega-Sánchez, M., Díez-Minguito, M., and Ollero, M., (2015). Morfodinámica del estuario de Punta Umbría (Huelva): impacto en los dragados del canal de acceso. *XIII Jornadas Españolas de Ingeniería de Costas y Puertos*. Avilés, Spain (in spanish)

- Tintoré-Parra, Á., Magaña P., **Reyes-Merlo, M. Á.**, Ortega-Sánchez, M., and Ollero, M., (2015) Importancia de los dragados en el sistema portuario andaluz. *XIII Jornadas Españolas de Ingeniería de Costas y Puertos*. Avilés, Spain (in spanish)

SOCIAL, ECONOMIC AND ENVIRONMENTAL ASPECTS OF DREDGING

Dredging works should be designed in harmony rather than in conflict with nature, minimizing side effects both in the environment and in the society. The physics involved in coastal and estuarine systems are rather complex, with multiple forcings and processes interrelated and influenced by human presence. It is the aim of this Chapter to give a general overview of the dredging activity and its impact on the environment from a socio-economic perspective, providing the framework that this dissertation faces.

Section 2.1 describes the main drivers of dredging, assessing the relevance of the dredging activity from a global to a European and National (Spanish) perspective. The next two sections address the problem from a regional (Andalusian) point of view with different approaches. On the one hand, Section 2.2 uses one of the methods developed during the project *Dragaport* (Section 1.2): an object-relational database designed to improve the decision-making process when dredging in the ports managed by the Regional Government of Andalusia. A fully-integrated assessment considering the volume of mobilized material, cost efficiency of the interventions and the influence of the wave climate is presented; showing the relevance of the Punta Umbría inlet in Andalusia. On the other hand, Section 2.3 focus on the conflict between the different stakeholders in the Guadalquivir estuary, which is one of the most important environmental and socio-economic areas in the southwestern Spain. Past and present management policies are analyzed to understand the role of dredging activities in the estuary, as well as the proposed future interventions.

2.1 Dredging, a global overview

Dredging is a necessary activity in civilization's development. These operations, usually carried out underwater, consists in excavating soils and rock and disposing of them at a different location. The basic reasons or drivers for dredging include, amongst others (Bray and Cohen, 2010): i) maintaining the water depths and thus the ship traffic/seaborne world-trade with the maximum safety and operational conditions, ii) infrastructure construction and land reclamation, iii) beach nourishment, iv) improving sea or river defences against flood risk, v) environmental remediation in waterways or subaqueous facilities, vi) mining and vii) covering the growing demands for energy, with interventions for underwater foundations for the placement of oil, gas or other pipelines or tunnels.

Throughout history, most important civilizations were born in the vicinity of large rivers and coastal areas. These communities needed to transport people, equipment, materials and commodities by water to grow; implying the channel depths of many waterways to be increased to provide proper access to ports and harbors. Over the years, global changes in marine engineering and water management have come in many ways. However, the most remarkable hydraulic works that have altered our world and our living conditions occurred over the past centuries: science and technology have turned the threat of water into a major challenge and a commercial opportunity (Vanderostyne and Cohen, 1999). Particularly, the development of powerful dredging machinery in recent decades, formal education of crew, quality control and safety management increased the scope and complexity of engineering projects which could be executed by dredging (IADC, 2015).

Dredging activities mostly take place in rivers, canals, estuaries, ports and coastal areas. These areas, in which human activities are interlinked with both the land and the sea, are of great societal importance, often serving as the source or foundation of the economy of coastal nations. Indeed, 23% of the global population currently live within 100 km of the coast and less than 100 m above sea level, with a population density in this coastal areas three times larger than average (Masselink and Gehrels, 2014). Demographic developments and growth rates indicate that human involvement with water-related issues will continue to increase with the passage of time (Bray and Cohen, 2010). The current world population of 7300 million is expected to reach 8500 million by 2030 and 9700 million by 2050. By 2025, predictions indicate that approximately 6000 million people would be living within 200 km of a coastal line. This increase will place a greater demand on residential, employment and recreational facilities, as well as on beach protection and other health and safety requirements. In fact, the need for more land has increased the need for reclamation and would do so in the future, which is a major driver for dredging (IADC, 2014).

As dredging activities have increased in recent decades, the concern regarding its impacts on the environment has grown too. This increase agrees with the rising in the complexity of environmental management, with higher demands for considering multiple economic, environmental and ecological factors. Thus, a better understanding of the forcings affecting the dredging is required: sediment budget, currents, waves, winds, water levels, tidal range and human activity are amongst them (CEDA, 2012). Also, constant changes in these agents conditions, their interrelation and the uncertainties when foreseeing their effects on the morphology of the medium 'to be dredged', make dredging a challenging task for the scientific and the engineering

community.

The following sections perform a global review of the Worldwide and European dredging market, to assess the impact of this activity.

Worldwide dredging

Between 1977 and 2011, world Gross Domestic Product (GDP) rose by a Compound Annual Growth Rate (CAGR) of 3.2%, while seaborne trade did by 3.1% and the number of containers shipped worldwide by 9.7%. Whereas in the 70s the introduction of large crude carriers led to investments in ports, the current containerization, boosted by economies of scales with its ongoing trend of manufacturing larger container vessels, are stimulating the dredging market (Rabobank, 2013). The total turnover of global dredging contractors (private as well as state- or port-owned companies), per driver and its geographic spread, are represented in Figure 2.1.1. Data was obtained from the International Association of Dredging Companies (IADC), whose members market share represents around 50% in the entire dredging market and around 90% in the open market (values in 2013).

From 2000 to present, the global dredging turnover has more than doubled, from around €4000 mln to €11,680 mln in 2013. Between 2007 and 2013, this rise is of 25%. As inferred from Figure 2.1.1, the drivers of dredging have developed favorably for about a decade at a moderate but steady pace, with a notable rising in the seaborne world trade, which is the most important driver for the dredging industry. Subsequently, there has been an increased demand for the capacity and efficiency of ports. Thus, new ports and hinterland infrastructure are required, where dredging is needed to maintain and deepen existing waterways, as well as supplying material for extending berths and strengthen quay walls. The geographical distribution analysis revealed that, though in China few projects are open for international tenders, is by far the leading region. Mostly, its adhesion to the global seaborne trade in the past years has been to a high level. This region is followed in significance by Europe, the rest of Asia and Middle East.

Dredging in Europe and Spain

The previous section showed that the larger the port activity is, the more dredging is done. In fact, the European ports are of vital economic interest, handling up to 90% of Europe's international trade and 40% of the volume of tonne-kilometers carried out in intra-Community trade (The European Commission, 2012). This activity contributes, amongst other factors, the leadership of European dredging industry in the world. According to the European Dredging Association (EuDA), European dredging companies have a 90% market share of dredging in the worldwide open market, with an investment of €7000 mln from 2008–2012. Also, the European innovation has created new markets, where 2.5% of turnover is re-invested in R&D.

The relevance that the EU has given to dredging activity and its impact on the environment has been directly or indirectly reflected in its legislation, such as in the *Water Framework Directive* and *The Habitats Directive*. The Member States have to both ensure the protection of the environment, promote sustainability of economic development and implement the transport policies. This results, most of the times, in continuous conflicts between different stakeholders. An extensive list of these EU policies, with case study implementations, can be found in The European Commission (2009). Though some dredging associations do not completely agree with

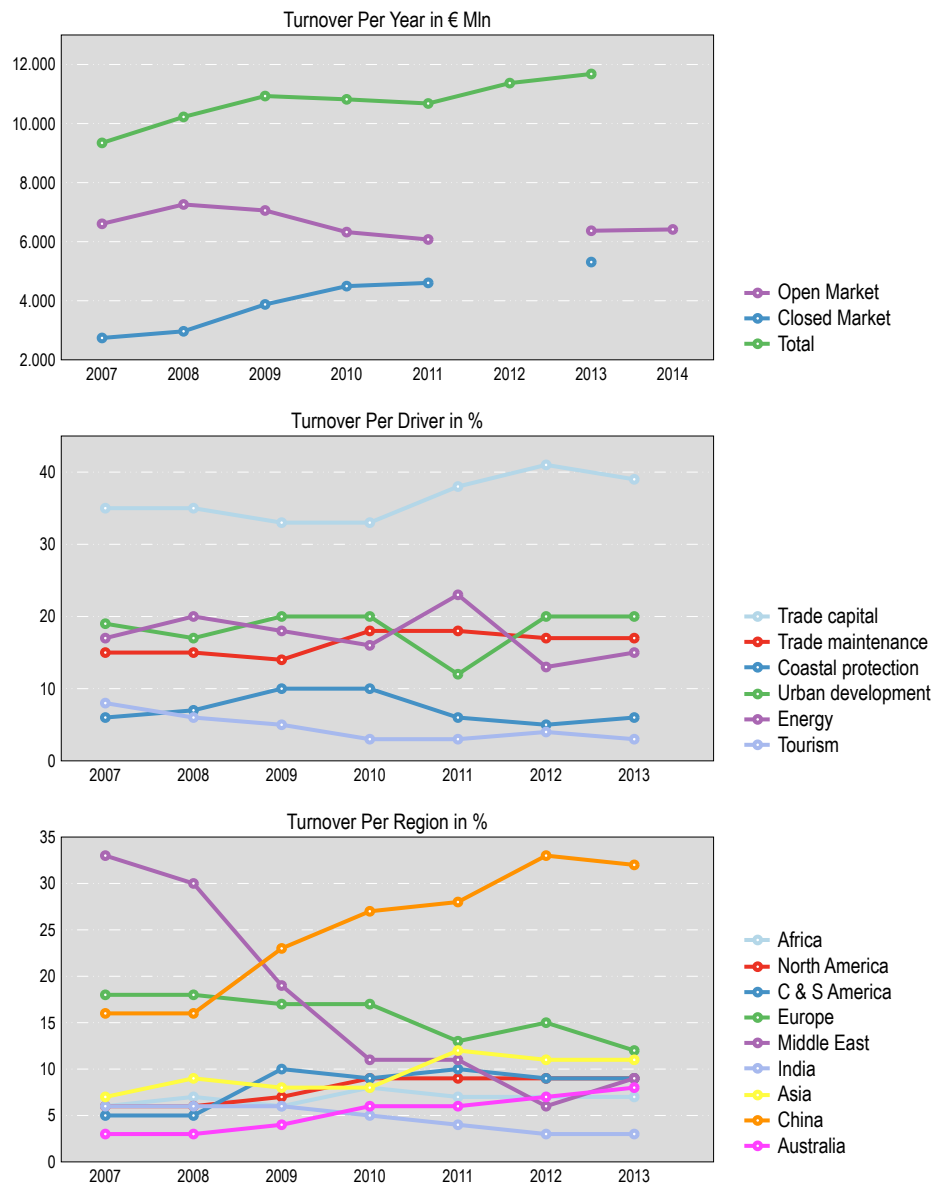


Figure 2.1.1: Panel a: turnover in the open and closed market and the sum of both in € mln. Panel b: Percentage of the total turnover of Panel a per driver. Panel c) Percentage of the total turnover of Panel a per region, as the sum of open and closed market. Europe includes Turkey, Western Russia and the Black Sea countries. Eastern Russia, Caspian Sea countries, Japan and SE Asia are included in Asia. The figures relates to underwater excavation, transportation and placement of dredged material. It does not include maritime construction such as breakwaters, offshore installations, harbour infrastructure, dams, dikes and other infrastructure in which dredging contractors are involved. However, within this figure, some of the rock works are an integrated part of land reclamations and coastal defense. Designed from IADC data (IADC, 2014; IADC, 2015).

the procedures that these policies imply (Mink et al., 2006), their importance have been evidenced when deciding whether or not to approve a dredging intervention in estuaries. Some examples are the Weser (CJEU, 2015) and the Guadalquivir (Supreme Court, 2015).

Spain is the country with the longest coastline (8,000 km) in the EU. Its geographical location, being closer to the axis of one of the world's major maritime routes, place the Spanish ports as the main Hub in southern Europe. The State-owned Spanish Port System includes 46 ports of general interest, managed by 28 Port Authorities, whose coordination and efficiency control corresponds to the government agency Puertos del Estado. These ports handle nearly 60% of exports and 85% of imports, which account for 53% of Spanish foreign trade with the European Union and 96% with third countries. The State Port System's activity contributes nearly 20% of the transport sector's GDP, which accounts for 1.1% of the Spanish GDP. This information correspond to data from 2016 of the Spanish Port System.

The total amount of mobilized material by the Spanish Port System between 1995–2012 was 208,744,635 m³, with an increase in the period 2005–2012 respect to 1995–2004 of 7.2%. This trend agrees with the global dredging rise in recent decades. Figure 2.1.2 depicts the use of the removed material and its evolution in time, obtained with the data from CEDEX (2007) and CEDEX (2013). While the percentage of reused material remains constant at 57%, the disposal at sea has notably decreased to 17%.

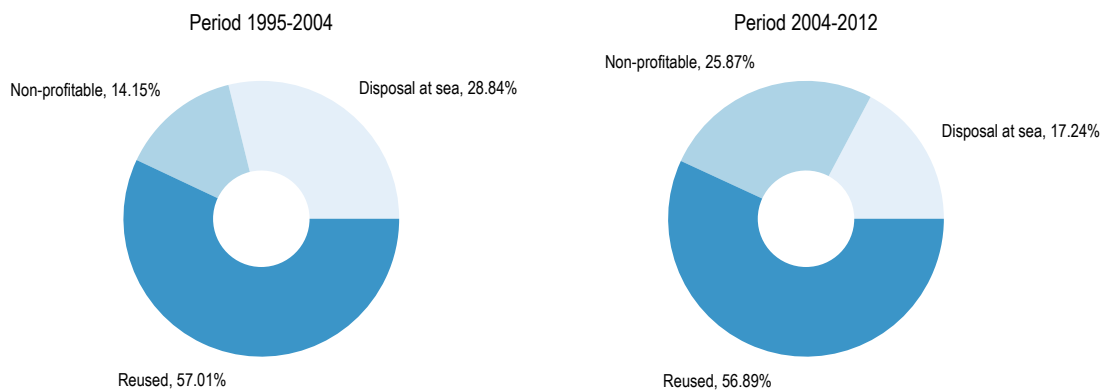


Figure 2.1.2: Evolution in the use of the dredged material in the Spanish Port System for the indicated periods. Elaborated from CEDEX (2007) and CEDEX (2013).

2.2 Dredging at Andalusian ports: operations database and Punta Umbría inlet

To date, there are 53 ports along the coastline of Andalusia (Table 2.2.1), averaging one port every 21 km of coastline, and with 30% of them located in estuaries, rivers and/or river mouths. Their distribution between the Atlantic and the Mediterranean coasts is very similar (47—53%, respectively), even though the length of the Mediterranean coast is significantly larger. The morphological complexity of the Mediterranean coast, with many cliffs and a significant proportion of rocky coast (Ortega-Sánchez et al., 2014), and the importance of the shipping routes in the Atlantic partially explain this difference.

The main commercial operations take place at the 13 ports owned and operated by the Spanish Port System (Table 2.2.1); the rest are managed directly or indirectly by the public agency APPA of the Regional Government of Andalusia. These ports are mainly dedicated to

providing leisure or fishing services. APPA functions consist of the maintenance, reparation, facilities and infrastructure development and integral management. To improve the dredging management, this Institution funded, between 2013–2015, the R&D project “Dragados en el sistema portuario andaluz: método para la gestión y toma de decisiones” (from now on referred to as Dragaport) of the “Programa Operativo FEDER 2007–2013”.

Dragaport project focused on the analysis of the 20 ports (Figure 2.2.1) that are directly managed by the APPA, in which at least one dredging operation has been done. This section includes the key points of the implemented methodology and the most relevant results, pointing PUI as especially problematic port in Andalusia.

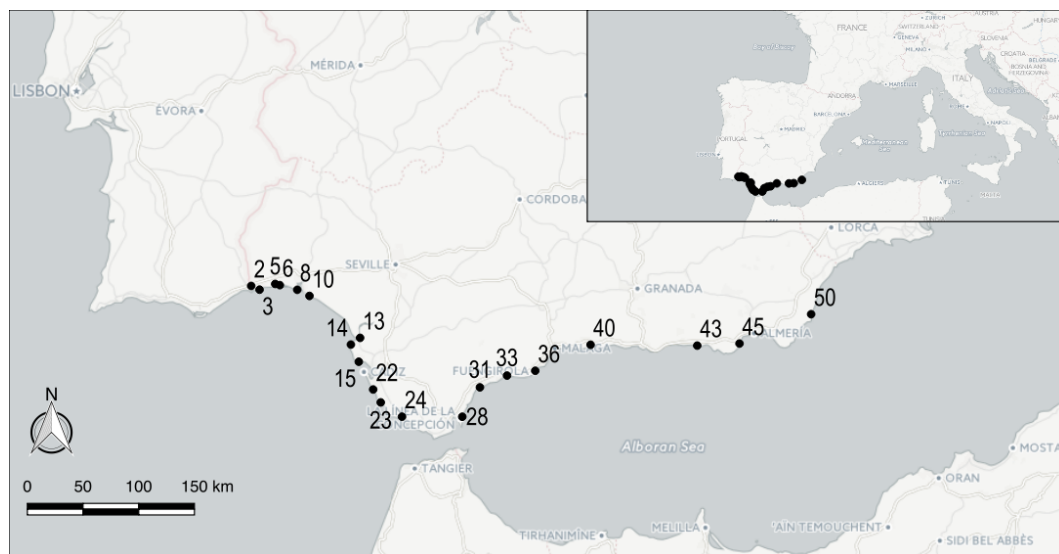


Figure 2.2.1: Study area and locations of the ports in the Andalusia region of Spain. The numbers increase from west to east and correspond to the information in the database (only ports analyzed in this paper are included).

2.2.1 Database methodology

The proposed methodology to analyze the data corresponds to Magaña (2015), based on the compilation, organization, and analysis of several fields of information about the maintenance activities associated with a given Civil Engineering (CE) infrastructure (i.e. roads, railways, ports or bridges). The methodology was applied to the case study of APPA ports, which resulted in a dataset that was integrated into an open and public database, including its incorporation into GIS systems for further analysis. A brief explanation of the methodology is given below.

Scheme of the methodology

The phases of the methodology are (Figure 2.2.2):

- Phase 1: Collection of activities. The information is collected and classified by locations.
- Phase 2: Organization of the documentation. The information about each location is organized into two groups: consulting (associated with the initial design of the project)

Table 2.2.1: Name, ownership and function of the Andalusian ports. Ports managed by the Spanish Port System or by the Andalusian Regional Government (directly or indirectly) are denoted as PE, APPA-D and APPA-I respectively. Numbering is in correspondence with the information included in Figure 2.2.1

PROVINCE AND NUMBERING OF PORTS	PORT NAME/HARBOUR NAME	MANAGEMENT	FUNCTION		
			LEISURE	FISHING	COMMERCIAL
HUELVA					
	1 Sanlúcar de Guadiana	APPA D	X		
	2 Ayamonte	APPA D	X	X	
	3 Isla Cristina	APPA D	X	X	
	4 Isla Canela	APPA I	X		
	5 El Terrón	APPA D	X	X	
	6 El Rompido	APPA D	X	refuge	
	7 Marina de Nuevo Portil	APPA I	X		
	8 Punta Umbría	APPA D	X	X	
	9 Huelva	PE	X	X	X
	10 Mazagón	APPA D	X		
SEVILLA					
	11 Sevilla	PE	X		X
	12 Gelves	APPA I	X		
CÁDIZ					
	13 Pesquero de Bonanza	APPA D		X	
	14 Chipiona	APPA D	X	X	
	15 Rota	APPA D	X	X	
	16 Sherry	PE	X		
	17 La Cabezueta	PE			X
	18 Santa María	PE	X	X	X
	19 América	APPA D	X		
	20 Cádiz	PE	X	X	X
	21 de Gallineras	APPA D	X		
	22 Sancti Petri	APPA D	X	refuge	
	23 Conil	APPA D	X	X	
	24 Barbate	APPA D	X	X	X
	25 Tarifa	PE		X	X
	26 Algeciras	PE	X	X	X
	27 La Alcaidesa (Línea de la Concepción)	PE	X		
	28 La Atunara	APPA D		X	
	29 Sotogrande	APPA I	X		
MÁLAGA					
	30 La Duquesa	APPA I	X		
	31 Estepona	APPA D	X	X	
	32 José Banús	APPA I	X		
	33 Deportivo de Marbella	APPA I	X		
	34 Marina la Bajadilla	APPA I	X	X	
	35 Cabopino	APPA I	X		
	36 Fuengirola	APPA D	X	X	
	37 Benalmádena	APPA I	X		
	38 Málaga	PE	X	X	X
	39 El Candado	APPA I	X		
	40 Caleta de Vélez	APPA D	X	X	
GRANADA					
	41 Punta de la Mona	APPA I	X		
	42 Puerto de Motril	PE	X	X	X
ALMERÍA					
	43 Adra	APPA D	X	X	
	44 Almería	APPA I	X		
	45 Roquetas de Mar	APPA D	X	X	
	46 Agudulce	APPA I	X		
	47 Almería	PE	X	X	X
	48 San José	APPA I	X		
	49 Comercial de Carboneras	PE			X
	50 Pesquero de Carboneras	APPA D	X	X	
	51 Garrucha	APPA D	X	X	X
	52 Villaricos la Esperanza	APPA D	X	X	
	53 Villaricos la Balsa	APPA D	X	X	

and construction (associated with the final construction project and the executed works) information.

- Phase 3: Analysis of two selected activities to design the guideline table. Two representative activities are chosen with the managers as examples and benchmarks to select the fields of data to be included in the database. The most relevant variables are then grouped and organized into the first table design. The variables are reviewed, and the table is redesigned if necessary. A final table and set of variables are developed.
- Phase 4: Complete the final table. This step consists of collecting the data for all of the activities. Although many variables are similar to other types of CE maintenance activities, other specific data may be collected for further analysis depending on the type of activity (in our case, data about the maritime climate). As in Phase 3, periodic revisions by the working team are recommended to avoid inconsistencies.
- Phases 5 and 6: Incorporation into a database and GIS integration. The final steps consist of the incorporation of the information into a database and the full integration into a GIS.

The time to revise and compile all the information (Phases 1–4) depends mainly on the number of activities and variables, including the format of the information. The development of the database for the APPA ports took 5 months.

Development of the database and GIS integration

The object-relational database PostgreSQL was selected to store the information. This database management system has several notable features. PostgreSQL can handle spatial attributes such as points, polygons or lines using the PostGIS extension (Zhang and Yi, 2010), which makes it possible to perform spatial queries of the database (Carrera-Hernández and Gaskin, 2008). In addition, it can be easily linked to the statistical language R, which provides libraries for statistical analysis. Another advantage of PostGIS is that it can be linked to the open source GIS Quantum GIS (QGIS), which provides tools for raster, vector and point analyses as well as image processing.

In the case study, the data were incorporated into a PostgreSQL/PostGIS system. QGIS conveniently integrates these representational models and was used to depict the data and develop the different types of maps. Digital geodatabases allow the accumulation of large amounts of information that can be readily accessed with simple tools and are used in many fields of applied geography (Jäppinen, Toivonen, and Salonen, 2013; McCool, 2014; Rozenstein and Karnieli, 2011).

Some of these tools were successfully applied in (Magaña et al., 2014), who presented an open database with a total of 294 sites that showed shoreline undulations. Thus, this methodology provides a framework that can be extended to any other activity. In addition, this framework should be accessible using freely available and open source software when possible. Further details of this methodology can be found in Magaña (2015).

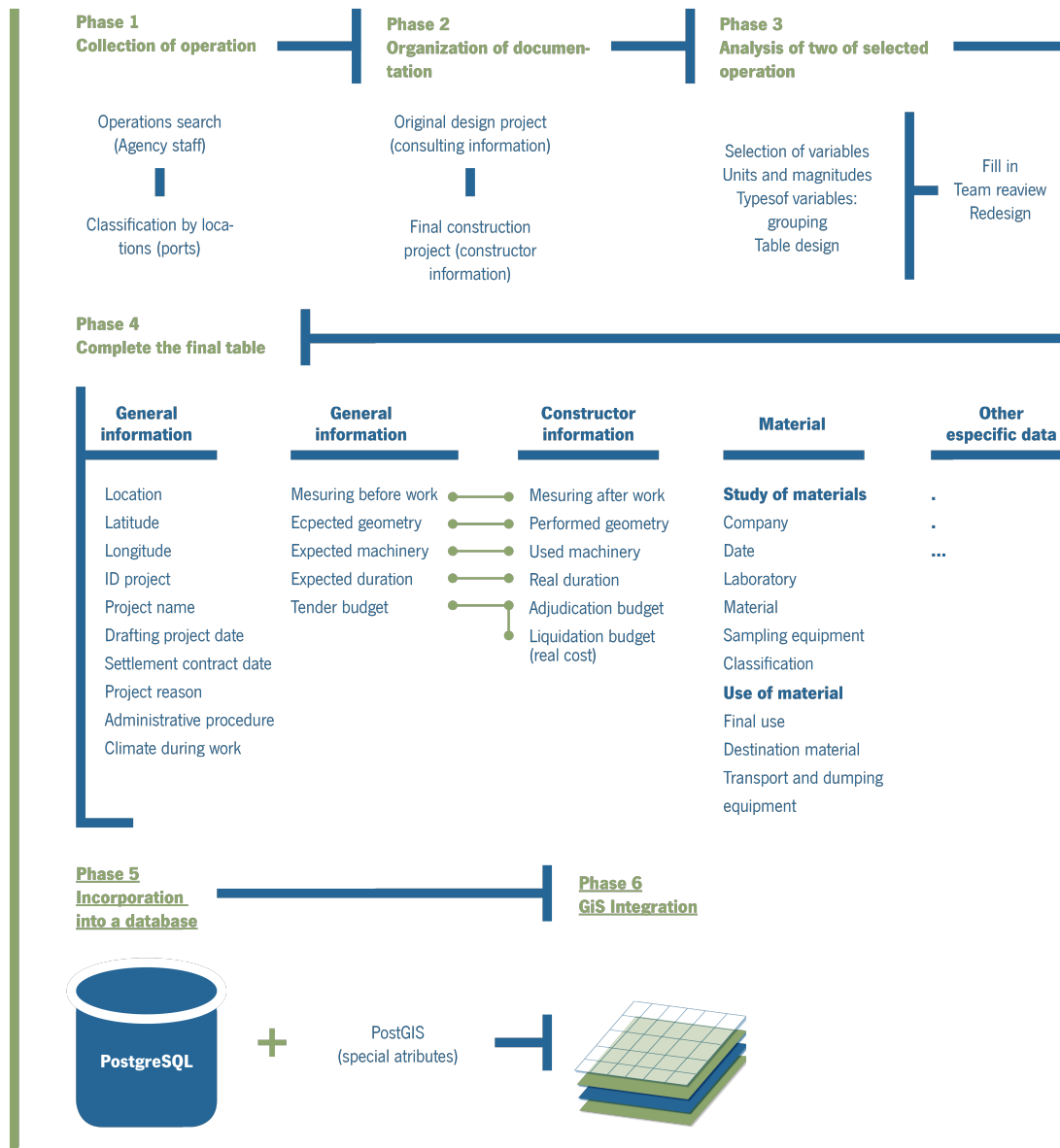


Figure 2.2.2: General scheme of the developed methodology to create databases from regular maintenance CE activities. Elaborated from Magaña (2015).

2.2.2 Database results

From 1993 to 2015, the regional government performed 70 dredging projects. A total of 87 fields of data were defined, many of them similar to other CE maintenance activities, although some others may be different (i.e., the geometric parameters). The total amount of sediment mobilized during the 70 interventions was 5,847,593 m³, thirty five times lower than in the Spanish Port System for a similar period. The average volume per intervention in the APPA ports is 83,537 m³. The maximum total volume was dredged at port nº 23 (1,536,380 m³) representing the 26% of the total amount, followed by Punta Umbría, port nº 8 (438,587.92 m³), representing 15% of the total. The most relevant results performed with the proposed methodology are presented below.

Destination of the dredged material

One of the major economic engines of the Andalusia region is the coastal tourist sector; therefore, the quality of the beaches is a priority for managers. Nevertheless, recent erosion processes have had negative impacts on the development of this social and economic sector due to the deterioration of the beaches. During the 1990s, reuse of dredging material from ports was practically non-existent (Figure 2.2.3). In contrast, 90% of the activities that were carried out during the last five years reused dredged material to replenish nearby beaches (Figure 2.2.3). Whereas dumping at sea tendency has decreased in the Spanish Ports (Figure 2.1.2), in APPA ports it has remained constant but for the past three years.

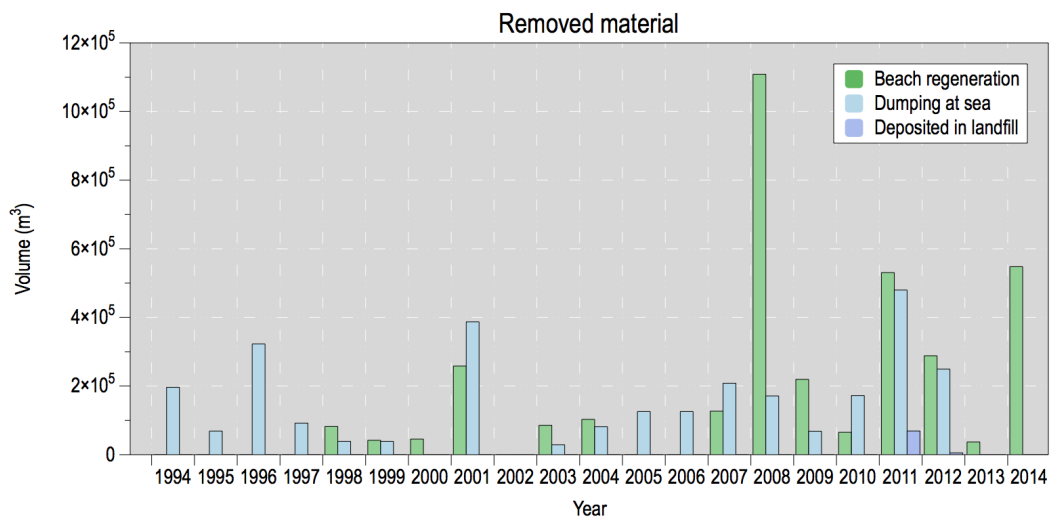


Figure 2.2.3: Evolution in the use of material removed by dredging activities performed by the Andalusian Regional Government in the last 20 years.

Current local regulations allow regeneration of beaches except at sites where other restrictions or regulations apply. The database allowed the identification of restricted ports where difficulties in the management of the dredged sediment occur. This is the case for port n° 50, which is located in a protected area and where disposal sites are far from the coast because dumping at sea and along the beach is strongly restricted. In some other cases, the materials are subjected to special treatments. For example, in port n° 45, material must be dried before dumping. To deal with these environmental issues, new research on the reutilization of dredged material is being performed (Zentar et al., 2009; Sheehan, Harrington, and Murphy, 2010).

Costs efficiency assessment

The total investment by the Andalusian Regional Government over the last 20 years was 39,420,534.10 €, and the largest expenditure of 8,136,443.09 € (20% of the total) occurred in 2011. Based on the information in the database, many useful indexes and rates can be defined for further in-depth assessments. The administration frequently works with the average liquidation budget per activity at every port, which is calculated as the ratio between the total of the liquidation budgets and the number of activities. Port n° 6 has the highest cost (2,238,577.42 €), followed by port n° 45 (1,525,133.01 €). In both cases, costs increased due to particular environmental issues; the former is located in a protected area, which slows the work, and the

latter has a unique problem with the final destination of the dredged material. In contrast, port nº 36 has the lowest cost (168,494.60 €).

The average cost of dredging 1 m³ at each port was calculated as the ratio between the liquidation budget and the dredging volume. The highest cost was at port nº 45 (78.45 €) because special material treatments are required before the material reaches its final destination. The second highest cost was at port nº 5 (18.21 €), whereas the minimum cost was at port nº 23 (3.51 €). From a global perspective, dredging projects are more efficient in the Atlantic watershed; while the dredging volumes and costs by activity are higher, the mean cost of dredging 1 m³ is lower (Atlantic: 6.28 €/m³ vs. Mediterranean: 8.28 €/m³). Hence, the assessment of the information in the database can inform the Administration about provinces that should be the focus of attention (i.e., improving the management of Atlantic ports due to the overall investment) but also identifies sites with specific problems (i.e., a deeper analysis of the dredging activities at port nº 45 is recommended).

Deviations from original projects

To appropriately manage CE activities, one of the most useful parameters is the relationship between the expected data (before the projects) and the real data (after the projects) of a given variable in the database. We define the percentage deviation (PD) as follows:

$$PD(\%) = \frac{D_R - D_E}{D_E} \cdot 100 \quad (2.1)$$

where D_R and D_E corresponds to the real and expected data, respectively.

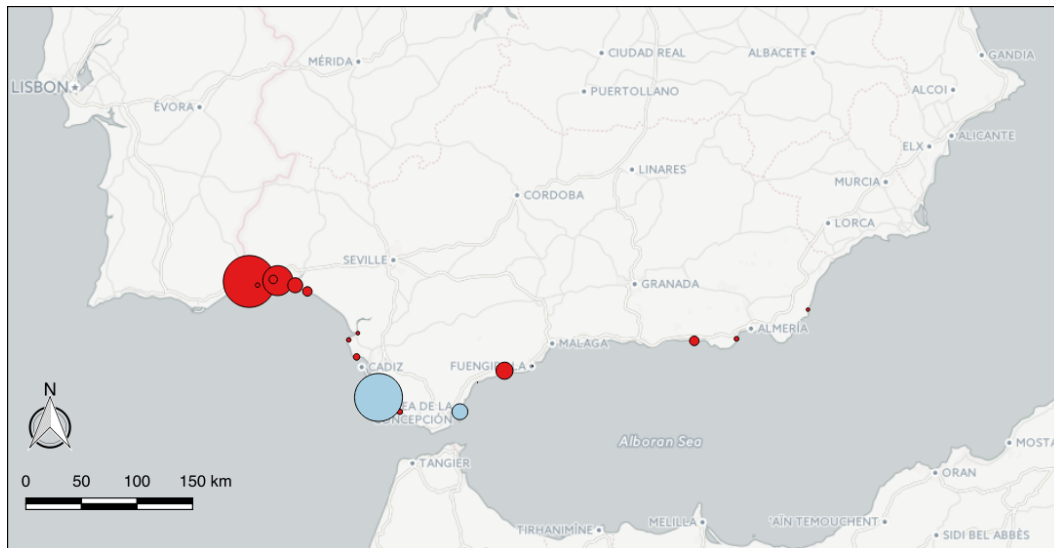


Figure 2.2.4: Percentage deviations of the budgets of the activities. Blue (red) colors indicate negative (positive) deviations.

As an example, the results for the deviation of the budget are shown in Figure 2.2.4. The major underestimations (positive values) are found at ports nº 2 and nº 6 (up to 31%) in Huelva Province, whereas the greatest overestimation (up to 50%) is at port nº 23 in Cádiz Province. These results can help to predict the performance and behavior of future activities at a given site.

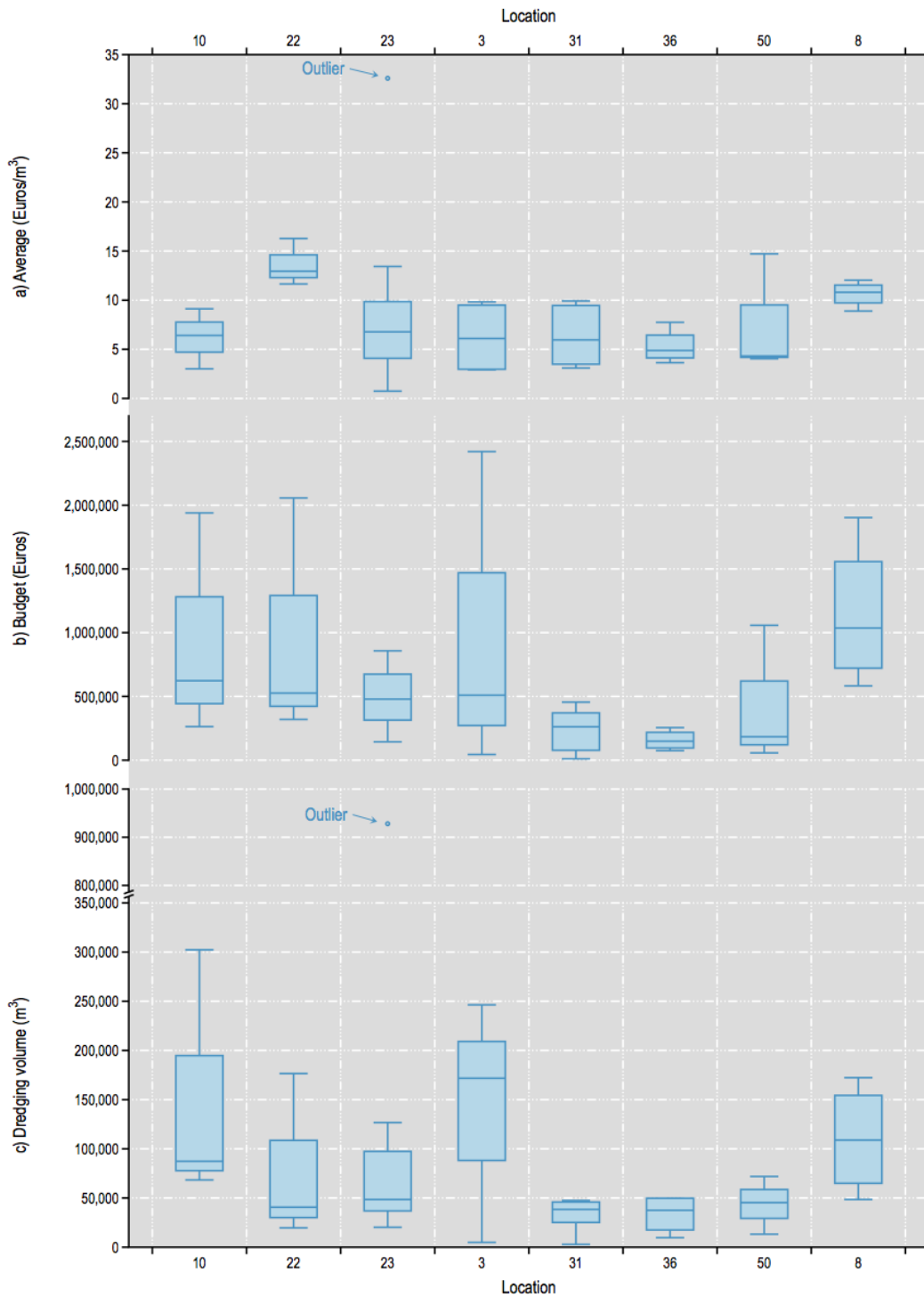


Figure 2.2.5: Box-plot showing the analysis of (a) the average price of dredging 1 m³ of material, (b) liquidation budget of dredging activities and (c) dredging volume of each activity. The main ports in each watershed are shown for a detailed comparison.

Finally, Figure 2.2.5 shows a detailed comparison of the impacts of the budget, volume and duration of the activities at the main ports. Although these variables have small deviations at some ports (e.g., ports nº 31 and 36), they have significant variabilities at others (e.g., port nº 3). Furthermore, port nº 10 has different behaviors between the activities; for example, the average cost has a small variability, while the dredging volume has a large variability. Project managers may find these results useful at different stages in the development of a project to make more accurate estimations.

2.2.3 The case of the Punta Umbría inlet

Punta Umbria (port nº 8) is located inside the River Tinto-Odiel estuary, facing the Gulf of Cádiz. Two ports managed by the APPA are located inside the estuary, at a distance of 2 km from the mouth of the estuary. Since the late 50s, many new industrial and tourist activities have been developed in the surrounding area, with the consequent occupation of natural landscapes and the alteration of the natural behavior of the ecosystem. The presence of these activities resulted in a reduction in the magnitude of the natural agents that maintained the stability of the navigational channel. Hence, during the last decades, there has been a progressive increase in the magnitude and frequency of the sedimentation at the estuary mouth. To maintain the navigation channel and guarantee safety conditions, periodic and urgent dredging are necessary. Four interventions were done in the period 2004–2014 with a total cost of 4,558,214.14 €. As mentioned before, the volume of sediment mobilized was the second highest (438,587.92 m³), representing 15% of the total volume dredged since 1993.

Results from the study

Comparing this port with the other Andalusian ports with a significant number of interventions (3 in nº 10, 3 in nº 22, 11 in nº 23, 4 in nº 3, 6 in nº 31, 4 in nº 36 and 3 in nº 50), the average price of dredging 1 m³ is one of the highest average prices (Figure 2.2.5-a) which provides an average magnitude per intervention of 1,140,000 €. Also, results indicate that the average price in Punta Umbria of 10.39 €/m³ was similar at different interventions, with values between 8.88–11.03 €/m³. However, for other sites such as nº 23 deviations are significantly higher.

Figure 2.2.5-b shows liquidation budgets of the interventions at the main ports. Punta Umbria is one of the ports where more budgets were set aside for dredging interventions. In this case, there are very notable differences between the budgets: while the deviations are, in average, in the middle of the main ports, they are significantly higher than for the results depict in Figure 2.2.5-a.

Figure 2.2.5-c shows dredging volumes through the different interventions in the main ports. Volumes are similar in each intervention with low deviations. Box-plot analyses show that Punta Umbria spends in dredging interventions above average, in spite of dredging lower volumes. Nevertheless, managers should focus on others ports where the deviations are larger to improve efficiency and reduce costs.

As shown in Figure 2.2.5-c, one of the main problems in Punta Umbria is the amount of sediment that is mobilized. At least one intervention is required every 2 (maintenance) or 4 years (urgent) to maintain the navigability of the channel. Since most of the sediment is transported alongshore under storm conditions, we searched for correlations between the storms (frequency,

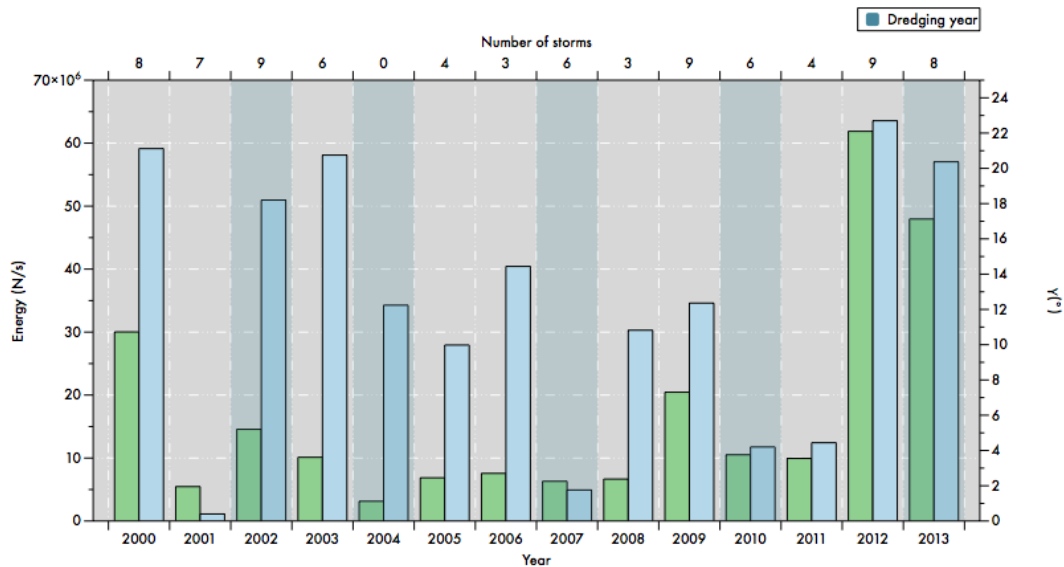


Figure 2.2.6: Relation between the number of storms, wave energy and wave angle and years of the dredging operations.

the number of storms and associated energy flux) and the dredging operations (dates, volumes and urgency/maintenance). Figure 2.2.6 shows the relation between the number of winter storms, the energy associated and its main angle of propagation, and when the dredging operation was done. After a stormy winter (i.e. 2002—2003), a subsequent dredging intervention was done (summer 2004). The winters that followed (2004, 2005 and 2006) were of low energy, and no interventions were necessary. However, during the winter of 2007, the number of storms slightly increases and finally a dredging was done in summer 2008. A very energetic winter in 2009 followed this operation, resulting in a maintenance intervention in 2010. The winter of 2011 was mild, whereas in the winter of 2012–2013 a total of 9 storms arrived. Hence, another intervention was done in 2014.

From these analyses it can be observed that one operation is required every four years at Punta Umbria; this frequency reduces to two years if stormy winters arrive. For this site one of the main forcing factor that must be considering when dredging is the littoral drift, so alternative solutions should focus on reducing this rate.

2.3 Dredging at Andalusian ports: the case of the Guadalquivir estuary

2.3.1 Guadalquivir estuary historical overview

Most important geomorphological changes in the SW of the Iberian Peninsula occurred ~ 6500 B.C., when the sea level rise caused the appearance of a huge bay (Gulf of Tartessos), which gradually dried and originated the current Guadalquivir marshes. First settlements in the valley date from VIII century B.C, where early civilizations ensure passage through the river with small dikes. Although Seville was a small island at that time, it was a commercial enclave since the Guadalquivir was navigable to that point (Álvarez, 2011).

During Roman rule, in the middle of I century B.C, *Hispalis* (Seville) was one of the most relevant cities of *Baetica*. Not only minerals, but olive-oil trade and conservation and curing of fish were the main economic drivers. The *Baetis*' frequent overflows conditioned the urban development, being one of the reasons that impelled the construction of a defensive wall.

Next remarkable changes occurred with the arrival of Muslims in VIII century B.C. The "*al-wadi al-Kabi*" (big wash) allowed the entrance of ships from Sanlúcar de Barrameda, Puerto de Santa María and Algeciras; connecting the maritime transport to farm production (Girard, 2006). The first law that controlled the behavior of the river users dates from this period. Riverine protections and port installations were also renewed. Both the presence and the importance of the port were also reinforced.

When Christians reconquered Seville in XIII century, they found a city that revolved around the port. Indeed, sailors and merchants privileges were increased and merged. The maximum splendor reached with the Indian trade decayed in XVII century, due to the continuous sedimentation of the navigational channel (Athané, 2012). The dredge of the Sanlúcar sandbar did not avoid the shift of the port seawards.

It was between mid-XIX and XX centuries when the most important interventions in the Guadalquivir margins were performed, shortening the main course ~40 km. These human alterations aimed to preserve the navigability as far as Seville (Vargas and Paneque, 2015). The flow regime, with mean values of 185 m³/s, minimum of 10 m³/s and overflows of 5000 and 9000 m³/s (return periods of 5 and 100 years, Vanney, 1970), was regulated with the construction of the Alcalá del Río dam in 1931, at 110 km from the mouth. This construction, that has distorted the tidal dynamics in the estuary, also altered the flow regime: the freshwater inputs to the estuary have decreased by an average of 60% (from approximately 5000 hm³/year in 1931–1981 to 2000 hm³/year in 1981–2000), with a greater reduction in dry years (Ruiz et al., 2015).

This historical overview of the low Guadalquivir marks the mutual conditioning and interaction between the socio-economic sectors throughout time and the estuarine morphology, especially the dependence of the port's activity to the Guadalquivir's navigability.

2.3.2 The Guadalquivir estuary nowadays

The Guadalquivir estuary is located in the SW of the Iberian Peninsula and flows into the Gulf of Cádiz, normally subjected to low river discharges. It comprises the last 110 km of the Guadalquivir river, where the first 90 km are navigable. The river has a total length of 680 km and a drainage basin of 63,822 km² (Granado-Lorencio, 1991). In the estuary and surroundings inhabit 1.7 million people, spread over 90 population settlements. Currently, the estuary is one of the most important socio-economic areas in the southern part of Spain, where the management is extremely harsh due to the interaction of numerous conflicting stakeholders.

The water and the exchange of material between the ocean and the fresh water mass result in a high degree of biodiversity and plentiful fishing resources. However, the priority that was given to other uses, such as navigability and agriculture, in addition to unrestricted fishing, ultimately resulted in the overexploitation of resources and an overall alteration of habitats and the system. Green intensive farming and paddy cultivation, fishing, recreational and commercial navigation, fisheries and aquaculture, salterns, the Doñana National Park, the urban development and

associated infrastructures, with an extensive road network and irrigation channels, are the main uses and elements present in the estuary (Medio Ambiente, 2009).

The large-scale human-made modifications in the margin in the XX century, together with the pressure for agricultural land, lead to widespread drainage of the marshes, modifying the freshwater regime. Indeed, more than 80% of the original marsh surface area was transformed, representing one of the largest losses of marshes in Europe (Ruiz et al., 2015). Today, the Guadalquivir paddy marshes are the most important rice-production areas in Spain in terms of cultivated area (36,800 ha: 34% of the national total and 92% of the regional total) and gross production (300,000 Tm per year: 40% of the national output). The productivity of these fields averages 8 Tm/ha, which is the highest in Europe (Vargas and Paneque, 2015).

Recently, as a result of the Aznalcollar mining spill, the remaining marshes of the Doñana area were completely isolated from the estuary with dikes and floodgates Contreras and Polo (2010). Salt production and aquaculture have also contributed to this isolation. This process resulted in the channelization of the estuary, drastically reducing the number of tidal creeks and the surface of intertidal zones (Díez-Minguito et al., 2012). In the channel, the waterway is periodically dredged from its mouth to the Port of Seville, to guarantee a minimum navigation depth of 6.5 m.

Since 1993 the management of Seville's port and the navigation channel is entrusted to the Port Authority, although the Guadalquivir Hydrographical Federation (CHG) is the responsible for preserving the water mass in the ecosystem. A project to improve access to the port was presented in 2000 by the Port Authority, with the utmost objective of receiving larger ships. This project involved two major actions: the construction of a new lock (inaugurated in 2010) and the deepening of the navigation channel. This widen and deepen project (from 6.5 m to 8 m) of the channel (80 m wide and 90 km long) included other actions that would have significantly modified the ecosystem (e.g.: reconfiguration of the inner channel, banks, land uses, etc.). It should be noted that the social and environmental impacts were not properly taken into consideration, which resulted in conflicts between different stakeholders: ones supporting the project, led by the Port Authority, and others against, gathering the rice agricultural sector, ecologist associations and the Doñana's national park. The assessment of the environmental impact of the project followed in 2003 and 2005, remarking the importance of banks protection, changes in the salinity and turbidity distribution, and the overall impact on the fauna and flora in the ecosystem. To that purpose, a scientific committee was settled, resulting in the publication of the document Ruiz and Losada (2010): Methodological proposal for the diagnosis and forecast of human action in the Guadalquivir estuary.

Since then, a large number of studies with valuable information about the state and behavior of the Guadalquivir estuary has been revealed, as described in Section 1.2. These studies, based on the data collected associated to the proposal of 2010, support the overall diagnosis emitted by the scientific committee: the Guadalquivir estuary is in poor condition. 80% of the year the river flow is not able to favor the stratification, essential for life development and turbidity control. Since under these conditions the estuary is well-mixed, where the suspended matter severely limits the photosynthesis and the biodiversity (Losada, 2011). As the impact of deepening the channel on the ecosystem is uncertain, further assessments should be done and more specific measurements proposed to execute this kind of project. Therefore, the project was rejected. Since

then, the attempts to deepen the navigation channel, or modify the morphology of the banks, have been rejected by the corresponding authority based on the scientific committee decision. Vargas and Paneque (2015) fully details the evolution of the generated conflict by the dredging. As the impact of deepening the channel on the ecosystem is uncertain, further assessment should be done and more specific measurements proposed.

Dredging by the Port of Seville in the Guadalquivir estuary

The Port of Seville, the only inland seaport in Spain, is located in the Guadalquivir estuary, at 90 km from the mouth. Navigation is performed in the navigation channel, cataloged as the European waterway E.60.02. The harbor surface is 850 ha, with a logistic zone linked by multimodal transport corridors.

Between 2012–2014, the Port of Seville received an average of 1060 ships. Mean total cargo per year is 4.4 million tonnes. General merchandise represents half of this value (53%), followed by solid bulk (40%) and liquid bulk (7%). Container mobilizes the 50% of total cargo, while ro-ro represents ~ 6%. Regarding the solid bulk traffic, the most important correspond to scrap, grain and flour, and fertilizers.

Maintenance dredging works are periodically carried out to maintain the operational capacity and security conditions of the navigation channel. These works agree with the impact declaration of 2003 (General Secretary of the Environment, 2003). The main characteristics of the dredging in the Guadalquivir estuary are depicted in Figure 2.3.1. The mean volume of mobilized material per year is $\sim 6.5 \times 10^5 \text{ m}^3$, with an average price in the period 2010–2012 of 3 €/m³. Higher dredging volumes per year are above $1.1 \times 10^6 \text{ m}^3$. Higher dredging costs in a year are above €2.5 mln. Between 2010–2014, the total cost of dredging was €6.48 mln. The dredged volume between 1995–2004 represented 7.2% of the Spanish Port System, while in 2005–2012 the 3%. Between 1995–2010, 24% of the dredged material were disposed in the sea, 10% reused and the rest (66%) was not profitable. According to (Fernández and Novo, 2007), since 1980, the dredging of the navigation channel pumped $4 \times 10^6 \text{ m}^3$ of dredged sediments to dike precincts, building 0.5–3 m high deposits along an 8 km stretch on tidal marshes of the estuary. The dredge is more intense in the first ~ 20 km closest to the lock. Regardless this stretch, the dredging intensity has moved landward in recent decades, focusing between pk 25 and 60 from the lock.

	1964-1980	1995-1998	1999-2004	2005-2012
Dredged volume (x10 ⁶ m ³)	12.25	3.3	3.95	3.22
*Mean dredged volume per year (x10 ⁶ m ³)	0.72	0.83	0.66	0.4

*Note: Values in periods in light blue are equally distributed

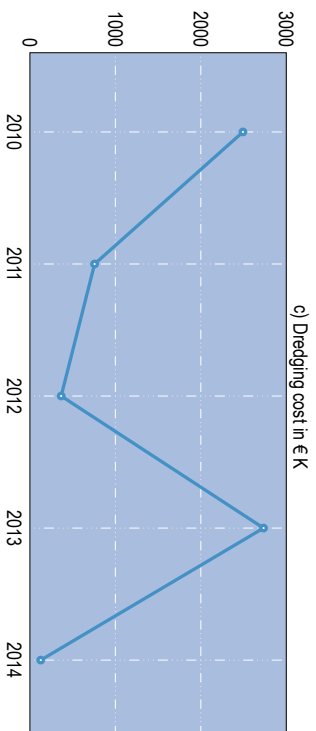
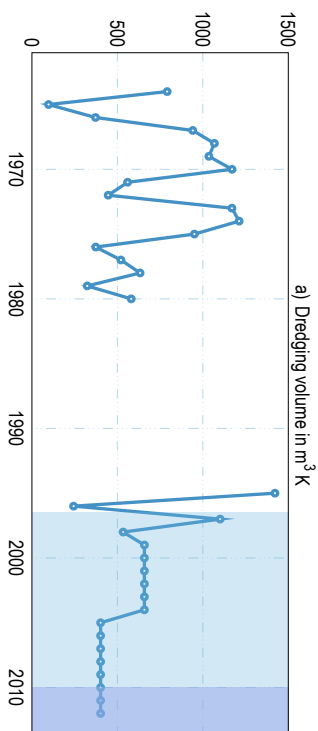
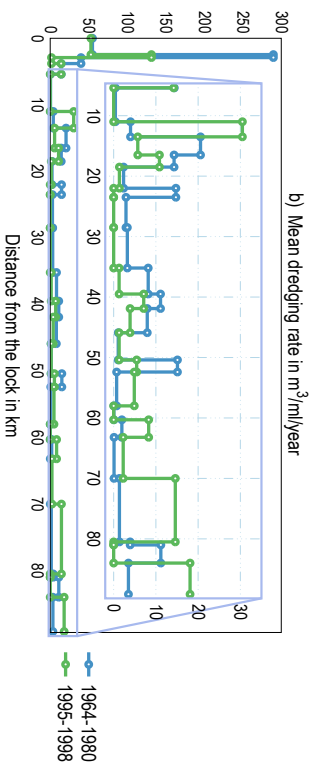


Figure 2.3.1: Table with dredging volume information (up-left), time evolution of this dredging volume (panel a) and along-channel distribution (panel b). The dredging cost for the Port Authority of Seville are also included (panel c).

2.4 Results & Conclusions

The assessment of the main drivers of dredging and different economic indicators point that dredging is a global activity that will continue to grow in the near future. From the past years, the global dredging turnover has more than doubled, with a notable rising in the seaborne world trade, which is the major driver for the dredging industry. Regarding this trade, European and Spanish port are not an exception. In Europe, ports are of vital economic interest, handling up to 90% of Europe's international trade and 40% of the volume of ton-kilometers carried out in intra-Community trade. In Spain, the Spanish Port System account for 53% of the Spanish foreign trade with the European Union and 96% with third countries. This activity is reflected in dredging and the amount of mobilized material, with an increase of 7.2% in the past decade for the Spanish ports. The southwestern of the Iberian Peninsula, close to the axis of one of the world's major maritime routes, accounts for several estuaries and tidal inlets. In some of these, dredging is intense to maintain the inland ports' activity.

Since dredging has increased in recent decades, the complexity of their management, with more strict demands for considering multiple economic, environmental and ecological factors, has grown too. The European legislation agrees with this concern, promoting numerous policies to ensure the protection of the environment, as well as the sustainability of the economic development. Most of the times, this resulted in continuous conflicts between different stakeholders, posing a challenge to managers, and engineering and scientific community.

In the ports managed by the Regional Government of Andalusia, the project *Dragaport* has represented a breakthrough regarding the dredging interventions. This dissertation used an object-relational database, from the abovementioned, to assess the relative importance of the 70 regional dredging projects executed between 1993–2015. In the inlet of Punta Umbría, four interventions were done in the period 2004–2015, which represent the 15%, the second highest in the region. The average price per intervention is 10.39 €/m³, which belongs to the most expensive group. The occurrence of the interventions in the inlet was related to storms events, namely their frequency, number and their associated energy fluxes. These analyses indicated that one operation is required every four years at Punta Umbría; that rate reduces to two years if stormy winters occur. Since the economic and environmental impacts are elevated, regional managers are demanding a more efficient alternative. A possible alternative is presented in Chapter 5.

Regarding the Guadalquivir estuary has always been a hot spot for environmental and human conflicts. It was between mid-XIX and XX centuries when the most important interventions in the morphology, particularly in the margins, were executed. The main course was shortened ~ 40 km, aiming the preservation of the navigability as far as Seville. Maintenance dredging works are periodically done to this purpose. In response to the project proposed by the Port Authority of Seville to widen and deepen (from 6.5 m to 8 m) the navigation channel, a scientific committee was formed. Their role was the evaluation of the environmental impact in the estuary as a consequence of the dredging intervention. The diagnosis emitted by the scientific committee, as well as associated studies, pointed that the Guadalquivir estuary is in poor condition, namely for life development and turbidity control. Thus, the proposed dredging was not recommended. As the impact of deepening the channel on the ecosystem is uncertain, further assessment should be done and more specific measurements proposed. This Thesis deepens on this topic in Chapters 3 and 4.

ANALYSIS OF PROCESSES IN THE GUADALQUIVIR ESTUARY

The amplification in the tidal range is one of the most common effects in estuaries as a response to deepening and narrowing the channels. This shift in the tidal motion, with a relative increase in high water and a decrease in low water levels with respects to former may improve the navigation conditions. However, this shift may enhance flood risks, lowering of ground water table, increase the suspended sediment matter concentration and displacing the salinity intrusion further upstream. As a consequence of losing intertidal areas, ongoing deepening may favor flood dominance while the river's flushing capacity decreases. The effective hydraulic drag is reduced, increasing the tidal asymmetry and the suspended matter concentrations too, in a feed-back loop. Besides, the role of river flows on tidal wave propagation is relevant in this cycle, and cannot be captured with common linear models and approximations.

This chapter focuses on the processes that are relevant to understand the estuarine dynamics in the Guadalquivir and their implication with dredging and channel deepening. Section 3.1 presents the study area and its basic characteristics. Section 3.2 assess the estuarine salinity structure and circulation, analyzing the dependence of the salt intrusion on the forcings agents. Section 3.3 focuses on the tidal-fluvial interaction, namely in the processes and controlling mechanism of the non-stationary response of tidal, and subtidal water levels and currents, to high discharges. Results and observations from previous Sections were used to assess the feed-back loop in the Guadalquivir estuary as a response to deepening the navigation channel.

3.1 The Guadalquivir-river estuary: Study area

The Guadalquivir estuary is located in the SW of the Iberian Peninsula ($36^{\circ}43'N-37^{\circ}32'N$, $5^{\circ}56'W-6^{\circ}30'W$) and flows into the Gulf of Cádiz, in the North Atlantic Ocean (Figure 3.1.1). Its natural course has been deeply modified during the last two centuries, with channelization, dredging works and the occupation of a substantial part of its wetlands (Section 2.3). From its mouth, the estuary extends 110 km upstream, the first 85 km of which are navigable. The Guadalquivir River Estuary (GRE) decreases in width from ~ 800 m at its mouth to ~ 150 m at its head. The estuary is thus slightly convergent, with a convergence length-scale of 60 km. It has an average depth of 7.1 m and a minimum depth of 6.5 m in the *thalweg*, which is maintained by periodic dredging. The river branch in Seville hosts the Port of Seville, which is separated from the main channel by a lock.

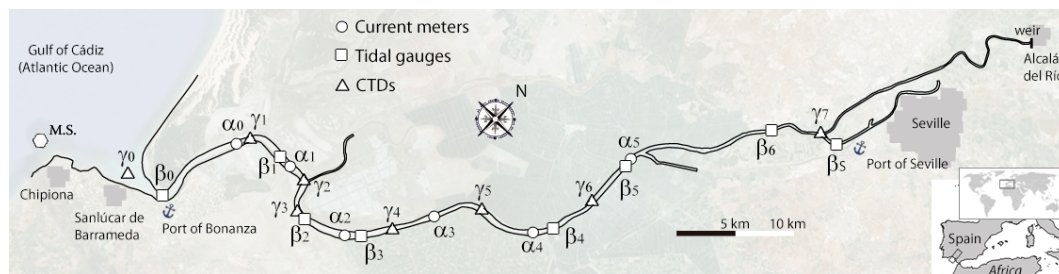


Figure 3.1.1: Guadalquivir River Estuary (SW Spain) and monitoring stations of relevance to this study: current meter (circles, α_k), tidal gauges (squares, β_k), water quality probes (triangles, γ_k) and meteorological station (hexagon, M.S.).

During 2008-2011 a comprehensive research study was carried out with the purpose of regulating the different economic and environmental uses of the estuary (Ruiz and Losada, 2010). This involved the installation of a remote, real-time monitoring network (RTMN) (Navarro et al., 2011) which accounted for tidal gauges, current meters and environmental quality stations, amongst others (Appendix 3.A). The analysis of the data produced by the RTMN has undoubtedly contributed to an ample characterization of the estuarine processes and has led to a breakthrough in our knowledge of the Guadalquivir estuary.

The tidal wave penetrates the estuary from its only mouth near Sanlúcar de Barrameda to the Alcalá del Río dam. The dam is the last control point of the river flow and constitutes a barrier for the tide, which arrives with sufficient energy to be reflected and interact with the incident wave. This interaction causes the tidal elevations to show hypersynchronous behavior and produces a quasi-standing wave tidal regime in the upper third of the estuary (>45 km). Hyposynchronous and synchronous stretches are the lower (0-20 km) and the second third, respectively (Díez-Minguito et al., 2012).

The climate in the GRE catchment area is temperate (Mediterranean). Freshwater discharges exhibit marked intra-annual and seasonal variations in magnitude and duration. The Alcalá del Río head dam regulates about 80% of the fresh water contributions to the estuary. From 1980–2016, the reduction in the mean freshwater discharge is 54% in comparison with the period 1931–1980. Dry periods, which yield low discharges of less than $40 \text{ m}^3/\text{s}$, occur for over 70% of the year (period 1980–2016). These freshwater discharges are sufficient to compensate for the evaporation loss, thereby causing the estuary to be positive in terms of longitudinal

salt distributions. These abovementioned conditions are the estuary's *normal* conditions (Díez-Minguito et al., 2012). The wet season yields relatively short and intense periods of rainfall. Despite the upstream regulation, freshwater inputs into the estuary are frequently characterized by high discharge levels exceeding $400\text{m}^3/\text{s}$ (and lower than $6000\text{m}^3/\text{s}$) that accumulate over a few days.

Under normal flow conditions, water motion and solute transport processes in the GRE are dominated by tides. The estuary is flood dominated. The tidal water level range at the mouth does not exceed 4m (mesotidal). The most important constituents are semidiurnal, particularly the M2, attaining a ratio of ~ 0.1 between the two main diurnal constituents and semidiurnal constituents. Channel convergence and interactions between incoming and partially reflected tidal waves cause tidal elevations to increase. Tidal amplification is more significant during neap tides than in spring tides. Mixing by tides overwhelms stratification induced by low river flows. Under these conditions, the GRE features a well-mixed to partially mixed (near the mouth) water column and weak gravitational circulation (Díez-Minguito et al., 2013), as detailed in Section 3.2.

These conditions are altered during periods of high discharge. Observations show that with fresh water discharges greater than $400\text{m}^3/\text{s}$, the GRE is no longer tidally dominated, the potential energy of the water column increases, and the saline intrusion point moves to the mouth. Díez-Minguito et al. (2013) documented adjustment times over two weeks as a response to $Q_d \approx 531\text{m}^3/\text{s}$, and found a saline intrusion front propagation speed of $4\text{cm}/\text{s}$.

In the case of the Guadalquivir River Estuary (GRE), the impact of high levels of run-off into the estuary on biogeochemical fluxes and on the recruitment of small pelagic fish has been analyzed by Fernández-Delgado et al. (2007) and Guerreiro et al. (2013), respectively. Wang, Winterwerp, and He (2014) studied the relationship between suspended sediment concentrations and the tidal amplification from water level data. The effects of high river flows on surface turbidity patterns and mean sea water levels over the inner continental shelf were analyzed by Caballero et al. (2014) and Gómez-Enri et al. (2015), respectively. The tidal-fluvial interaction and related non-stationary hydrodynamics of the GRE in response to high river flows have received less attention, despite their industry and research implications (Ruiz et al., 2015). Section 3.3 deepens on this topic.

3.2 Saline intrusion mechanisms

Despite the analysis of the data produced by the RTMN, which has undoubtedly contributed to an ample characterization of the estuarine processes and has led to a breakthrough in our knowledge of the Guadalquivir estuary, much remains to be investigated regarding the salinity structure. The landward transport of salt is controlled by both natural forcings and human activities. The latter are mainly those related to the periodic dredging of the shipping channel performed by the Port of Seville, the overexploitation of aquifers, the direct uptake of fresh water from the estuary for agricultural purposes, and the management of the Alcalá del Río head dam. For the rational management of these conflicting activities, it is essential to characterize and predict the saline intrusion. In this work, the saline intrusion is determined as the distance from the location γ_0 to the point where the salinity reduces to the 2 practical salinity units (psu). Neither the influence of flow exchange in the transport of salt nor the relative influence of the climate forcing agents (mainly tides, wind and freshwater discharge) on the salt intrusion has been studied.

Focusing in these questions, we investigate the mechanisms that drive the salt transport by using the extensive dataset of the RTMN. The baroclinic circulation is characterized in terms of estimations of the effective turbulent viscosity coefficients along the lower half of the estuary. Power-law relationships are proposed to assess the relative influence of tides, river flow, and wind forcing on the saline intrusion. This analysis allowed us to develop a stochastic model based on first order Markov Chain Monte Carlo (MCMC) simulations to predict the saline intrusion, as studied in Chapter 4. Stochastic methods for saline intrusion in coastal waters are far less common than deterministic approaches (see, for instance, Hansen and Rattray, 1966; Savenije, 1993; Monismith et al., 2002; MacCready, 2004), but include naturally the assessment of the uncertainty in the predicted results (Herckenrath, Langevin, and Doherty, 2011).

3.2.1 Hydrodynamics and salt structure classification

A simple characterization of the salt structure regarding the Peclet number (Dyer, 1997). It is defined as $P = u_d/u_t$, being u_d the freshwater discharge velocity and u_t the tidal current amplitude, suggests that estuaries are well-mixed when $P < 10^{-2}$, and stratified when $P > 10^{-1}$. In the Guadalquivir case, mean P values vary from $P = 6.7 \times 10^{-3}$ to $P = 2.9 \times 10^{-2}$ for low and high freshwater discharges, respectively. These results evidence that, despite being a well-mixed estuary, stratification increases with increasing river flow, in particular during peak discharges.

This analysis is completed with an along-channel assessment with Hansen and Rattray (1966) classification system. Two hydrodynamic non-dimensional parameters need to be computed: the circulation and the stratification parameters. The first one is the coefficient between the near-surface current u_s to sectional averaged flow, in our case, in the water column U_{col} . The larger the circulation parameter, the stronger the baroclinic circulation. The stratification parameter is defined as the ratio of the top-to-bottom salinity differences δS to mean salinity over the section S_0 . The weaker the water column stratification, the smaller the stratification parameter will be. Type 1 estuaries show no vertical structure in net flows, in Type 2 the net flow reverse with depth and Type 3 exhibit strong gravitational circulation. Further explanation and examples can be found in Valle-Levinson (2010).

According to Figure 3.2.1, lower and mid stretches exhibit larger stratification parameter during high flow than low flow conditions. Overall, the circulation parameter is greater closer to the mouth. In the upper stretches both the stratification and circulation parameter are lower. During low flow regime, the estuary falls in class Type-2a, which indicates that the estuary is well mixed. During high flow regime, the stratification and circulation increases, moving to 2b and 3b regions. This rise is noteworthy during high flow conditions in α_0 , related to stronger baroclinic circulation.

3.2.2 Baroclinic circulation

Under normal conditions, the Guadalquivir is a positive estuary and its horizontal density gradient is the driving force for the gravitational circulation, which involves a vertically varying pressure gradient. A simple but reasonable approximation for analyzing the influence of the density gradient on the circulation is condensed in the following tidally-averaged equation (e.g.

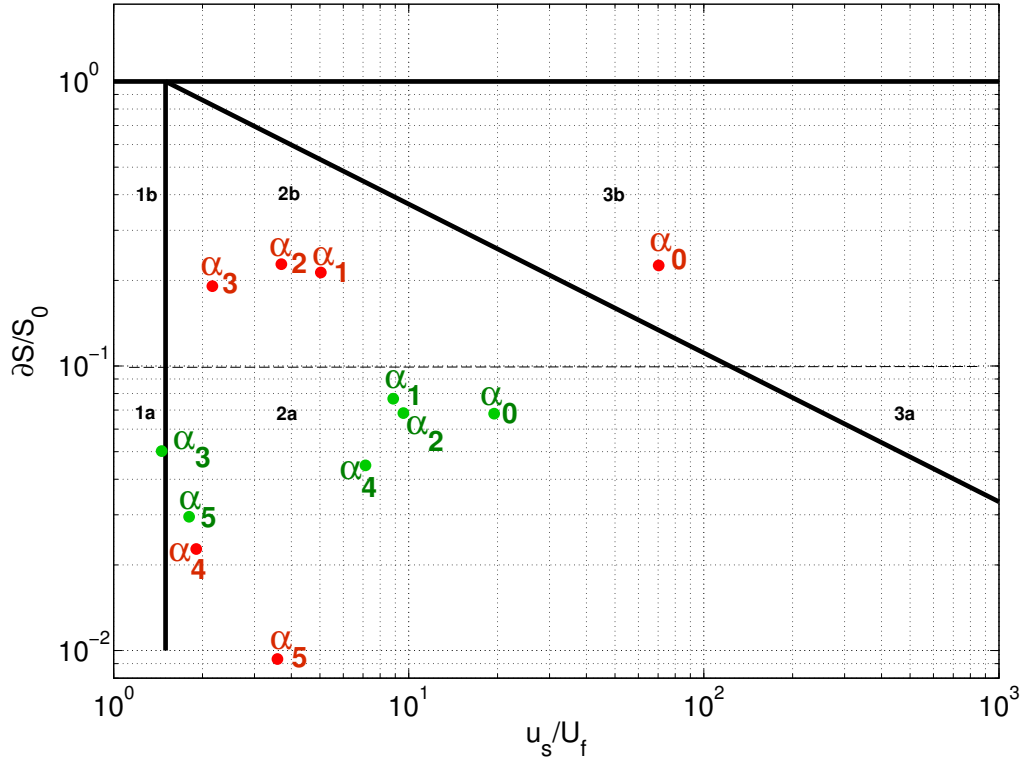


Figure 3.2.1: Hansen and Rattray (1966) Diagram, displaying the location of the current meters and their location during low (green) and high (red) flow regime.

Geyer, 2010; Hansen and Rattray, 1966):

$$gz \frac{\partial \rho}{\partial x} + \rho g \frac{\partial \eta}{\partial x} = \rho N_z \frac{\partial^2 u}{\partial z^2} \quad (3.1)$$

where ρ is the density, g is the gravitational acceleration, η is the elevation of water surface, N_z is the eddy viscosity coefficient (which is assumed constant throughout the water column), and u is the vertical current profile. Equation 3.1 relates the pressure gradient forces of the horizontal density gradient and the surface slope to the frictional term. Assuming no wind stress at the surface and imposing a slip condition at the bottom, Equation 3.1 can be integrated directly to obtain the cubic profile:

$$u = \frac{g\lambda(h^3 - 4z^3)}{24\rho N_z} + u_0 \quad (3.2)$$

where h is the water depth, λ is the longitudinal density gradient $\lambda = \partial\rho/\partial x$ and u_0 is the vertically averaged runoff velocity per unit width. The applicability of Equation 3.2 is restricted to tidal channels where lateral circulation is weak in comparison with the along-channel circulation, and to well-mixed conditions. During high flows, the pressure gradient due to the surface slope

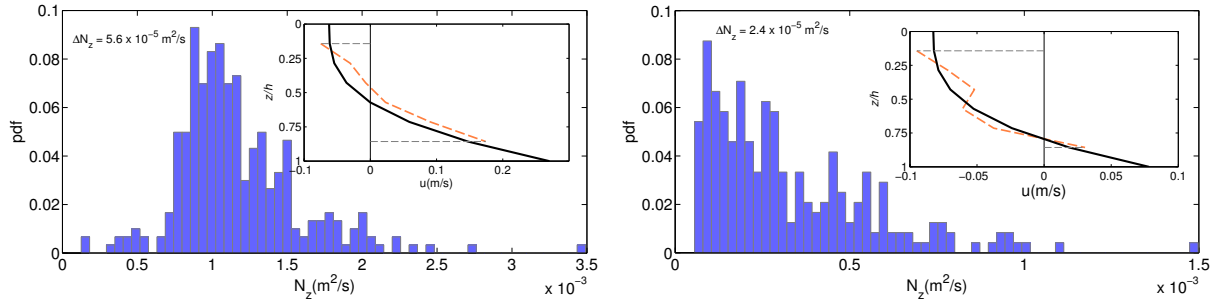


Figure 3.2.2: Main panels: Probability distribution function (pdf) of the fitted N_z coefficients at α_1 (left) and α_4 (right). Bin sizes are $\Delta N_z = 5.6 \times 10^{-5} \text{ m}^2/\text{s}$ and $\Delta N_z = 2.4 \times 10^{-5} \text{ m}^2/\text{s}$ for α_1 and α_4 , respectively. Insets: Observed (orange dashed line) and modeled (black solid line) tidally-averaged vertical current profile at α_1 (left inset) and α_4 (right inset) locations.

(barotropic component) reaches the higher values, the stratification increases, and N_z may exhibit a vertical structure.

The eddy viscosity coefficient N_z is estimated by fitting Equation 3.2 to the observed tidally-averaged vertical current profiles at moorings α_1 and α_4 during low flow conditions. The 94 and 75 percent, respectively, of the obtained correlation coefficients R were larger than 0.75. Figure 3.2.2 shows one example of the observed and modeled residual current profiles at both moorings and the histograms representing the probability density functions estimated with the computed N_z . The order of magnitude of the observed residual currents is ~ 10 cm/s, somehow larger near the bottom in the location close to the mouth. The values of the eddy viscosity coefficients, which depend on the tidal flow (e.g. the spring-neap cycle) and stratification, range from 10^{-4} to $10^{-2} \text{ m}^2/\text{s}$. In our case, the mean eddy viscosity decreases upstream from $1.2 \times 10^{-3} \text{ m}^2/\text{s}$ in α_1 to $3.3 \times 10^{-4} \text{ m}^2/\text{s}$ in α_4 . This spatial variation of N_z is consistent with the fact that λ , during low river flows, attains its maximum value in the lower stretch of the estuary, specifically between α_1 and α_2 . Also, the tidal amplitude in α_1 is higher than in α_4 , since the tidal velocity increases as the tidal wave enters the estuary entrance. Further, upstream the general tendency of currents is to decrease upstream. Weak deviations in regards to the non-stratified behavior are possibly reflected in the greater variance of N_z at α_1 . These results will be used elsewhere to make short-term predictions of the saline intrusion using vertically-resolved hydrodynamic, computational models.

3.2.3 Saline intrusion Power Law

Figure 3.2.3 shows the relation between the saline intrusion X_2 and the tidal velocity range U_t at α_1 and the river flow Q_d . Tidal range and saline intrusion time series are in close correspondence with the low flow regime. Spring-neap and diurnal inequality variations can be observed in both curves. As expected, the dependence of the saline intrusion on the value of Q_d is stronger during high river flows. It can be also observed an amplification of the tidal range after the peak discharge around 6-Feb-2009. As a result of this discharge from the head dam, boundary shear stresses reduce, which is a consequence of the non-linear interaction between the tide and the suspended sediment dynamics (Wang and Fernández Bermejo, 2010). High river discharges enable the mud entrainment due to turbulence, prompting an extreme turbidity event and reducing the bottom resistance. This amplification of turbidity is also common in other turbid

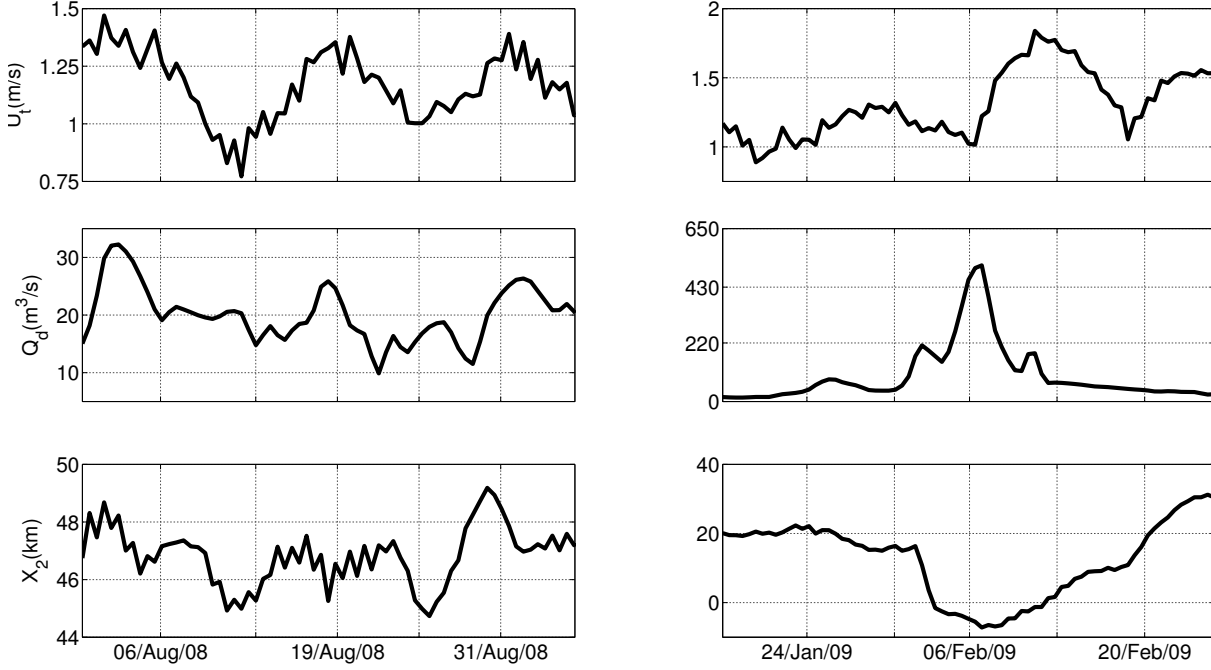


Figure 3.2.3: From top to bottom: Tidal amplitude, river discharge, and saline intrusion during low (left column) and high discharges (right column), respectively, at α_1 .

estuaries (King and Wolanski, 1996; Geyer and Nepf, 1996). The Guadalquivir estuary suffers periodical extreme turbidity events and is, in fact, one of the most turbid estuaries all over the world (Ruiz et al., 2013). These events severely limit the light availability, and thus, the biological productivity, determining the hypoxic conditions of the estuary.

In order to unravel the nature of the saline intrusion X_2 and the mixing mechanisms, the dependence of X_2 on the tidal velocity range U_t , and the river flow discharge Q_d , was analyzed. More specifically, it was found that X_2 , U_t and Q_d are related both in low and high regimes by:

$$X_2 \sim U_t^{b_1} \left(\frac{Q_d}{A_x} \right)^{b_2} \quad (3.3)$$

where A_x is the average cross-sectional area in the portion of the estuary with salinity greater than 2 psu (Monismith et al., 2002; Lerczak, Geyer, and Ralston, 2009; Ralston, Geyer, and Lerczak, 2010). The parameters b_1 and b_2 are constant coefficients that depend on the flow. Equation 3.3 expresses the idea that river flow controls to some extent the saline intrusion, which is modulated by the tidal variations of the current. Table 3.2.1 shows the results of the fitted coefficients, where saline intrusion is expressed in km, currents in m/s and discharges in m^3/s . Despite the crude fitting and the relatively large error bars in the computed coefficients, the exponents provide valuable information about the estuarine physics.

The obtained coefficient b_1 (for both regimes) indicates that the larger (smaller) the tidal current is, the larger (smaller) the saline intrusion is. This is consistent with an up-estuary salt flux which depends on U_t . The value of b_1 ranges from $b_1 \approx 0.06$ to $b_1 \approx 0.1$ for low and high

Table 3.2.1: Non-linear fitting coefficients for low (first row) and high (second row) river flows. The error bars represent the 95% confidence interval.

b_1	b_2
$(6.32 \pm 2.47) \times 10^{-2}$	$-(3.00 \pm 13.65) \times 10^{-3}$
$(1.25 \pm 2.89) \times 10^{-1}$	$-(3.17 \pm 0.77) \times 10^{-1}$

discharges, respectively. According to (Ralston, Geyer, and Lerczak, 2010), the theoretical scaling $X_2 \sim U_t^2$ for the saline intrusion indicates that tidal random walk, tidal pumping and lateral trapping are the most significant processes. The behaviour $X_2 \sim U_t$ is apparently related to lateral stirring and shear. When $X_2 \sim U_t^{-1}$, the main mixing process is gravitational circulation that usually occurs in estuaries with a long convergence length (Savenije, 2005), as the Guadalquivir estuary. Our results of b_1 , even within the error bars, differ from these theoretical values. However, tidal-pumping, lateral stirring, and baroclinic circulation should not be disregarded as the main salt transport mechanisms. The most plausible hypothesis is that our coarse description based on b_1 already includes these and other salt transport processes. In particular, a larger value of b_1 is obtained after a peak discharge mainly because of the tidal current range amplification produced by the mud entrainment, which interacts non-linearly with the tidal processes. Nevertheless, this behavior might also indicate an increase of the baroclinic circulation during high flows, as the value of b_2 confirms.

Regarding the fitted exponent for the river contribution b_2 , this varies notably from low ($b_2 \approx -0.003$) to high flows $b_2 \approx -0.3$. For the former case, the estuary is tidally-dominated and the intrusion is relatively insensitive to Q_d , whereas for high river flow, the estuary becomes fluvially-dominated, with discharge controlling the salt transport, being the tidal processes less significant overall. The scaling $X_2 \sim Q_d^{-0.3}$, close to the theoretical exponent 1/3 predicted by Hansen and Rattray (1966), suggests that gravitational circulation is greatly enhanced during the fluvially-dominated regime. The relative insensitivity of the saline intrusion to the discharge during low flows is interpreted in terms of non-significant inflows of freshwater when compared to the seawater volume present in the estuary, and thus with non-significant changes in the spatial limit of saltwater influence.

3.3 Tidal-fluvial interaction: spatial and frequency-dependent response of currents and water levels

Estuaries and tidal rivers are generally subject to forcing conditions, like fresh water discharge and tides, which highly vary in time. Understanding mutual interactions between river discharge and tidal waves is particularly important to improve the safety of navigation, assess flood vulnerability, analyze the effects of dredging intervention and to control water quality. This interaction, which is commonly referred to as tidal-fluvial interaction, drives water levels and currents, which also have consequences for morpho-hydrodynamics and ecosystems. In river systems where fresh water discharges are highly regulated (e.g., the Guadalquivir River Estuary in the SW Spain, Ruiz et al., 2015), tidal-fluvial interaction processes can be even triggered by human activities.

Under low enough river discharges, water levels and currents can often be obtained as a

linear superposition of tidal and river contributions (e.g. Godin, 1999). However, non-linear interactions between the two and non-stationary behaviors induced by short-scale variabilities in discharge is the rule rather than the exception (Hoitink and Jay, 2016). River discharge changes tidal and subtidal levels (LeBlond, 1978; Jay and Flinchem, 1997; Jay et al., 2014; Alebregtse and Swart, 2016), contributes to the dissipation of tidal energy (Godin, 1991; Horrevoets et al., 2004), reduces wave celerity (Godin, 1985; Savenije et al., 2008), and alters the stability of the water column by increasing the potential energy and/or by generating additional turbulence that changes the bed stress, which in turn alters tidal propagation (Jay and Musiak, 1994; Burchard and Hofmeister, 2008; Winterwerp, Lely, and He, 2009). Tides propagate further upstream than the salt intrusion point and the reach of semidiurnal tidal current reversal, affecting river water levels and flows (LeBlond, 1979; Buschman et al., 2009; Guo et al., 2015).

Tidal-fluvial currents and water levels are time-varying phenomena whereby energy is distributed between different characteristic frequencies or harmonics. The transfer of energy between frequencies (in addition to dissipation and inputs of energy within the system) is dependent on non-linear hydrodynamic processes, the tidal forcing and the river discharge input level (Godin, 1985; Kukulka and Jay, 2003; Guo et al., 2015). For instance, the generation of sub- and over-harmonics of primary tidal constituents, i.e., those directly generated by tide generating potential, is attributable to non-linearities in wave propagation (Le Provost, 1991). The principal lunar tide, M2, the most energetic constituent of many estuaries, gives rise to higher levels of harmonics generation (e.g., the overtide, M4). The superposition of M2 and M4 creates tidal ebb-flood asymmetry in levels and currents (Speer and Aubrey, 1985; Friedrichs and Aubrey, 1988; Parker, 1991; Lanzoni and Seminara, 1998) and affects the transport of solutes and particulate matter. Two primary waves propagating through a non-linear medium mix frequencies. A mutual non-linear interaction between M2 and the principal solar constituent, S2, produces an overtide, MS4, and a fortnightly compound tide, MSf. Compound tides also generate ebb-flood asymmetry, but due to their long periods, they rather affect subtidal water levels (Buschman et al., 2009; Jay et al., 2014; Sassi and Hoitink, 2013; Guo et al., 2015). These changes in subtidal water levels as a consequence of dredging interventions are further assessed in Section 4.3.

A number of techniques have been developed for analysing interactions and for determining amplitudes and phases of the frequencies involved (Hoitink and Jay, 2016). Stationary harmonic analyses are typically used for tidal prediction (e.g. Pawlowicz, Beardsley, and Lentz, 2002). Non-stationary techniques such as short-time harmonic (e.g. Godin, 1999; Gallo and Vinzon, 2005; Guo et al., 2015) and wavelet analyses (e.g. Jay and Flinchem, 1997; Flinchem and Jay, 2000; Buschman et al., 2009) offer more insight into tidal-fluvial interaction dynamics. Sources of non-linear interactions between tides and river discharge can be traced through continuity and momentum equations (in particular, non-linear shallow water and friction terms) using the harmonic decomposition method (e.g. Dronkers, 1964; Godin and Gutiérrez, 1986; Giese and Jay, 1989; Parker, 1991; Gallo and Vinzon, 2005). This method assumes that levels and currents are described by a reduced number of fundamental tidal frequencies and a non-tidal contribution, allowing for the simple evaluation of the relative strength of those terms. Nevertheless, how the strength of such sources changes with time has received less attention, and especially in response to varying levels of river discharge.

The general objective of this section is to investigate along-channel tidal-fluvial interactions

in the inner GRE during and after high fresh water discharge episodes. The long-term goal is to provide reliable tools for navigation and flood risk management based on detailed knowledge of the underlying physical mechanisms of tidal-fluvial interactions. The better understanding of these dynamics would lead to better interpretations of dredging interventions. The present section focuses specifically on the identification and analysis of processes and controlling mechanisms of the non-stationary response of water levels and currents to high discharge events of $400\text{m}^3/\text{s}$ or larger taking normal conditions (discharges Q_d below $40\text{m}^3/\text{s}$) as a reference. This observational study is based largely on sea water level, current, and water quality measurements recorded during a monitoring campaign running from 2008 to 2011, extending the hydrodynamic analysis of Díez-Minguito et al. (2012). These authors limited their analysis to tidal transformation processes observed under normal conditions.

Several techniques described in Appendix 3.B are applied herein to achieve the following specific objectives. Non-stationary analyses of observations are performed in terms of a short-time harmonic analysis and continuous wavelet transform. These analyses allow for the evaluation of spatial and frequency-dependent responses in water levels, tidal ellipse parameters, and related variables, and they reveal dominant processes of the tidal-fluvial interaction such as the flow-suspended sediment feedback loop, treated in detailed in Section 3.4. The results on the spatial and frequency-dependent responses of water levels and currents to discharges are presented and analyzed in Section 3.3.1. This also identify major tidal-fluvial interactions, and key results on flow-suspended sediment feedback are also discussed. The main remarks drawn from this Section are summarized in Section 3.3.2.

3.3.1 Water level and Current responses

Water levels

Figure 3.3.1 shows the effect that discharge (panel (a)) has on the water elevation with respect the local mean sea level at the following two different stations: Seville (panel (b), and inset), located in the tidal river part of the system, and Bonanza (panel (d), and inset), located at the estuary mouth. The analysis interval shows discharges of less than $40\text{m}^3/\text{s}$ (the threshold proposed by Díez-Minguito et al., 2012 for low discharge), and discharges well above that value.

The detided water level at β_S increases by 3 m for $Q_d \sim 2000\text{m}^3/\text{s}$ (inset panel (b)), whereas for $Q_d \sim 4000\text{m}^3/\text{s}$, the value is slightly higher than 4 m. Near the mouth, where the estuary widens, the river discharge varies more gradually, and its effect on water levels is less significant. Larger cross-sections and larger ratios of the volume of water over tidal flats to that in the channel near the mouth yield lower elevations of less than 1 m for $\sim 2000\text{m}^3/\text{s}$ (inset panel (c)). This value, which agrees with satellite observations (Gómez-Enri et al., 2015), decreases further as discharge spreads over the shelf.

For such high values of Q_d , particularly a time after this peak events, water levels are no longer obtained as a simple superposition of tidal water levels and those associated with the fresh water discharge, as evidenced by damping in the semidiurnal oscillations around the peak discharge point (Figure 3.3.1, panel (b) and inset). At the estuary mouth, nevertheless, the linear superposition of tidal and fluvial contributions to η offers fair agreement, at least for the discharges shown in Figure 3.3.1, panel (a). The ratios between tidal amplitudes in Seville and those in Bonanza are 0.3 and 0.1 for discharge peaks occurring on 23/Jan/96 and 23/Dec/96,

respectively. These ratios suggest higher tide damping by the river flow in upper stretches. Under normal conditions, this ratio is ~ 0.9 for the time interval shown in Figure 3.3.1, and it is larger during neap tides than during spring tides because of shear stress dependence on the amplitude of the tidal flow. As a consequence, the tidal range difference between spring and neap tides decreases as the tidal wave propagates upstream.

The time variability of the frequency dependent behavior is explored through a CWT analysis. Figure 3.3.1 (panels (d) and (e) for Seville and Bonanza, respectively) shows the impact of high discharges on wavelet power spectra of the most significant tidal species, and it notably mirrors features listed above from the time series. Spring-neap color alternation is observed for Bonanza and Seville under normal conditions, although this pattern is less pronounced in Seville because differences in tidal ranges between spring and neap tides diminish upstream. Tropical and equatorial tides are also noticeable in the diurnal group. A weak in-phase annual variation in both species may be associated with the steric and atmospheric signal of the Gulf of Cádiz (Laiz et al., 2016). High river flows dampen the tidal species of diurnal and shorter periods, including overtides. Damping is also observed in the time series of water levels at both stations, and especially for Seville (β_S). A lower reduction in tidal amplitude due to the discharge is observed near the mouth (panel (c)) due to the weaker frictional damping by the river flow. Tidal damping is frequency-dependent. Discharge favors the generation of over-harmonics and compound tides (harmonics that are sums and differences of primary frequencies) although the former are damped faster as the tide propagates upstream by a river flow than when they are being generated (Matte, Secretan, and Morin, 2014).

The CWT analysis also shows that most of the power is concentrated in longer periods (8 hours and longer), and especially in fortnightly and monthly constituents (Figure 3.3.1 panels (d) and (e)). Non-linearly generated MSf variations in the subtidal water level (orange curves in panels (b) and (c)) are clear even though their amplitudes are over one order of magnitude lower than those of the semidiurnal tides. Larger MSf amplitudes are observed in the upstream station (panel (b)). These variations are partially modulated and as shown below, are generated by the river discharge. Compound tide MSf is in phase with the spring-neap tidal cycle, producing higher subtidal water levels during spring tides than during neap tides. This feature is common to many estuaries (Speer and Aubrey, 1985; Buschman et al., 2009; Sassi and Hoitink, 2013; Hoitink and Jay, 2016).

Currents and Tidal Wave Propagation

Figure 3.3.2 shows the effect of high discharge levels (panel a) on the time series of longitudinal currents (panel b) and CWT power spectra (panel c) at station α_5 . Figure 3.3.2 is the counterpart, in terms of currents, of Figure 3.3.1. The analysis interval includes a range of discharges of less than $3000\text{m}^3/\text{s}$ (panel a). The residual current decreases during impulsive fresh water discharge periods of an order of magnitude of $Q_d \sim 500\text{m}^3/\text{s}$ (such as those for 20/Apr/08 and 07/Feb/09), thereby causing the mean flow to be directed downstream (panel b, orange curve). During such events, fluvial current magnitudes are lower than those of maximum flood and ebb tidal currents, and thus positive and negative currents are still observed at station α_5 (panel b, blue curve). Without considering low-frequency, fluvial currents, tidal ebb currents are surface intensified due to inputs of potential energy associated with higher discharges (Jay and Musiak, 1994). Nevertheless, floods are still stronger than ebbs (falling tide exceeding rising

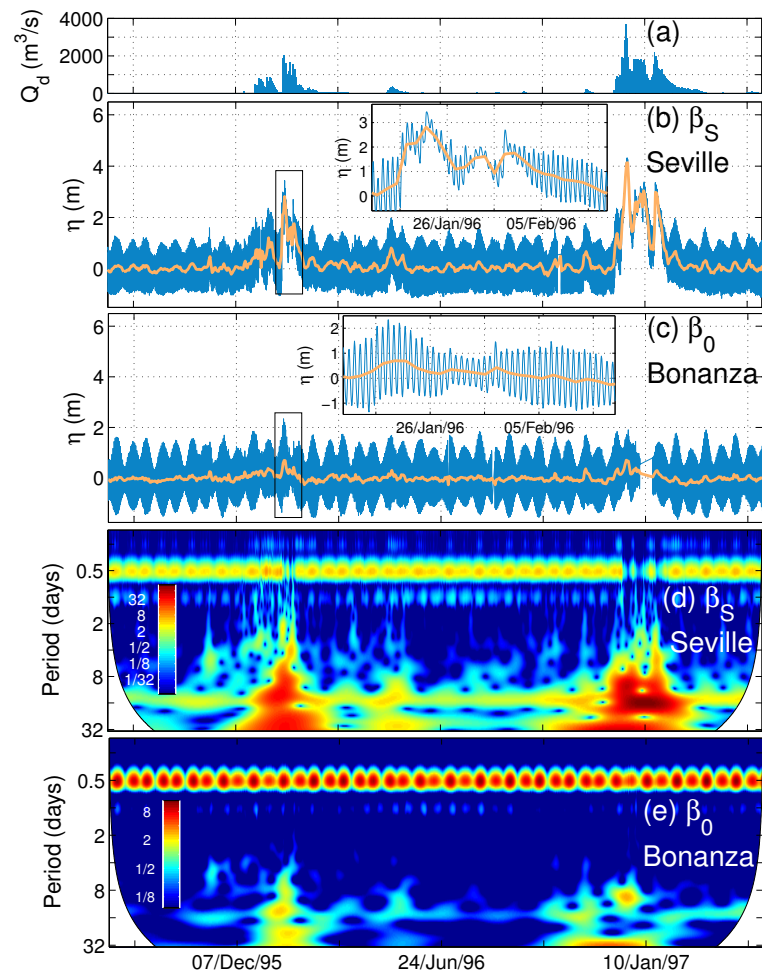


Figure 3.3.1: Panel (a): Time series of the fresh water discharge from the Alcalá del Río dam. Panel (b): Time series of elevation (blue curve) and subtidal, low-pass filtered elevation (orange curve) at β_S (Seville). Inset magnified image of the black box. Panel (c): The same as that shown in panel (b), but for the β_0 (Bonanza) station. Panel (d): Color plot of the Continuous Wavelet Transform power spectra of time series of water levels at β_S . The wavelet power is $\log_2(|Amp|^2/var)$, with Amp being the wavelet complex amplitude and with var as the variance of the time series. The white area limits the 95% confidence level (cone of influence). Periods are normalized as (e.g.) quarter-diurnal ~ 0.25 and semidiurnal ~ 0.5 . Panel (e): The same as that shown in panel (b), but for the β_0 station.

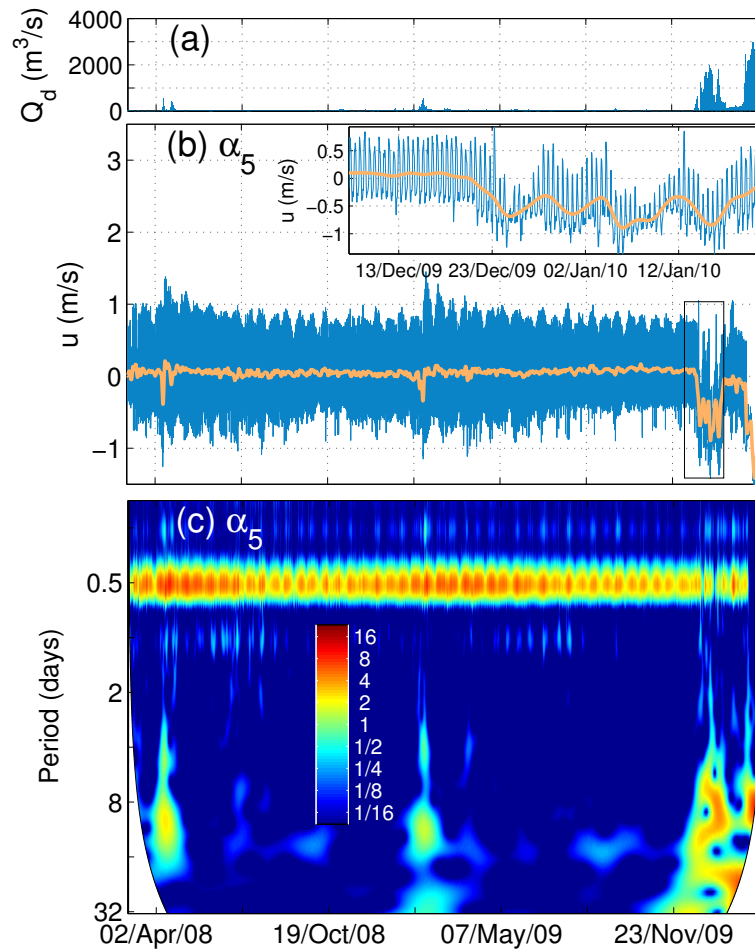


Figure 3.3.2: Panel (a): Time series of the fresh water discharge from the Alcalá del Río dam. Panel (b): Time series of along-channel current (blue curve) and subtidal, low-pass filtered currents (orange curve) at station α_5 . Inset magnified image the black box. Panel (c): Color plot of Continuous Wavelet Transform power spectra of the time series in panel (b). Settings are the same as those applied in Figure 3.3.1, panels (c) and (d).

tide in duration) according to the phase relationship between M2 and M4 constituents (Speer and Aubrey, 1985). After the 20/Apr/08 and 07/Feb/09 discharge episodes, the M2 amplitude increases. This amplification, which is shown in panels (b) and (c), lasts for over two months. Discharges of above $\sim 2000\text{m}^3/\text{s}$, such as those occurring during the winter of 2010, cause the salt intrusion to move off to the estuary mouth and induce fluvial currents of the same order or exceeding maximum flood and ebb currents. Considering the mean flow induced jointly by river and tidal motion, net currents are negative because fluvial currents outweigh tidal current asymmetry. The information provided through the CWT analysis on currents (panel (c)) is largely similar to that on water levels. The damping of tidal species of diurnal and shorter periods during discharge episodes of above $\sim 2000\text{m}^3/\text{s}$, the amplification after impulsive discharge episodes of approximately $\sim 500\text{m}^3/\text{s}$ and the concentration of power inputs found in periods above 8 hours are perhaps the most remarkable features.

Kinematics of tidal wave propagation provides further clues on the dominant processes of the tidal-fluvial interaction. The transit times of high-water (HW), low-water (LW) and upward and

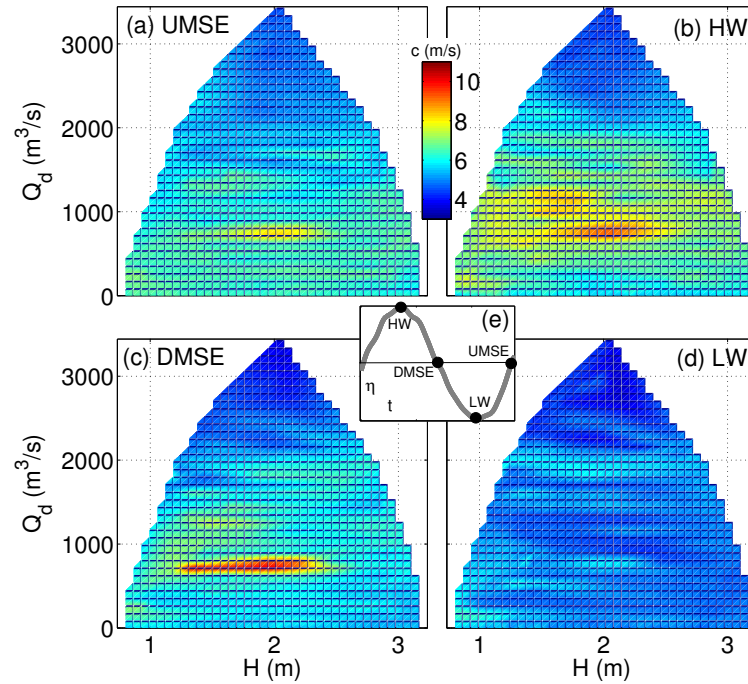


Figure 3.3.3: Low-pass filtered tidal wave celerity, c , as a function of the fresh water discharge, Q_d , and tidal range, H . The observed celerity is determined from propagation lags of the upward zero-crossing through the mean of surface elevation (UMSE, panel (a)), high-water (HW, panel (b)), upward zero-crossing through the mean of surface elevation (DMSE, panel (c)), and low-water (LW, panel (d))). Different tide moments are schematized in panel (e).

downward zero-crossings of elevation (UMSE and DMSE, respectively) are computed between stations β_0 and β_S for the analysis interval shown in Figure 3.3.1, which presents different tidal and river flow conditions. The observed tidal wave celerity c is determined from these propagation lags. Figure 3.3.3 shows the variability of c in terms of fresh water discharges, Q_d , and tidal range, H , at UMSE (panel (a)), HW (panel (b)), DMSE (panel (c)), and LW (panel (d)). Overall, the c pattern remains the same across the different moments of the tide. During periods of low river flow, the observed celerity in spring tides is lower than in neap tides (e.g., at HW $c \approx 5.9$ m/s and 6.2 m/s, respectively) due to the friction dependence on tidal flow. These values are smaller than the classic celerity value for a frictionless, non-convergent estuary, $c = \sqrt{gh_0} \approx 8.2$ m/s with $h_0 = 7$ m, which is taken here as a reference. The largest differences in magnitude are observed between HW (panel (b)) and LW (panel (d)). Tidal wave propagation is faster at HW than at LW. This result is consistent with features of flood-dominated estuaries. For high river flows exceeding 2000 m³/s, no substantial difference is observed between spring and neap tides at the four moments. Above this apparent threshold, high river flows reduce the observed celerities drastically due to damping by the discharge. However, for river flows between the two conditions, from high to very high discharges, the celerity almost doubles the tidal wave celerity under normal conditions (~ 11 m/s), which is most apparent at HW and DMSE for $500 \text{ m}^3/\text{s} < Q_d < 1000 \text{ m}^3/\text{s}$.

Channel convergence, reflection, and friction heavily control the observed celerity values. The convergence length of the GRE, which is a weakly convergent estuary, is not expected to change significantly under different flow conditions, as the estuary is rather channelized. Regarding

the reflection, tidal gauges β_0 and β_S were selected for the wave celerity calculation to minimize reflection effects. They are located far enough from the upstream dam and have the longest records: 17 years of simultaneous measurements under different tidal-fluvial flow conditions. These stations are separated by 80 km, with the last 20 km potentially being affected by the tidal reflection. Nevertheless, wave propagation from β_0 to β_S shows features of a traveling wave such as the linear increase in the tidal phase (Figures 4 and 5 in Díez-Minguito et al. (2012)). Thus, the structure of the patterns shown in Figure 3.3.1 is apparently produced by changes in friction. In particular, the remarkable increase in celerities for $500\text{m}^3/\text{s} < Q_d < 1000\text{m}^3/\text{s}$ is not attributable to effects of the dam on observed celerities but rather to reduced friction induced by high sediment concentrations as will be discussed below.

Further effects of discharges on the tidal currents are shown in Figure 3.3.4. This figure shows tidal ellipse parameters of the semidiurnal tide computed at α_1 from a STHA with $\Delta t = 4T_{M2}$. A STHA with such moving window size can not separate the M2 from the S2, and only the results for the M2 are discussed. Station α_1 is located in a short straight stretch flanked by channel bends with high curvature (see Figure 3.1.1). The time interval shown in Figure 3.3.4 includes long periods under normal conditions and shorter periods under high river flows and transitions between them. Figure 3.3.5 shows two sample vertical profiles of the ellipse parameters (for low, blue curves, and high flows, orange curves) selected from Figure 3.3.4.

Overall, the semi-major axis, S_M , (Figure 3.3.4, panel (b)) decreases smoothly as the depth increases. No sub-surface jump is observed. Spring and neap tide periods are evidenced in the whole water column by alternating warm and cold colors, respectively. These alternations are also noticeable in other tidal ellipse parameters. Under normal conditions, in spring tides around September of 2009, S_M attains 1.50 m/s near the surface. During neap tides, S_M amplitudes occasionally exceed 1 m/s at α_1 . Panel (c) shows the eccentricity, $e = S_m/S_M$. The semi-minor axis, S_m , is typically much lower than S_M ($|e| < 0.05$), as is expected for a rather channelized estuary (Figure 3.1.1). Although the ellipse rotation shows high variability, the anticlockwise rotation appears to prevail near the surface and near the bottom, whereas clockwise rotation (expected for a frictionless system in the northern hemisphere) predominates in the bulk of the water column. The semi-minor axis, S_m , reaches a minimum value of -0.05 m/s at roughly -4 m below the surface (see also selected profiles in Figure 3.3.5, blue curves). As the stratification is normally weak, this behavior may be due to the shearing of lateral flow induced by the channel curvature. Local topographic features such as bends, may have a considerable influence on the tidal ellipse parameters. However, elucidating the precise role of these features has proven difficult from measurements recorded at fixed locations at different cross sections. The inclination of the M2 tidal ellipses varies normally between 0° and 25° at all depths, i.e., along the main channel (Figure 3.3.4, panel (d)). Phases also range from 0 to 90° following spring-neap cycles. The tidal phases are correlated with S_M due to the effects of friction on the momentum balance: the stronger the amplitude, the stronger the damping and the longer the phase. The effects of friction on inertia also explain why the phases decrease with depth, albeit slightly (Figure 3.3.4, panel (e)). Both I and ϕ behave rather uniformly in the water column (also in Figure 3.3.5), meaning that tidal propagation in low river flows can be assumed to be in good approximation as barotropic.

High discharge events modify this configuration and affect the current field or more precisely, the tidal ellipse parameters. The discharge event occurring on 07/Feb/09, with $Q_d \approx 531\text{m}^3/\text{s}$

(Figure 3.3.4, panel (a)) apparently did not dampen the tidal wave at station α_1 . Furthermore, after the discharge follows a remarkable amplification of the semi-major axis amplitude (Figure 3.3.4, panel (b)) that lasts for at least two months, much longer than the discharge itself. This increase is accompanied by a decrease in tidal amplitudes near the bottom (the slope of the profile increases) as is more clearly shown in Figure 3.3.5 (upper left panel, orange curve). Taking observations made during low river flows as a reference, the other tidal parameters, namely S_m , I , and ϕ , are also influenced by the high discharge. The magnitude of the eccentricity near the bottom increases after the discharge at most of the stations, attaining a value of 0.5 (panel (b) in Figure 3.3.4). The difference in eccentricity between the surface and bottom also increases and fluctuates but without a clear pattern. Moreover, the semi-minor axis reverses at the water column. The surface current ellipses acquire a clockwise rotation, whereas the bottom ellipse moves anticlockwise.

The first panel from the left in Figure 3.3.5 more clearly shows the increase (decrease) in S_M in upper (lower) layers of the water column and the change of sign and magnitude of S_m (second panel) after the discharge event. Dynamics observed during low flows are barotropic as indicated by the inclination, I , and phase, ϕ (blue curves in the third and fourth panels), but after the discharge event, the vertical structure of the currents shows a subsurface jump in both I and ϕ from which the location of the pycnocline can be inferred.

Nature of the Oscillatory Motion

The nature of the tidal motion is often simply characterized in terms of the phase lag, ε , between high water and the high-water slack (e.g. Dyer, 1997; Savenije et al., 2008; Díez-Minguito et al., 2012). The phase lag ε is computed here directly from elevation and current time series and not from harmonic analysis. Figure 3.3.6 shows the along-channel variability of ε (panel (b)) in response to high discharge events. Time series of fresh water discharge is depicted in panel (a) as a reference.

The tidal wave reflection at the continental margin induces a standing wave motion at the edge of the inner shelf of the Gulf of Cádiz. The GRE co-oscillates following water level and current changes in the inner shelf because tidal generating forces inside the estuary are negligible. Under the low river flow regime, friction induces an additional phase lag that is close to the theoretical value of $\pi/4$ obtained under the zero-inertia approximation (e.g. Friedrichs and Madsen, 1992). The phase lag decreases further upstream (α_5 , orange curve in Figure 3.3.6) and becomes small at 80 km, which, according to the observational analysis by Díez-Minguito et al. (2012), indicates that in its upper part, tidal propagation is partially standing due to the reflection on the upstream dam. Based on the results of an analytical model that describes tidal wave propagation and its reflection due to a varying cross-section and closed end, Cai, Toffolon, and Savenije (2016) also reported significant reflection at the Alcalá del Río dam. The spring-neap cycle involves fortnightly oscillations in ε due to a change in bottom shear stress. At spring tides, ε tends toward $\pi/4$ regardless of the stretch (blue and orange curves in panel b). At neap tides, shear stress is lower, and in the upper part of the estuary, where the influence of reflection is strong, ε tends toward 0 whereas in the lower part, ε moves toward $\pi/2$, separating from $\pi/4$.

After a high discharge event, an increase of roughly 0.5 m in the tidal range, H , is observed both for neap and spring tides at both stations (Figure 3.3.6, panel (c)). The 07/Feb/09 discharge

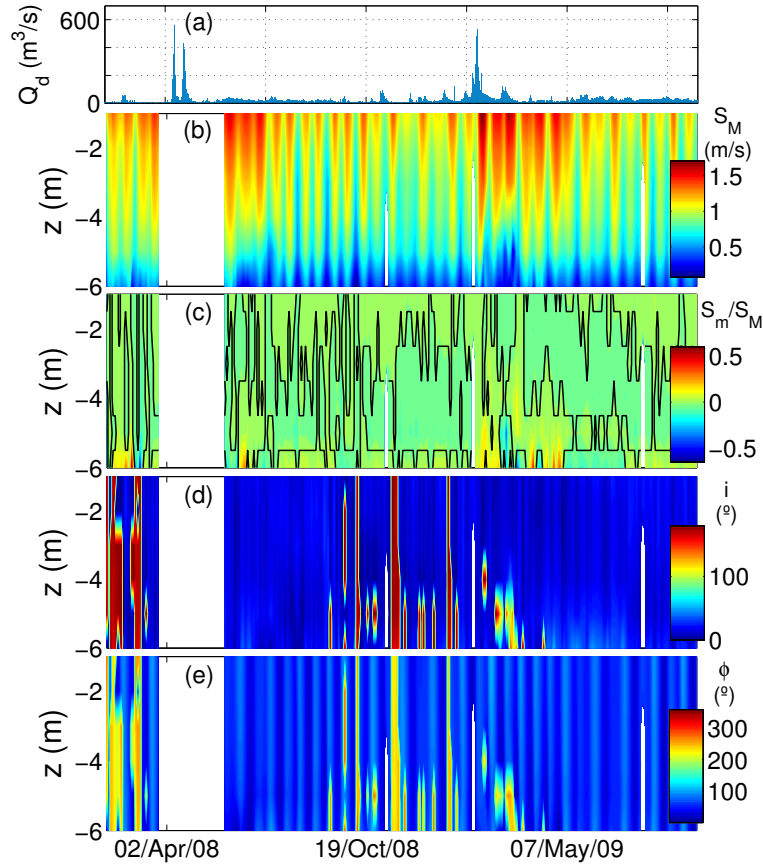


Figure 3.3.4: Color plots of the tidal ellipse parameters at α_1 for the M2 as a function of vertical coordinate z and time. Panel (a): Time series of fresh water discharge from the upstream dam. Panel (b): semi-major axis S_M . Panel (c): eccentricity defined as the ratio between the semi-minor axis S_m , and semi-major axis S_M , i.e., $e = S_m/S_M$. The black line in the eccentricity plot, which is shown for purposes of clarity, separates positive and negative values. Panel (d): inclination I . Panel (e): tidal phase ϕ .

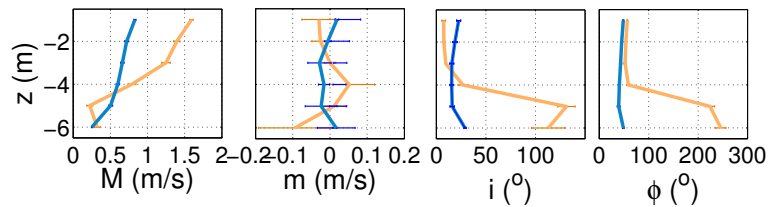


Figure 3.3.5: Selected tidal ellipse parameter profiles for the M2 at spring tide under normal conditions (blue lines, 14/Dec/08) and after a fresh water discharge event of $Q_d \approx 531 \text{m}^3/\text{s}$ (orange lines, 13/Mar/09). From left to right: semi-major axis S_M , semi-minor axis S_m , inclination I , and phase ϕ .

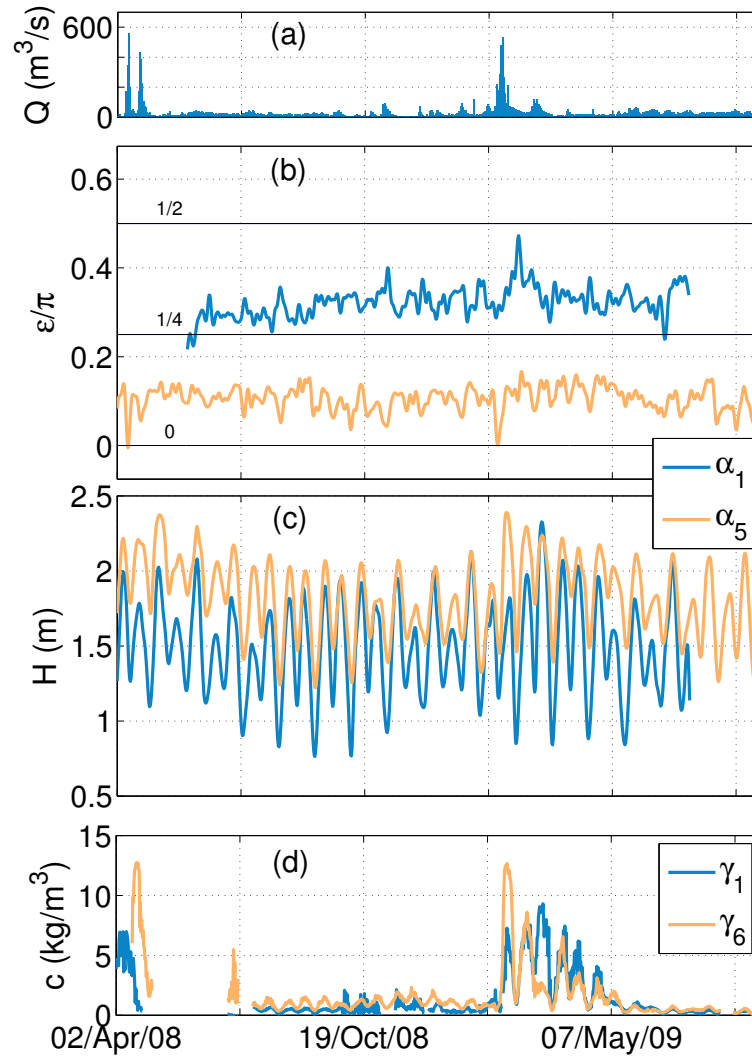


Figure 3.3.6: Low-pass filtered phase lag ε between HW and HWS. Panel (a): Time series of fresh water discharge from Alcalá del Río. Panel (b): ε at α_1 (blue curve) and α_5 (orange curve). Panel (c): tidal range H at stations interpolated from the nearest stations β_k of the tidal gauges set. Panel (d): Time series of tidally averaged suspended sediment concentrations, c , at stations γ_1 and γ_6 .

event ($\sim 531\text{m}^3/\text{s}$) was not significant enough to move ε to $\pi/4$, even during the peak. The tidal motion at α_1 in the lower part of the estuary shows a more progressive behavior, i.e., $\varepsilon \approx \pi/2$, as if the effects of shear stress were inhibited (blue curve, central panel Figure 3.3.6). Notably, the shift in ε occurs two weeks after the discharge event. By contrast, upstream at α_5 , the standing character of the tidal motion is more pronounced and is produced without an apparent time delay with respect to the discharge event. The post-discharge adjustment of ε to return to former levels took 60 days, which is similar to the recovery time of turbidity and S_M (Figure 3.3.6, panel d).

Flow-sediment Feedback

The regime shift in tidal water levels and currents, and in S_M , S_m , H , and ε , in particular, after February of 2009 discharge event (Figure 3.3.4-3.3.6), may be due to an increase in (salinity)

stratification because the water column gains stability from fresh water inputs, increasing density stratification and yielding lower effective friction (Giese and Jay, 1989; Winterwerp, Lely, and He, 2009). Nevertheless, salt intrusion X_2 , in the estuary recovers to values recorded before the discharge event within the first two weeks after the discharge event (Figure 3.3.7, panel b) (Díez-Minguito et al., 2013), but the regime shift lasts longer (e.g., Figure 3.3.4, panel b). This shift from normal conditions is not induced by a tidal wave blocked by enhanced river currents (e.g. (Peregrine, 1976; Chawla and Kirby, 2002)), a phenomenon that is fairly common in wave-tide interactions, as tidal wavelengths are large and river currents are low enough.

The amplification in both S_M and H is apparently caused by a suppression of turbulence due to stratification induced by extreme suspended sediment concentrations (Gust and Walger, 1976; Geyer, 1993; Winterwerp, Lely, and He, 2009). These concentrations, which are triggered by the high discharge event, are several orders of magnitude higher than those recorded under normal conditions in almost the entire estuary (Figure 3.3.6, panel d). This effect was already reported in other turbid estuaries (see e.g. King and Wolanski, 1996; Kineke et al., 1996; Alvarez et al., 1999) and noted by Wang, Winterwerp, and He (2014) in the GRE. This increase in stratification restricts the frictional influence below the pycnocline, which explains the intensification of the progressive (standing) character of the tidal motion in the upper (lower) part of the estuary, the damping of S_M near the bed and the sign inversion in S_m . This modification of the tidal ellipse parameters by stratification was identified by Souza and Simpson (1996) for the region of the North Sea influenced by Rhine discharge.

Stratification is evidenced by the bulk Richardson number, Ri , which compares the buoyant energy per unit of volume with that induced by tidal action. The bulk Richardson number is computed here, at the same time scale as the tidal parameters, as following:

$$Ri = gh\Delta\rho/(\rho(0)S_M^2) \quad (3.4)$$

where $\Delta\rho = \rho(-h) - \rho(0)$ is the density difference between the bottom and surface. The values of $\rho(-h)$ and $\rho(0)$, which are extrapolated from available data, are computed both with and without considering the presence of sediments (Ri^w and Ri^{wo} , respectively) to separately evaluate the role of suspended sediment and salinity in water column stability. The bulk Richardson number Ri^{wo} is computed using $\rho(S, T, p) = \rho_{sw}$, whereas Ri^w is determined using the full equation $\rho(S, T, p, c) = \rho_{sw} + c(1 - \rho_{sw}/\rho_c)$. Figure 3.3.7, panel (c), shows remarkable differences between Ri^{wo} and Ri^w at all stations over the time period. Station α_0 (black vertical lines), which is located in the lowest stretch of the estuary and downstream from the tidally averaged salt intrusion point X_2 (Figure 3.3.7, panel b), exhibits the larger Richardson numbers computed with ($Ri^w \approx 3.8$, upper black dots) and without ($Ri^{wo} \approx 2.5$, lower black dots) sediments. These values are one order of magnitude larger than those observed before the high discharge event. Both values tend to decrease upstream. Stations upstream from the salt intrusion point (e.g., at α_5) apparently show small values of Ri^{wo} , which indicates that the water column has a largely uniform salinity profile. However, the larger values of Ri^w at the same stations indicate that stratification is mainly induced by high suspended sediment concentrations, which inhibit the transfer of vertical momentum, decoupling the overlying flow from the bottom. This effectively reduces friction favoring an increase in tidal amplitudes, as is shown in Figures 3.3.4 and 3.3.5. Stations α_2 and α_5 show the largest differences between both Richardson values (e.g., at α_5

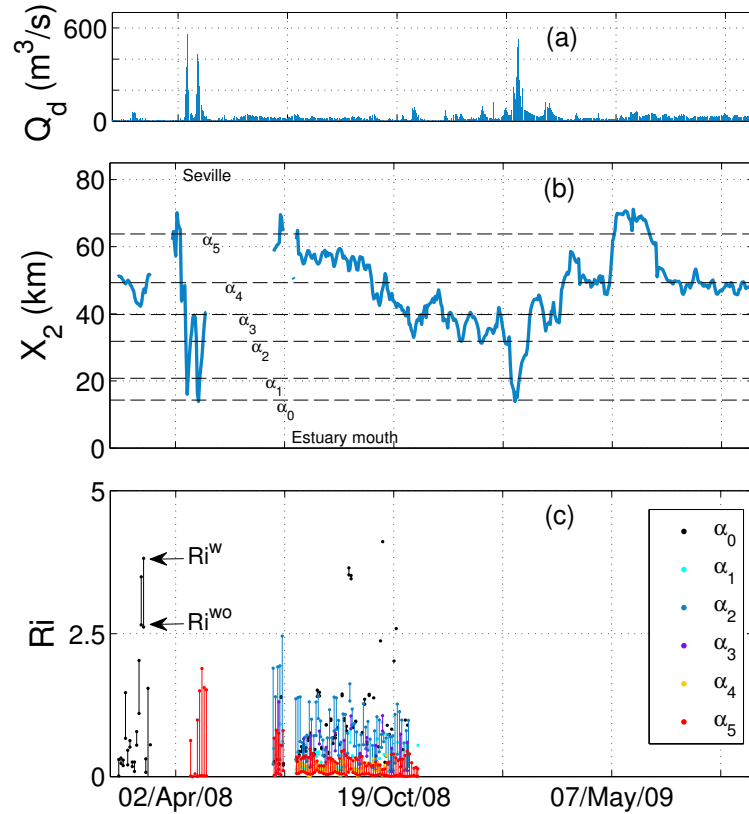


Figure 3.3.7: Panel (a): Time series of fresh water discharge from the upstream dam. Panel (b): Time variability of the 2 psu isohaline salt intrusion (blue curve). Along-channel positions where current meters α_k are located (dashed black lines). Panel (c): bulk Richardson number computed at α_k locations. Vertical lines show the span of the bulk Richardson number with, Ri^w , and without, Ri^{wo} , considering a sediment laden water column.

$Ri^{wo} \approx 0$ and $Ri^w \approx 2$ after the Apr/08 high discharge event).

The inner structure of the water column and the height of the frictional layer in particular are denoted by the vertical shear of horizontal currents, $G_H = [(\partial \bar{u} / \partial z)^2 + (\partial \bar{v} / \partial z)^2]^{1/2}$, and vertical currents, $G_V = [(\partial \bar{w} / \partial z)^2]^{1/2}$. Figure 3.3.8 shows G_H and G_V in panels (b) and (c), respectively. Discharge triggers higher values of G_H and G_V near the bottom due to an increase in sediment concentrations. This increase is produced approximately two weeks after the discharge event, suggesting that the highest stratification level at this station is attained at this time, as is shown in Figure 3.3.6, panel (d) (station γ_1 , close to α_1). The two-week lag coincides with that computed in ε for the same station. The upper layer streams more freely over a bottom layer (below $z \approx -3$ m) where frictional effects are confined.

3.3.2 Remarks

This observational study investigates non-linear interactions between tides and river discharge along several stretches of the Guadalquivir River Estuary, which is a highly turbid estuary in SW Spain. The study specifically focuses on the non-stationary response of water levels and currents to high discharge events, the evaluation of the main contributing non-linear terms to the

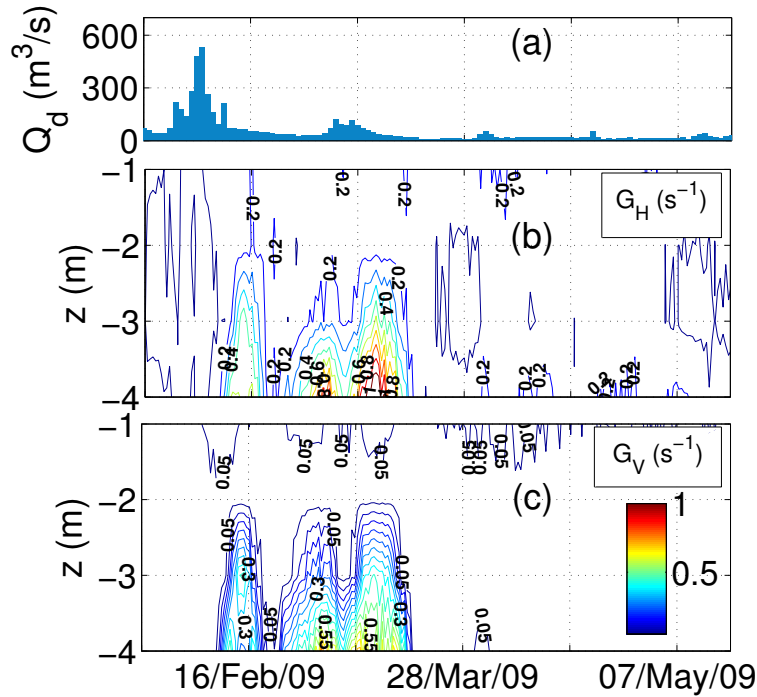


Figure 3.3.8: Panel (a): Time series of fresh water discharge from the upstream dam. Panels (b) and (c): shear of the horizontal, G_H , and vertical current, G_V , respectively, at α_1 . The latter two panels share the same colorbar scale.

generation of overtides and compound tides, which is completed as a function of time to capture the variability induced by the river discharge, and the term-by-term estimate of the balance equations at a subtidal scale for pre-discharge, discharge, and post-discharge periods.

Field data shows that the estuary responses to high discharges are dependent on sizes and distributions, among other factors such as tidal conditions or previous discharge events. Extreme discharge events that last more than 2 weeks with peaks above $2000\text{m}^3/\text{s}$ dampen tidal species of the diurnal period or of shorter periods and reduce tidal wave propagation velocity. Most energy generated within the estuary occurs at fortnightly and higher frequencies. However, high to very fresh water discharges of between $\sim 500\text{m}^3/\text{s}$ and $\sim 1000\text{m}^3/\text{s}$ may induce a regime shift due to high suspended sediment concentrations that discharge triggers. High sediment concentrations that reach several orders of magnitude higher than those under normal conditions and that last over two months (much longer than the discharge period itself) increase stratification in the water column.

The change in the structure of the water column affects on the kinematics and dynamics of along-channel tidal wave propagation. Possibly with the exception of locations near the head dam, such discharge events significantly increase the observed tidal wave celerity, which doubles its value under normal conditions. The increase in stratification restricts frictional influence to the bottom layer and partially decouples the overlying flow from the bottom, as evidenced by the regime shift in water levels, tidal ellipse parameters, and current shearing.

The results presented in this Section, and in particular the identification of the physical

mechanisms that control tidal-fluvial interactions, are necessary for developing reliable models that can help improve the navigational conditions of the channel and that assess flood risks in the Guadalquivir River Estuary, as done in Section 4.3.

3.4 Effects of a dredging intervention in the Guadalquivir estuary

This section assesses the possible morphodynamic effects of deepening the navigation channel in the Guadalquivir estuary. In Chapter 4 these effects are quantified through modeling and simulation techniques. The present section mainly focuses on the estuarine processes.

3.4.1 Tidal amplification

Deepening the estuarine tidal channels often leads to tidal amplification and deformation of the tidal wave (Wang et al., 2002; Winterwerp and Wang, 2013; Maren, Winterwerp, and Vroom, 2015), amongst other factors (Ensing, Swart, and Schuttelaars, 2015). The tidal motion is, at a large extent, determined by the competence between the friction and the channel convergence (Savenije and Veling, 2005). In the Guadalquivir, the current navigation channel design arose from the occupation of the river banks and the dredging interventions that took place in the second half of the past century, amongst other factors. Besides the increase in the water depth all along the estuary, an increase in the tidal range was recorded along the main channel (Wang, Winterwerp, and He, 2014). This was more noticeable in the upper stretch (from Seville to the Alcalá del Río dam), where the wave reflection at the head play an important role in the tidal propagation (Prandle and Rahman, 1980; Díez-Minguito et al., 2012). Figure 3.4.1 shows the tidal range at β_S for the past twenty years, where a positive trend is observed, in agreement with other studies (Wang, Winterwerp, and He, 2014).

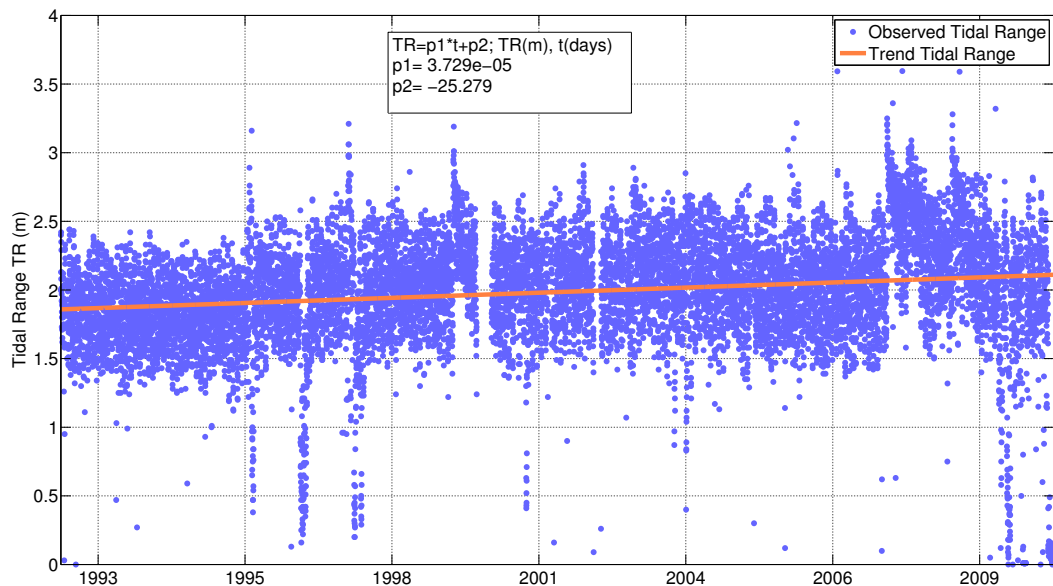


Figure 3.4.1: Observed Tidal range and tendency at β_S station in the lock of the Port of Seville. It should be noticed that time is in Julian days.

In contrast to other highly human-altered estuaries, despite the maintenance dredging in the Guadalquivir, there are no morphodynamic records after deepening the navigation channel, since at present this intervention has not occurred. However, i) the analysis of the data from the monitoring network deployed between 2008–2011, ii) previous and present studies in the Guadalquivir, as well as iii) the acquired knowledge from hydrodynamically similar estuaries; provide adequate insight to evaluate the effects of deepening the navigation channels (Maren et al., 2015). The main involved processes are sketched in Figure 3.4.2, which shows the feedback loop between these and the tidal amplification as a response to deepening the navigation channel. This loop can be summarized as followed (Winterwerp and Wang, 2013): deepening often leads to tidal amplification, increasing the import of suspended matter concentration (SPM) which, in

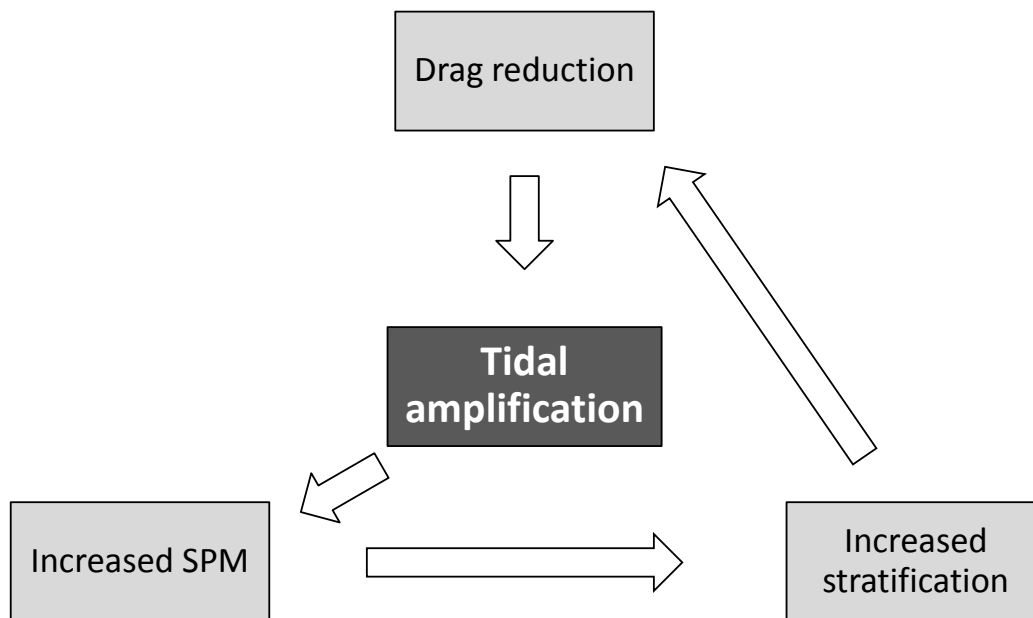


Figure 3.4.2: Conceptual sketch showing the feedback loop between different estuarine processes as a consequence of channel deepening, where SPM is the suspended matter concentration.

3.4.2 Increased suspended matter concentrations

The alteration of the vertical and the horizontal tide as a consequence of deepening of tidal channels usually results in significant increases in suspended matter concentrations (SPM), in particular in the estuarine turbidity maximum (ETM). For instance, Jonge et al. (2014) document these changes for the past 50 years in the Ems estuary. The authors observed that the shift of the ETM into the freshwater region resulted from a cumulative effect of the deepening, plus the subsequently changes in the vertical viscosity and the partial slip parameter (bed roughness). In their case, the SPM concentration increased significantly in the tidal river, originating a strong decrease of the vertical mixing. The distribution of SPM varies according to tides and other factors like wind-induced resuspension (De Jonge, 1995) and river discharge (Jalón-Rojas et al., 2016). Maren, Winterwerp, and Vroom (2015) found, for the Ems estuary too, that the import

of fine sediment increased because of larger tidal transport, even though the degree of tidal asymmetry may not have significantly changed after the interventions. These works reached similar conclusions: the rise in SPM concentrations reduced the hydraulic drag, amplifying the tidal range. Hence, the export of fine sediment became less because the river-induced residual flow velocity decreased with deepening of the channel.

Up-estuary transport of sediments is also related to salinity-induced density currents (Meade, 1969; Uncles, Elliott, and Weston, 1985). The magnitude of the residual flow velocity u can be assessed with Equation 3.2, which is proportional to water depth. Assuming at this stage the eddy viscosity to be constant, increasing the water depth leads to strengthening the residual current. In very few (if any) estuaries worldwide, observational evidence exists for the impact of deepening on estuarine circulation, since the residual flow velocity is very sensitive to the observational techniques (Maren et al., 2015). However, process-based numerical modeling was used in Maren et al. (2015) for the Ems estuary, where the authors showed that the magnitude of the estuarine circulation increased as a result of deepening. This caused an up-estuary increase in the SPM, agreeing with the reasoning mentioned above from the analytical formulation.

As explained in Section 3.3, high sediment concentrations triggered by certain high discharge events in the Guadalquivir induce 60 day post discharge amplification of tidal current and elevation amplitudes. Hence, it is likely that this flow-sediment feedback would also occur after a deepening, where higher SPM would lead to higher tidal currents and vice versa. This effect is more related to stratification phenomenon, as explained below.

3.4.3 Increased stratification

The increase of the water column stratification is commonly assessed with the (bulk) Richardson number (R_i , Equation 3.4), which indicates the ratio between the turbulence damping (stratification) and the turbulence production (velocity shear). Following the literature, this quantity is related to another relevant parameter, such as the eddy viscosity, N_z (Dyer, 1997):

$$N_z = N_0 (1 + 10R_i)^{-1/2} \quad (3.5)$$

where N_0 is the eddy viscosity value in the absence of stratification. Bowden, Fairbairn, and Hughes (1959) related N_0 to the tidal current amplitude U and the water depth h with $N_0 = c_v U h$, where c_v is a calibration parameter that usually takes values in order of $\sim 10^{-3}$. Combining both, Equation 3.5 can be rewritten as,

$$N_z = (c_v U h) \cdot (1 + 10R_i)^{-1/2} \quad (3.6)$$

Equation 3.6 points that the eddy viscosity coefficient is not constant after a dredging intervention. On the one hand, under well-mixed conditions an increase in the tidal current amplitude would increase the mixing. On the other hand, the mixing is reduced when water column is more stratified. These mechanisms are interrelated, being subjected the bed morphology, the duration and specific timing of the dredging intervention, and the SPM concentrations (Jonge et al., 2014). However, the feedback loop between tidal amplification and reduction in hydraulic drag (Figure 3.4.2) is mostly due to the vertical stratification induced by high SPM concentrations (Winterwerp and Wang, 2013).

Higher stratification induced by higher SPM concentrations is observed for the Guadalquivir estuary. In Section 3.3.1 the bulk Richardson was computed with and without considering the suspended sediments. After a high discharge event, the increase in the stratification was mainly induced by high SPM, reducing the friction and favoring the tidal amplification. Thus, the impact of high discharge events in the Guadalquivir estuary can be regarded, up to some extent, as those derived from a channel deepening. This fact justifies the analysis of the tidal-fluvial interaction in Section 3.3, and the assessment of different management scenarios in Chapter 4 where the freshwater discharge plays an important role.

The relation between the freshwater discharge Q_d , and the stratification Ri , is characterized by a least-squares linear regression, namely $Ri = l_1 Q_d + l_2$. The coefficients l_1 and l_2 are respectively $l_1 = 0.0045 \text{ s/m}^3$ and $l_2 = 0.2753$, and the determination coefficient is $R^2 = 0.49$. Although residuals are not small, this simple fit relates the increase in system buoyancy with inputs of fresh water and suspended sediment by fluvial discharge. Note as well that even with $Q_d = 0$, there is a measurable sediment concentration in the water column that contributes to the density stratification (non-zero Ri). This stratification reduces the effective drag c_D , as detailed below.

3.4.4 Drag reduction

An increase in the stratification reduces the effective drag c_D , thus amplifying the tidal range and the tidal currents. This drag reduction can be further explored and related to other coefficients, such as the Chezy coefficient C , via the relationship (Soulsby, 1997)

$$c_D = \frac{g}{C^2} \quad (3.7)$$

This C coefficient can be considered dependent on the structure of the water column (Winterwerp, Lely, and He, 2009), that changes on time t .

$$C(t) = C_0 + 4hg^{1/2}BRi(t) \quad (3.8)$$

where C_0 is the Chezy value for sediment-free conditions and B the Rouse number. This Rouse number depends on the shear velocity, and thus to drag coefficient again. Fixing this ratio as a constant after a dredging intervention, and combining Equations 3.7 and 3.8, yields:

$$c_D = \frac{g}{C_0 + 4hg^{1/2}BRi(t)} \quad (3.9)$$

In the case of the Guadalquivir $B \approx 0.3$ (Ruiz and Losada, 2010). C_0 can be determined from the Manning coefficient $n = 0.018 \text{ s/m}^{1/3}$, which was obtained by García-Contreras (2009) for the Guadalquivir matching tidal currents and elevations with observations ($C_0 = h_0^{1/6}/n = 76.8 \text{ m}^{1/2}/\text{s}$). These values, combined with Equation 3.9 provide physical insight and enable a simple quantification of the effective drag reduction.

3.4.5 Remarks

Based on field data, the possible morphodynamic effects of deepening the navigation channel in the Guadalquivir estuary were described, according to the common feedback loop: tidal amplification, increase in the SPM, increase in the stratification and drag reduction. For the Guadalquivir, most of the presented reasoning was based on the effects of high discharge events, where the increase in the SPM increased the stratification in the water column, reducing the friction, then amplifying tidal current and elevation amplitudes. But this comparison should be used with caution, since not all high freshwater discharges have similar consequences, as presented in Section 3.3 and other works (Wang, Winterwerp, and He, 2014).

3.5 Results & Conclusions

Field data measurements from a comprehensive monitoring campaign were used to describe different processes in the Guadalquivir. Regarding the salt transport structure, during low flow regime where the river discharge is lower than $40 \text{ m}^3/\text{s}$, the estuary falls in class Type-2a according to Hansen and Rattray (1966) diagram. This allocation indicates that the estuary is well mixed under normal conditions. During high flow regime, with values above $400 \text{ m}^3/\text{s}$, the estuary moves to 2b and 3b regions, suggesting stronger gravitational circulation, particularly in the mouth. The gravitational circulation was analyzed under normal conditions. Values for the eddy viscosity coefficients ranging from 10^{-4} to $10^{-2} \text{ m}^2/\text{s}$ were obtained. The (mean) effective vertical turbulent viscosity N_z , decreases from $1.2 \times 10^{-3} \text{ m}^2/\text{s}$ near the mouth to $3.3 \times 10^{-4} \text{ m}^2/\text{s}$ in the middle of the estuary due to the decrease in the shear stress, and the longitudinal density gradient. Power-law relationships were obtained to assess the relative influence of the tidal current amplitude and river flow on the saline intrusion. For low flow regime, the saline intrusion depends more on the mean tidal fluctuations, and to a lesser extent on the river discharge. Tidal-pumping, lateral stirring, and baroclinic circulation seem to be the main mechanisms that control the salt transport. During the fluviially-dominated regime, the dependence of the salt intrusion on the freshwater flow and the gravitational circulation greatly increase, in agreement with the abovementioned classification. The role of tides also increases after peak discharges, due to the mud entrainment induced by turbulence.

Field data shows a 60-day post-discharge amplification of tidal current and elevation amplitudes and a clockwise rotation of the tidal ellipse in upper layers. A decrease of amplitudes and an anticlockwise rotation predominates near the bed. Extreme discharge events that last more than two weeks with peaks above $2000 \text{ m}^3/\text{s}$ dampen tidal species of the diurnal period or of shorter periods and reduce tidal wave propagation velocity. Most energy generated within the estuary occurs at fortnightly and higher frequencies. However, high to very fresh water discharges of between $\sim 500 \text{ m}^3/\text{s}$ and $\sim 1000 \text{ m}^3/\text{s}$ may induce a regime shift due to high suspended sediment concentrations that discharge triggers. High sediment concentrations that reach several orders of magnitude higher than those under normal conditions and that last over two months (much longer than the discharge period itself) increase stratification in the water column. The change in the structure of the water column affects the kinematics and dynamics of along-channel tidal wave propagation. Possibly except locations near the head dam, such discharge events significantly increase the observed tidal wave celerity, which almost doubles its value under normal conditions, from $\sim 6 \text{ m/s}$ to $\sim 11 \text{ m/s}$. The increase in stratification restricts frictional influence to the bottom layer and partially decouples the overlying flow from the bottom, as

evidenced by the regime shift in water levels, tidal ellipse parameters, and current shearing. The description of these processes improves the understanding of the feed-back loop that may occur in the Guadalquivir as a response to deepening the navigation channel: how the tidal amplification would increase the sediment matter concentration, thus increasing the stratification, implying a drag reducing that would enhance, in turn, the tidal signal.

3.A Data Collection

The analyzed data were mainly recorded over a three-year field campaign (2008-2011). Detailed descriptions of the equipment and of the campaign's general aims can be found in (Navarro et al., 2011) and (Ruiz et al., 2015), respectively. Here, only a brief description of the instrumentation related to this study is provided.

Sea level, current, and water quality data were recorded at several stations along the main estuary channel (see Fig. 3.1.1). Current data were recorded every 15 min by Acoustic Doppler Current Profilers mounted rigidly in surface buoys close to the *thalweg*. They are denoted by $\alpha_0 \dots \alpha_6$ in Fig. 3.1.1, Table 3.A.1. The water column was sampled in cells of 1 m in height. The data were post-processed to remove measurements when the tilt sensor listed a value of greater than ~ 20 degrees in either pitch or roll (Navarro et al., 2011). Tidal gauges were moored at the margins and provided water levels every 10 min. They are defined in Fig. 3.1.1 as $\beta_1 \dots \beta_6$, see Table 3.A.2. The tidal gauges β_0 and β_S , separated by 80 km (Fig. 3.1.1), are the property of the Puertos del Estado government agency (State-owned Spanish Port, Ministry of Public Works) and are located in the Port of Bonanza at the estuary mouth and in the inland Port of Seville, respectively. These gauges recorded the water level every hour since 1992. The gauge β_S was moved 2 km downstream after the completion of a new lock in January of 2011. Only data for before January of 2011 are used in this study. Gaps in the water level series were filled in using T_TIDE, a standard harmonic analysis toolbox for MatlabTM (Pawlowicz, Beardsley, and Lentz, 2002).

Eight environmental quality stations denoted as γ_k in Fig. 3.1.1, Table 3.A.3, measured temperature, turbidity, and conductivity among other variables every 30 min (15 min for certain intervals) at $z = -1$ m below the water surface ($z = 0$ m). Over the first nine months, measurements were also recorded at -2 , -3 , and -4 m below the water surface. Station γ_0 at the estuary mouth was selected as the origin of the x coordinate (positive landward along the channel). The standard salt intrusion limit, X_2 , is defined as the distance from γ_0 to the 2 psu isohaline and is evaluated from the tidally averaged longitudinal distribution of salinity, which is approximated to a tanh function as $S = 0.5S_0(1 + \tanh(\xi_0 + x/\xi_1))$ (Warner, Geyer, and Lerczak, 2005; Talke, Swart, and Schuttelaars, 2009), where $S_0 = 36$ psu and S values are determined from observations made at each γ_k . The tanh distribution is fit to observations of each tidal cycle by determining best fit values of parameters ξ_1 and ξ_2 . The suspended sediment concentration, c , is estimated in kg/m^3 from turbidity data recorded in formazine nefelometric units (fnu) (Navarro et al., 2011; Díez-Minguito et al., 2014). From these data, the fluid density $\rho(S, T, p, c)$ (sea water and suspended sediment mixture) is calculated from the sea water density $\rho_{sw}(S, T, p)$ at the γ_k stations as $\rho = \rho_{sw} + (1 - \rho_{sw}/\rho_s)c$, where $\rho_s = 2650 \text{ kg/m}^3$ is the sediment density. Although the vertical structure of density can be more complex, estimates of density in the whole water column $\rho(z)$ are extrapolated by fitting the density data at different depths to a theoretical exponential law (Talke, Swart, and Schuttelaars, 2009; Friedrichs, Armbrust, and De Swart, 1998), namely,

$\rho(z) = \rho(-h)\exp(-d(z+h))$, where z is the vertical coordinate positive upwards ($z = 0$ at the surface), h is the water depth, and d is a decay coefficient that accounts for the degree of vertical mixing.

Daily fresh water discharge records for the Alcalá del Río dam, which releases approximately 80% of the total fresh water input into the estuary, were obtained from the Agencia Andaluza del Agua (Regional Water Management Agency). Wind direction and magnitude were measured with a sampling period of 10 min by a meteorological station (M.S.).

Table 3.A.1: Along-channel positions where the current-meters α_i are located.

Current-meter	α_0	α_1	α_2	α_3	α_4	α_5
km	14.30	20.80	31.80	39.80	49.30	63.80

Table 3.A.2: Locations of the tidal gauges β_i .

Tidal gauge	β_0	β_1	β_2	β_3	β_4
km	5.30	21.55	26.80	36.45	51.80
Tidal gauge	β_5	β_6	β_7	β_8	β_9
km	62.55	76.00	93.73	99.97	108.5

Table 3.A.3: Locations where the CTDs (γ_i) are located, with respect to the estuary mouth.

CTD	γ_0	γ_1	γ_2	γ_3
km	0	17.30	23.60	26.20
CTD	γ_4	γ_5	γ_6	γ_7
km	35.30	47.10	57.60	84.30

3.B Time Series Analysis Methods

For data analysis, the assessment of non-stationary behaviors resulting from tidal-fluvial interactions in the GRE is mainly performed via harmonic and wavelet analyses and through the low-pass filtering of time series. The focus is on the M2 and S2 ($T_{S2} = 12.00$ h) semidiurnal tides, overtide M4 ($T_{M4} = 6.21$ h) and compound tide MSf ($T_{MSf} = 14.76$ days).

A standard Short-Term Harmonic Analysis (STHA) (see e.g. Godin, 1999; Gallo and Vinzon, 2005; Guo et al., 2015) of currents and elevations is performed with current meters and tidal gauge data. Time series of tidal elevation amplitudes and phases of the resolved constituents are obtained at β_k using T_TIDE. Similarly, the temporal evolution at six different depths (from -1 m to -6 m) of the four tidal ellipse parameters (the semi-major axis, S_M , semi-minor axis, S_m , inclination with respect to W-E direction, I , and the phase of the tidal current relative to Greenwich, ϕ) is obtained at α_k locations. A moving window of sizes $\Delta t = 4 T_{M2}$ and $\Delta t = 29 T_{M2}$ with $T_{M2} = 12.42$ h is employed for both elevations, η , and currents, u . This windowing approach is appropriate for extracting physical information on (time-)scales of variability of η and u , although it limits the number of constituents (frequencies) that can be resolved (e.g., the STHA

with the largest window size $\Delta t = 29 T_{M2}$ separates the M2 from the S2 constituent, but the STHA with $\Delta t = 4 T_{M2}$ can not separate the M2 from the S2).

The STHA and wavelet analysis complement one another. Both are applied to the time series of elevations and currents to analyze non-stationary behavior at different frequencies. Wavelet analysis is a common tool for analyzing localized variations of power within a time series. A wavelet transform extracts the frequency content of a signal as a function of time, such that the trade-off between time and frequency resolution is nearly optimal with respect to the Heisenberg uncertainty principle (Rioul and Vetterli, 1991). By decomposing a time series into time–frequency space, one can determine both the dominant modes of variability and how those modes vary in time. (Torrence and Compo, 1998).

The Continuous Wavelet Transform (CWT) method, devised to conserve the total energy under the transform, is more accurate and efficient than the STHA at optimizing the time-frequency resolution and in allowing for the identification of nontidal variations in signals (see e.g. Jay and Flinchem, 1997; Flinchem and Jay, 2000; Buschman et al., 2009; Guo et al., 2015; Hoitink and Jay, 2016). The CWT is a time variable analog to the Fourier transform that uses evenly spaced frequencies. The CWT transforms time series into two-dimensional arrays in time and frequency, resolving both frequency modes and variations of these modes over time (Torrence and Compo, 1998). However, the CWT method provides amplitudes of tidal species rather than individual tidal constituents. The wavelet power of the different tidal species can be influenced by major constituents in a given species to varying degrees depending on the frequency resolution and wavelet length. In this work, the cross wavelet and wavelet coherence toolbox for Matlab™ by Grinsted, Moore, and Jevrejeva (2004) is used. A Morlet-type wavelet function is selected. This wavelet function is commonly used due to its optimal properties for tides (e.g. Sassi and Hoitink, 2013; Guo et al., 2015). The nondimensional frequency scale is set to 6. This value offers a good balance between time and frequency resolutions for tidal time series (Grinsted, Moore, and Jevrejeva, 2004). The frequency resolution of the Morlet function is set to 1/20, which is adequate for generating smooth enough results. The largest number of scales considered is 32.

Time series are low-pass filtered to remove tidal oscillations (diurnal and higher) using a zero-phase, fourth order Butterworth digital filter.

SIMULATION OF MANAGEMENT SCENARIOS IN THE GUADALQUIVIR ESTUARY. DEEPENING IMPLICATIONS

Since estuaries and human communities are in permanent feedback, the ability to model and predict both the natural and the stressed response to forcing agents, and their spatio-temporal shift, is an issue under permanent study. Natural variability of the systems, oceanographic and atmospheric events, high river discharges, saline intrusion, spills and dredging interventions, really concern managers and societies inhabiting these areas. The present Chapter models the main processes and predicts the effects of significant management scenarios for the Guadalquivir estuary. The scenarios correspond to a decrease in the freshwater discharge input for next decades and the deepening of the navigation channel.

Two major forcings are considered for the simulations: tidal motion and freshwater discharge. In the latter case, Section 4.1 applies a non-stationary statistical approach to representing its stochastic nature. The variables analyzed within the scenarios are the saline intrusion and the subtidal currents and levels. Regarding the saline intrusion, Section 4.2 presents a heuristic model to predict on a medium-term basis the scenarios, including the influence of wind. This is achieved by means of Markov Chain Monte Carlo simulations. Predictions of subtidal water levels and currents are performed with common regression models using the method of Monte Carlo, as presented in Section 4.3. Short-term analysis for subtidal elevations is also done in that Section.

4.1 River discharge: Non-stationary modeling

The objective of this characterization is to obtain the marginal distribution that represents the best the forcings behavior, used to simulate a long time series of such variable. In our case study, the variable is the river discharge in the Guadalquivir estuary, with noticeable seasonality (Section 3.1). After the stationary analysis (Section 4.1.1), the non-stationary approach developed in Solari and Losada (2011) is applied (Section 4.1.2).

4.1.1 Stationary modeling

Usual and mixture models (Appendix 4.A) for the marginal distribution of the river discharge are implemented. Usual distributions are the exponential (EX), Lognormal (LN), Weibull (WB) and Gamma (GM). The mixture models are intended to incorporate the central and extreme populations into a single model. In these, the central regime is a truncated distribution, where the upper and lower tails are represented by means of Generalized Pareto distribution (GPD). The analyzed resulting distributions are the LN-GPD and the WB-GPD (Solari, 2011). The parameters of the mixture models are estimated by maximum likelihood. Kolmogorov-Smirnov test, with 5% significance level, assesses the goodness of fit. To avoid numerical inconsistencies with null discharge (4% of the data), and considering the precision of the measurements (10^{-2}), the time series is uniformly completed with values between $5 \cdot 10^{-3}$ and $1 \cdot 10^{-2} \text{ m}^3/\text{s}$.

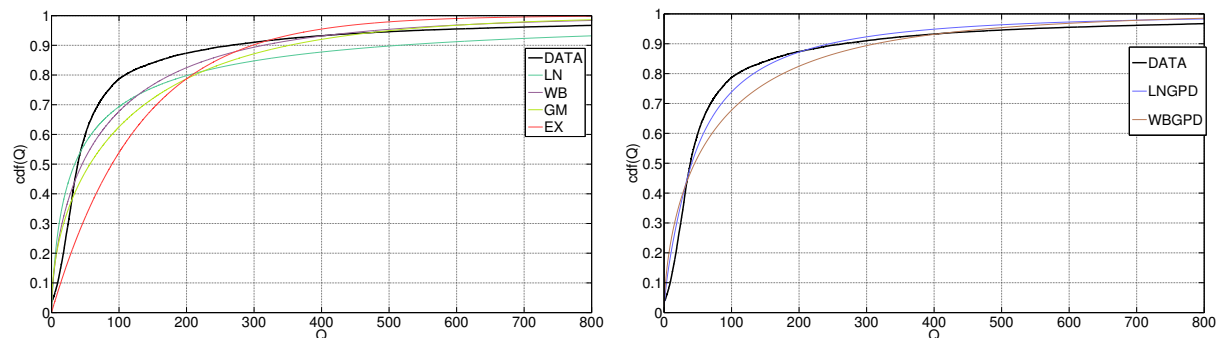


Figure 4.1.1: Cdf for the river discharge with the usual models (left panel) and the mixture models (right panel) described in Section 4.1.1.

Figure 4.1.1 (left panel) shows the empirical, as well as the modeled cumulative distribution function (cdf) of the river discharge. According to the test, the best fit corresponds to LN distribution. Figure 4.1.1 (right panel) shows the cdf of LN-GPD and WB-GPD. The best distribution is the LN-GPD. Comparing the best usual and mixture distributions, the LN and LN-GPD, the later one improves the fit, especially in the tails. Nevertheless, none of them can capture the trend with low freshwater discharges. The poor fit with usual models and the strong seasonality observed in river discharge, justify the use of non-stationary distributions.

4.1.2 Non-stationary modeling

The non-stationary distribution that best fit the data is the LN-GPD-NE (Appendix 4.A), that includes the seasonality in the parameters of the distribution using a Fourier time Series. For the discharges in the Guadalquivir, the model with minimum Bayesian Information Criterion has an order of approximation, for the Fourier series in the parameters $(\mu_{LN}, \sigma_{LN}, \xi_2)$, of (4,2,2). Figure

4.1.2 shows the pdf and cdf considering the seasonality in the parameters of the distribution. As can be seen, the improvement in the fit is noticeable.

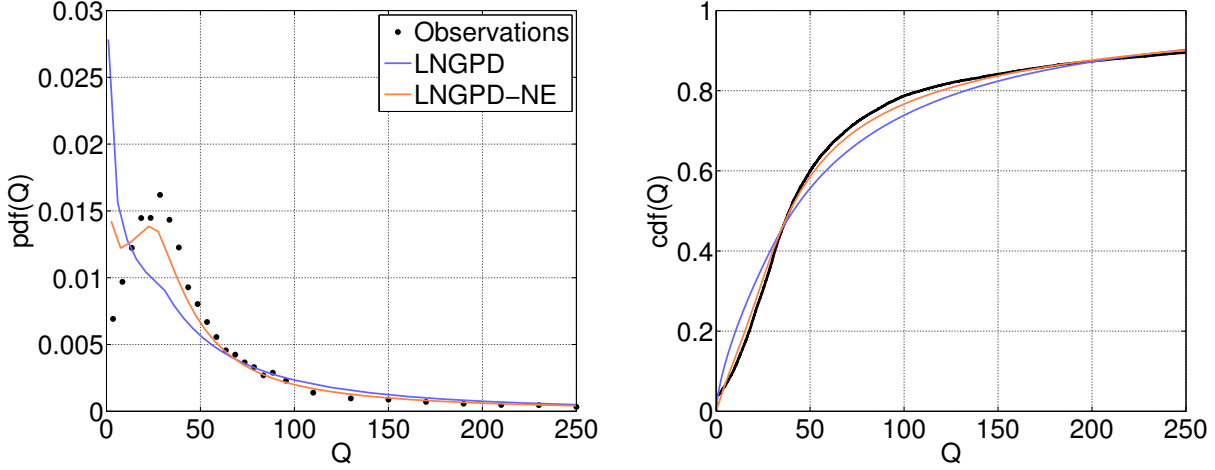


Figure 4.1.2: Pdf and cdf with the LN-GPD and LN-GPD-NE distributions.

Figure 4.1.3 shows the quantiles corresponding to the empirical accumulated probability values and those obtained when the LGN-GPD-NE. A moving window of one month was used to obtain the empirical quantiles. The lower-most part of the tail is not well reproduced, for quantiles ≤ 0.1 ($\sim 10 \text{ m}^3/\text{s}$). The reason is that the system is highly regulated, and further considerations should be performed to overcome this situation. Nevertheless, the rest of the quantiles are well reproduced. Then, this is the selected model when performing the simulations in the rest of the sections.

4.2 Saline intrusion: Markov Chain Monte Carlo methods & Management Scenarios Simulations

4.2.1 Markov Chain Monte Carlo Simulations

The various exponents stated in the previous section (Equation 3.3) are useful to link the results to salt transport mechanisms, and to better understand the physics of this estuary and its similarities and differences with others. However, from a management point of view, their practical applicability is limited. More heuristic, non-stationary approaches are then needed, since the adjustment of the salt intrusion to changes in the forcings is generally unsteady (Simpson, Vennell, and Souza, 2001; Banas et al., 2004).

Based on the measurements of the real time monitoring network (RTMN), we applied a simple first order Markov process (Appendix 4.B) to relate at a given semidiurnal tidal cycle t_n the saline intrusion X_2 to its value at the previous cycle, t_{n-1} and to the river flow, the tidal current range and the (easterly) wind velocity, W_p , at t_n . The saline intrusion may also depend on the precipitation, through direct rainfall in the estuarine water masses and indirectly through Q_d . In fact, precipitation and river discharges are correlated. However, the relation between both variables is not as trivial as one might expect due to the extensive upstream regulation of the drainage basin. The freshwater input from direct precipitation over the water surface, much

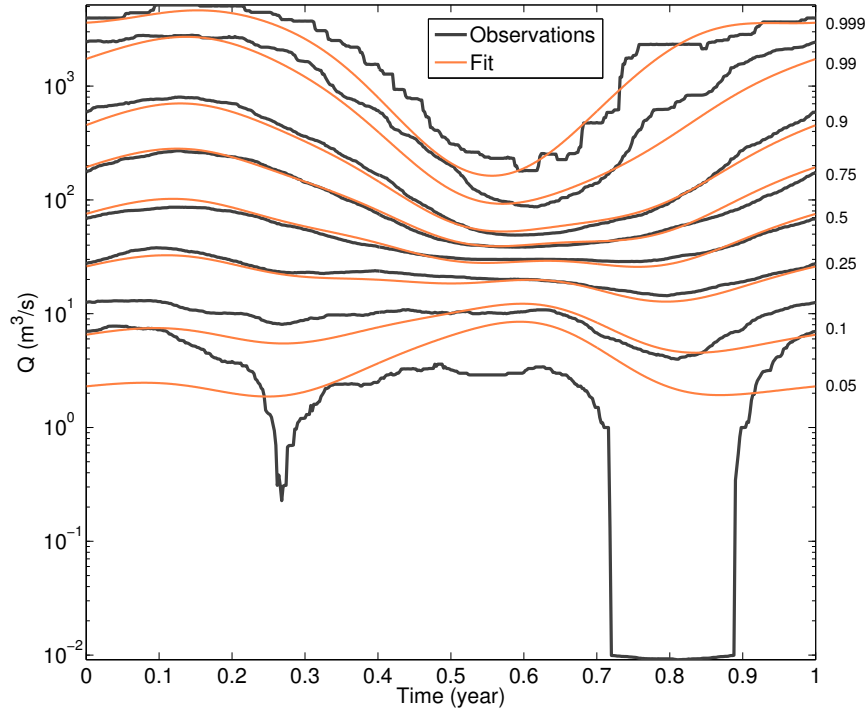


Figure 4.1.3: Iso-probability quantiles for non-exceeding probability (right numbers) equal to 0.05, 0.1, 0.25, 0.5, 0.75, 0.9, 0.99 and 0.999 empirical (black) and LGN-GPD-NE (orange) model.

lower than Q_d , is not considered. Thus, the following model, a generalization of Equation 3.3, is proposed:

$$X_2(t_n) = (1 - b_1 \Delta t) X_2(t_{n-1}) + \Delta t \left(b_2 U_t^{b_3} Q_d^{b_4} + b_5 W_p |W_p^{b_6}| \right) \quad (4.1)$$

Here $\Delta t=12.42$ hours and b_k are the fitted coefficients for both low and high discharges. Using a standard least square nonlinear regression routine, a value of $R^2=0.981$ is found for the low flow regime and $R^2=0.953$ for high river flows. Table 4.2.1 shows the coefficients for both conditions, where the saline intrusion is again expressed in km, currents in m/s and discharges in m^3/s .

Table 4.2.1: Fitting coefficients for low (first row) and high (second row) river flows. The error bars represent the 95% confidence interval.

b_1	b_2	b_3
$(9.70 \pm 7.30) \times 10^{-4}$	$(6.86 \pm 4.46) \times 10^{-2}$	$(3.89 \pm 8.07) \times 10^{-1}$
$(7.32 \pm 3.28) \times 10^{-3}$	$(3.04 \pm 6.34) \times 10^1$	$(2.63 \pm 10.64) \times 10^{-1}$
b_4	b_5	b_6
$-(7.37 \pm 6.17) \times 10^{-2}$	$-(1.52 \pm 117) \times 10^{-5}$	$-(6.64 \pm 516) \times 10^{-1}$
$-(1.00 \pm 0.48) \times 10^0$	$-(1.21 \pm 5.28) \times 10^{-2}$	$-(4.45 \pm 20.07) \times 10^{-1}$

Equation 4.1 provides an estimation of the typical time scale for the adjustment of the saline intrusion. Assuming stationary conditions, X_2 does not change significantly between two consecutive states and the response time (Appendix 4.B) is, therefore, $1/b_1\Delta t$. The response time is approx. 42 days during the low flow regime. This time is larger than the monthly timescale. During high river flows reduces to 5 days. This characteristic time scale is not far from 7.34 days, estimated for the post-river flood recovery of salinity after a single event (07-Feb-2009) (Díez-Minguito et al., 2013). The rapid salinity recovery during the latter regime seems to be related to the increase of the longitudinal density gradient near the estuary mouth after the discharge.

The most significant term is the histeretic term, as the factor $(1 - b_1\Delta t)$ is close to unity in both regimes. This fact agrees with the intuitive idea that the intrusion in a tidal cycle strongly depends on the saline intrusion in the preceding cycle. This term is followed in importance by the interaction term $b_2U_t^{b_3}Q_d^{b_4}$. The less significant one is the last term in Equation 4.1, responsible for the wind influence. Notice that the coefficient b_5 that accompanies with the wind term is negative during both conditions. This wind influence is in agreement with the observations in the estuary. The E-W orientation of the estuary mouth causes the local westward winds to contribute to an increase in salinity inside the estuary, thus increasing the saline intrusion and reducing the flushing time (Scully, Friedrichs, and Brubaker, 2005). These winds favor the gravitational circulation, enhancing the downwind (down estuary) flow near the water surface and upwind (up estuary) flow near the bottom. Thus, this wind-induced circulation increases the injection of saltier water, which replaces the superficial, low-salinity water flushed out of the estuary.

The model includes inertia, and the tidal, fluvial and wind influence. There are several studies that predict the saline intrusion with autoregressive models (Jassby et al., 1995; Monismith et al., 2002; MacWilliams et al., 2015). Despite considering the freshwater discharge, these are missing the tidal influence in their formulation. To the purpose of this Thesis, it is also necessary to c
 whi
 cha

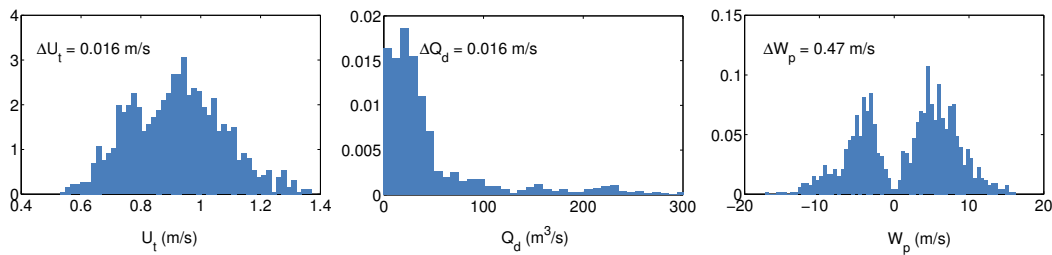


Figure 4.2.1: Probability density functions for the tidal amplitude range (left), discharge (middle) and easterly wind (right), and saline intrusion (d). Bin sizes are indicated in each panel.

The predicted saline intrusion can be estimated with Equation 4.1 using Monte Carlo simulations (Appendix 4.B), which are widely employed in many diverse areas, including coastal engineering (Benjamin and Cornell, 2014), modifying accordingly the probability distribution of Q_d . The methodology used here is based on Markov Chain Monte Carlo (MCMC, Appendix 4.B) simulations that include the assessment of the uncertainty in the results (Berg, 2005). Specifically, MCMC method stochastically generates a saline intrusion value at time t_n from

the immediately previous state of the system at t_{n-1} . The states are therefore correlated, and the desired probability distribution is reached asymptotically (i.e., for large n). Implicitly, it is assumed that the morphodynamic of the estuary do not change during the simulation time and that the values of Q_d , U_t , and W_p are uncorrelated. The non-zero lag cross-correlations between these variables, denoted by $\langle \cdot, \cdot \rangle (\tau)$, are found to be rather weak ($\langle U_t, W_p \rangle = -0.03$ at $\tau = -8$ tidal cycles; $\langle Q_d, W_p \rangle = 0.05$ at $\tau = 0$ tidal cycles; and $\langle Q_d, U_t \rangle = 0.20$ at $\tau = -2$ tidal cycles). Probability distribution functions of $X_2(t_{n-1})$, and W_p are obtained from the RTMN measurements, namely, a total of 587 days of consecutive data (see Figure 4.2.1). The distribution function for Q_d was constructed from a time series of almost 80 years. Stochastic time series are obtained by sampling these distribution functions, except for U_t , which is determined deterministically from the known tidal constituents (Díez-Minguito et al., 2012) through a harmonic analysis (Pawlowicz, Beardsley, and Lentz, 2002). Then, the Markovian process expressed by the Equation 4.1 was solved.

The state is computed from the low or high river flow fit depending on the value of the preceding state discharge. The initial time, $t=0$, was arbitrarily set up the 14-Jun-2008. MCMC simulations show that the sensitivity to the initial condition, $X_2(0)$, is weak, and the non-equilibrium steady-state is reached after a few MC steps. The resultant probability density function of the process $X_2(t_n)$ for a single run with $X_2(0)=80$ km is shown in Figure 4.2.2 (black line). The match between the observed and the computed function is fair, although the maxima are somehow diffused. However, the model captures the general shape of the function, in particular, the bimodality. Curiously enough, as shown in Figure 4.2.2, the simulated intrusion penetrates rarely all the way to the dam (110 km). During the field campaign, the maximum observed intrusion was 78.4 km, and thus never reached the head dam. The value of the mean salinity intrusion obtained with the 15 year MCMC simulation was $\overline{X_2} = 48.89$ km, rather close to the observed value ($\overline{X_2} = 46.31$ km).

4.2.2 Management Scenarios Simulations

The relationship of Equation 4.1 is used to predict, on a medium-term basis, the changes in the saline intrusion as a consequence of two different management strategies. The first one affects Q_d and the second one the water depth, after deepening the navigation channel. According to CEDEX (2011), the expected decrease of freshwater discharges for the next 15 years is by 15%. The deepening represents an increase of the water depth in the navigation channel of 23%. It is important to notice that, during the simulations, the coefficients of Equation 4.1 are kept fixed. It is likely that these would change after the scenarios. However, the records to fit the expressions are long enough and representative of a wide range of states. Hence, the possible deviation of these coefficients in response to the scenarios would be of lower magnitude than the values itself. This reasoning was extended to Section 4.3.

The scenario of the freshwater decrease was designed reducing, accordingly, the values of Q_d from the original record. Then, a new non-stationary distribution (Section 4.1.1) for this synthetic time series was fitted. The increase in the water depth was associated with shifts in the tidal current amplitude distribution. To that, the deterministic one-dimensional tidal model of Prandle and Rahman (1980) was used, with the calibrated parameters for the Guadalquivir (Estévez-Ortega, 2016). As above mentioned, the calibration parameters are kept fixed. In this case, the shift is introduced by changing the amplitude and phase of the semidiurnal component M2. It should be observed that this model underestimates the effects of deepening since the

friction parameter does not change. Pawlowicz, Beardsley, and Lentz (2002) was used to predict the astronomical tidal range. Equation 4.1 only includes the tidal amplitude in instrument α_1 . Nevertheless, considering nearby and upper stretches, and maximum deviations in the increase of the water depth of 10%, yields to a rise in the tidal current amplitude of $\sim 25\%$. Then, the mean of the tidal current amplitude distribution is displaced according to this value.

The Markovian process is solved again with the same initial conditions of Section 4.2.1. Fifty runs were done, with 15 years duration each. The results account for all the simulations. Figure 4.2.2 plots the observed and simulated probability density functions of X_2 . The expected mean saline intrusion under the freshwater scenario attains a value of $\bar{X}_2 = 52.84$ km, similar to the obtained with deepening the navigation channel $\bar{X}_2 = 51.77$. Thus, the saline intrusion would extend its reach 4 km upstream (an increase of about 8%) in both cases. Despite mean values are the same in both scenarios, the distributions significantly differ. In the case of the river discharge (green line in Figure 4.2.2), the distribution is less disperse than the obtained with the simulation of the current state (black line in Figure 4.2.2). Undoubtedly, this performance seems to be controlled by the shifts in the river discharge distribution (Figure 4.2.1), which also exhibit a reduced dispersion. About the deepening scenario distribution (orange line in Figure 4.2.2), the shape is similar to present state but displaced landward, with a spread in consonance with the tidal amplitude distribution rise (Figure 4.2.1). These reasonings are relevant from an environmental and management point of view. Results suggest that a freshwater reduction would change the current behavior of the saline intrusion in the Guadalquivir, with fewer extremes

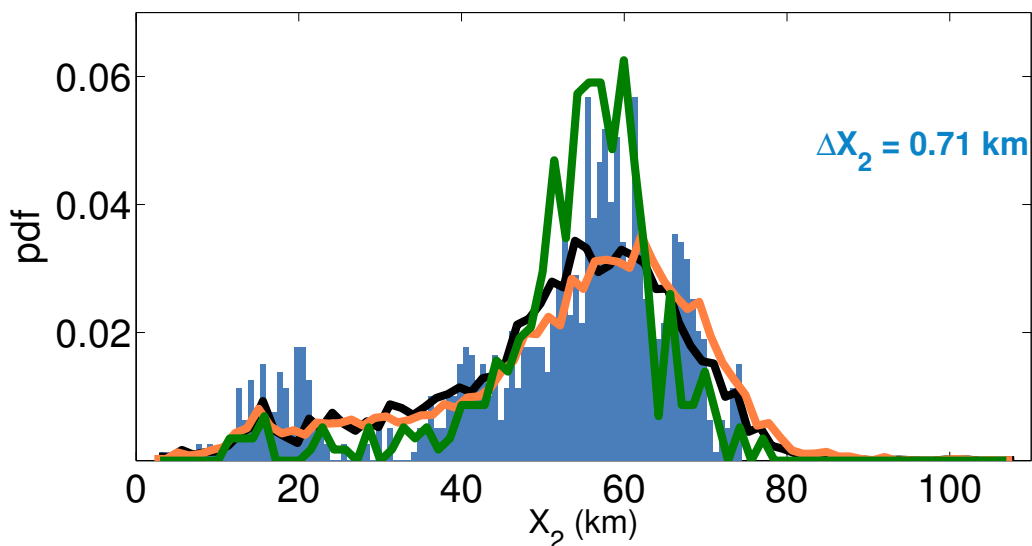


Figure 4.2.2: Probability density functions for the observed (blue bars) saline intrusion. The solid black line is the simulated saline intrusion with the Markov Chain Monte Carlo Predictions. Green line corresponds to freshwater discharge reduction. Orange line to deepening the navigation channel.

4.3 Subtidal levels and currents: Regression models & Management Scenarios simulations

Non-stationary analysis of subtidal water levels and currents was presented in Section 3.3. This section aims to represent, and therefore predict their behavior. The outstanding success of height predictions for most coastal stations has led to a complacency concerning tidal current predictions as a “solved” problem. Godin (1983) countered that estuarine currents are not practically predictable with existing techniques. One of the most cited important reasons is that virtually all estuarine currents records contain a substantial amount of variability associated with non-stationary processes. Sometimes, for low enough river discharges, levels and currents can be obtained as a linear superposition of the tidal and fluvial contributions. However, non-linear interactions between the two are the rule rather than the exception. Following models analyze both cases.

4.3.1 Regression models

The regression models corresponds to those detailed in Appendix 4.C: Godin (1999) (Equation 4.11), Kukulka and Jay (2003) (Equation 4.12) and Mixed (Equation 4.13). The fitted parameter, model performance S_k (Equation 4.16) and correlation coefficient R (Equation 4.15), are shown from Table 4.C.1 to 4.C.6. Figure 4.3.1 shows the observed and the predicted subtidal elevation in instruments β_S , β_5 , β_1 and β_0 . The figure also shows the observed and the predicted subtidal currents in instruments α_5 and α_0 .

Overall, the models reproduce better the signal at the landward-most stations. The fit coefficients with Godin and Kukulka formulation are same order of magnitude between instruments, e.g.: $s_{\eta,1}^G$ for is $\sim 10^{-1}$ and $s_{u,2}^K$ for currents is $\sim 10^{-3}$. This consistency is not observed in the Mixed model. Results suggest that, despite the improvement in the model performance with the Mixed model, the understanding of the dynamics, from a global point of view, is lost. For the sake of simplicity (parsimony principle), the interpretations are done with the first two models.

The best fit for the elevations is achieved with Godin (1999) and Mixed models. Focusing on former and according to the coefficients, with low discharges the dynamic behavior of the subtidal elevation in the GRE is mostly controlled by the astronomical tidal range. With discharges around $400 \text{ m}^3/\text{s}$ and higher, the situation changes. In this case, the results are in agreement with Díez-Minguito et al. (2012), where the subtidal elevations can be linearly related to the fresh water discharge. The Kukulka and Jay (2003) fit seems to be not adequate with small discharges, as illustrated in Figure 4.3.1. Since there is no linear term with the tidal range in Eq. 4.12, the subtidal behavior for the elevations cannot be reproduced: important spring-neap variations are dumped by the term $H_0^2/Q^{3/4}$. In addition, it should be noticed that the model considered the tidal range at the mouth, not local, which also affects the goodness of fit.

The fit for currents is slightly better with Kukulka and Jay (2003). Nevertheless, models fail to reproduce the subtidal currents during low river flows, pointing out to other processes also important and on the same order of magnitude, such as the effects of wind or the secondary circulation. This is the reason for not including the S_k and R indicators for currents case (from Table 4.C.4 to 4.C.6).

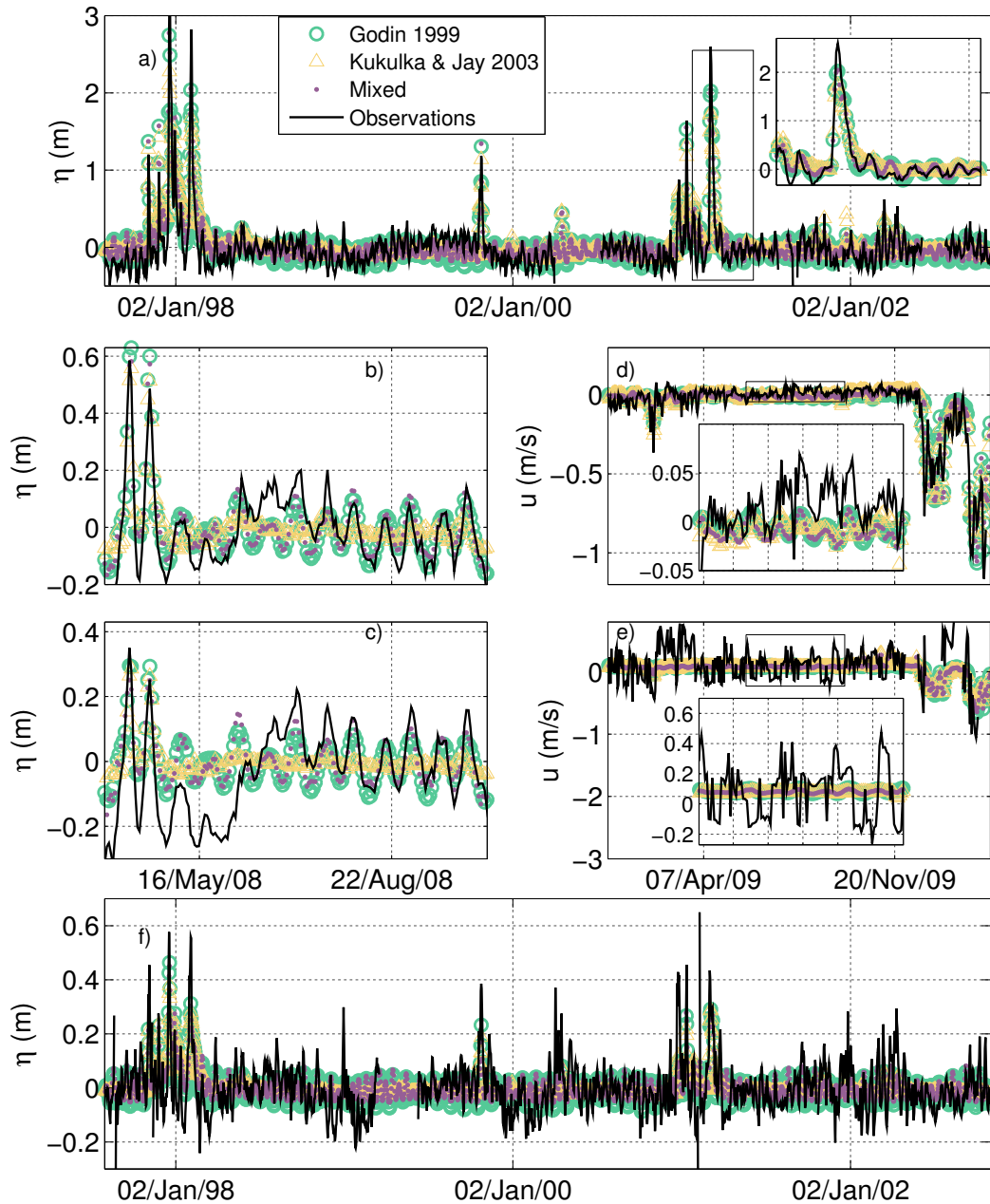


Figure 4.3.1: Panels (a) and (f): Calibration and validation at β_5 and β_0 , respectively, of Godin (1999) (green circles), Kukulka and Jay (2003) (orange triangles) and Mixed model (purple dots) regression formulae against subtidal water level obtained from observations (black curve). Panels (b) and (c): Fit of these models for water levels at β_5 and β_1 , respectively. Panels (d) and (e): Fit of these models for subtidal currents at α_5 and α_0 , respectively. Insets zoom into rectangled areas. Symbols are greater than the 95% error confidence interval.

The pdf and cdf for instruments β_6 and β_0 are depicted in Figure 4.3.2. When plotting the probability density and cumulative distribution functions with the observations and the models in Figure 4.3.2, we obtained that the upper tails are better reproduced than the lower. This fact must be considered when evaluating the results of our simulations, for example, if we intend to

assess the navigability of the channel. To improve the behavior in the low regime we included a first order autoregressive process or Markov Chain, since this technique successfully modeled the saline intrusion in the Guadalquivir Estuary (Section 4.2.1).

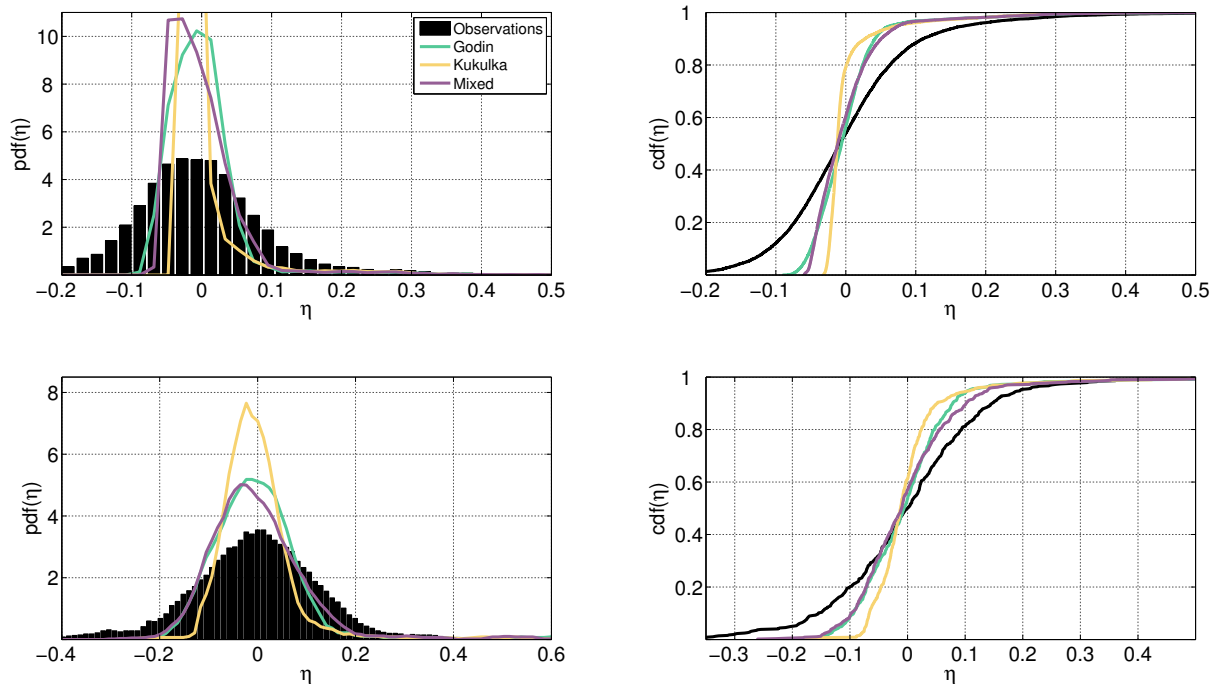


Figure 4.3.2: Pdf and cdf for subtidal elevations in β_6 (first row) and β_0 (second row) for the observed data (black color), Godin (1999) (green line), Kukulka and Jay (2003) (orange line) and Mixed model (purple line).

Markov Chain technique was considered in the regression analysis with Godin (1999), Kukulka and Jay (2003) and Mixed formulation (Appendix 4.C), in an attempt to improve the fit in low regime. The values of the new coefficients, which are not included, present the same features explained before, where the most important is the histeretic or past-time term. As we can see in Figure 4.3.3, the calibration improves, but the validation is almost the same (values not included).

The overall performance in the validation is similar, though slightly lower than without Markov Chain ($\sim 10^{-2}$). The proposed regression models does not significantly improve the fit as in the case of the saline intrusion (Section 4.2.2). The higher subtidal elevations and currents time step (25 h), that possibly attenuate or includes the past effect, can explain this fact. Also, changing the way to consider the inertia or the variables of the models, could improve the results, such as including the wind and other lateral effects as the secondary circulation. Either way, from this point, Markov Chain is not considered with subtidal elevations and currents.

4.3.2 Management Scenario Simulations

The proposed regression models (Appendix 4.C) were used to assess the effects of different scenarios into the subtidal water levels, from short- to mid- temporal scales. The mid-term simulations consider four different scenarios, related to the reduction of the freshwater discharge and the increase of the water depth after a dredging intervention. Short term simulation assesses

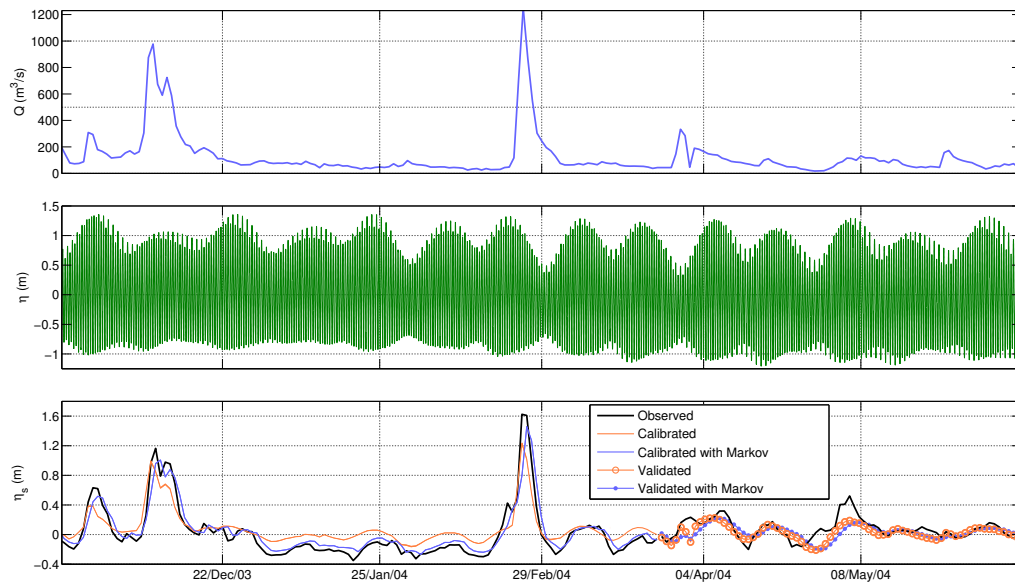


Figure 4.3.3: Upper panel: freshwater discharge from the Alcalá del Río dam. Middle panel: Astronomical tide in β_S . Lower panel: Observed subtidal elevations in β_S (dark line) for calibration and validation (dotted lines) periods with the model of Godin (1999), without (orange) and with (blue) Markov Chain.

the variation of the subtidal level after a peak discharge, supposing both the present state of the system and the response, to the same forcing, after the dredging intervention. As justified in Section 4.2.2, the coefficients of the regressions models are kept fixed during the simulations.

Mid-term simulations

Subtidal water levels depend on the freshwater discharge and the astronomical tidal range. For the different scenarios, 50 simulations with 25 years of duration each, were run. The procedure is similar to the one explained in Section 4.2.2. River discharges were stochastically simulated with the method of Monte Carlo (Appendix 4.B) using the non-stationary distribution (Appendix 4.A). A simple one-dimensional tidal model (Prandle and Rahman, 1980) assessed the changes induced by the dredging intervention (rise in the water depth). In this model, friction and the rest of parameters are supposed to remain as in the present situation. Thus, the shift in the tidal motion was applied by changing the amplitude and phase of the semidiurnal component M_2 .

The considered scenarios are as follow:

- S1: Similar discharge (Q_d) distribution with the current water depth (h), ($\sim Q_d, \sim h$).
- S2: Decrease in the freshwater discharge by a 15%, according to CEDEX, 2011. The water depth does not change ($\downarrow Q_d, \sim h$).
- S3: Increase in the water depth, from 7 to 8.5 m, according to the Port Authority of Seville. The fresh water regime does not change ($\sim Q_d, \uparrow h$).
- S4: Combination of S2 and S3 ($\downarrow Q_d, \uparrow h$).

Figure 4.3.4 depicts the pdf and cdf in β_S with the different models.

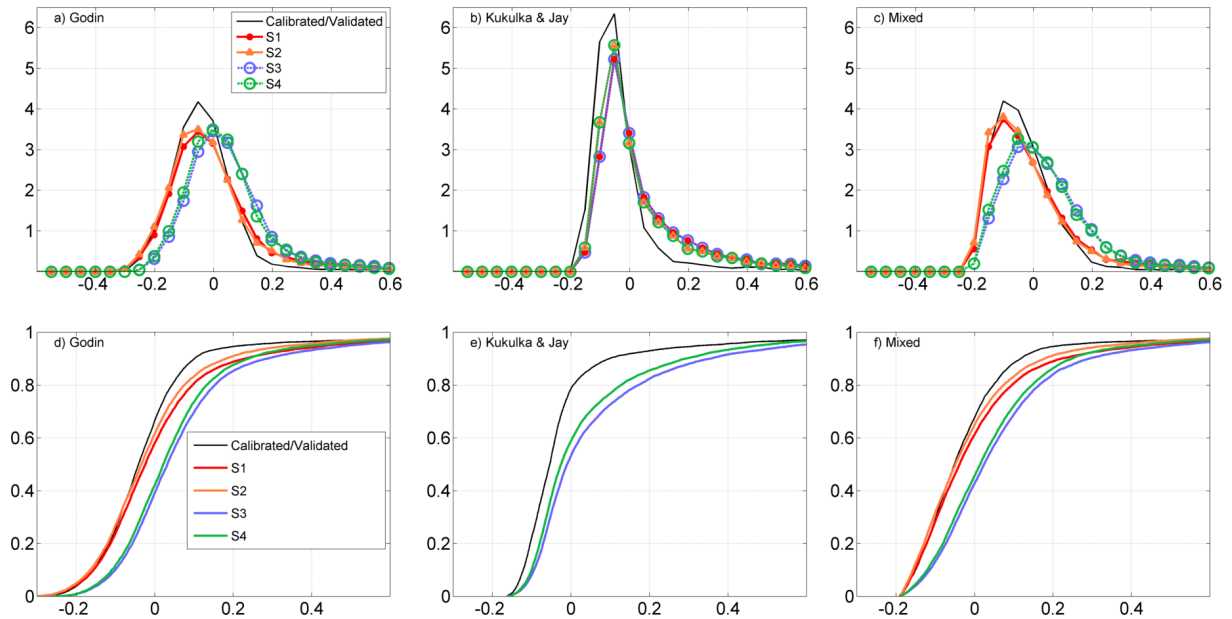


Figure 4.3.4: Pdf (first row) and cdf (second row) for subtidal elevations in β_S for the calibration and validation period (black line) and scenarios S1 (red), S2 (orange), S3 (blue) and S4 (green) for the regression models of Appendix 4.C. In Kukulka and Jay (2003) (second column), S1 overlaps S3, and S2 does the same with S4.

Godin (1999) and Mixed model, despite different values, present similar behavior (Fig. 4.3.4 panels a-c, d-f). As expected with these models, S1 (red line) reproduces better the observed values (black line) in this instrument than with Kukulka and Jay (2003). With this formulation, S1 overlaps S3, as well as S2 and S4. The reason is that the authors built their model with the astronomical tidal range at the mouth station. Since the one-dimensional tidal model fixes the harmonics in the mouth after the dredging, Kukulka and Jay (2003) can only capture a variation in the freshwater regime. In all scenarios with all models but with the mixed one, subtidal water level distributions do not have marked changes in the dispersion and tails behavior in comparison to the simulation of present state S1; in contrast to saline intrusion scenarios (Section 4.2.2).

Figure 4.3.5 displays the mean values of the subtidal levels for each scenario with the regression models. Comparing the scenarios with the current simulated situation S1, we observe that the subtidal levels decrease when the freshwater input reduces (S2), and increase as a response to deepening the navigation channel (S3). The mixed scenario (S4) is in between S2 and S3. According to the proposed values for S4 and in comparison to S1, it is possible to locate where the subtidal elevations decrease (lower stretch) or increase (upper stretch).

Short-term simulations

This section assesses the effects of a flooding in the subtidal water levels. The purpose is two-fold: firstly, to show that the presented regression models can be used as an early warning system since managers can control the river discharge released by the dam; and secondly, evaluate the response of the estuary against a flooding with or without the dredging intervention. Godin (1999) is the used model in this section.

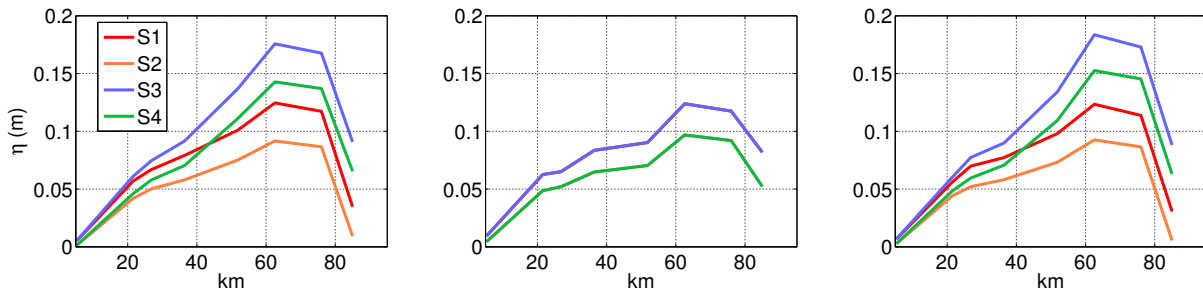


Figure 4.3.5: Along channel representation of the mean subtidal levels with the differens scenarios (S1,S2,S3 and S4) with the formulation of Godin (1999) (left panel), Kukulka and Jay (2003) (central panel) and Mixed (right panel).

The first step is to test the model against a high discharge in many instruments as possible. This corresponds to the discharges of April 2008 with peak values of $550 \text{ m}^3/\text{s}$. Figure 4.D.1 plots the subtidal levels in all the instruments along the estuary. The global coefficient of determination R^2 , using all the stations, is 0.67. The second step is to explore the along-estuary response with a higher discharge. The selected period corresponds to the winter of 2009/2010, as depicted in Figure 4.D.2. Only β_0 and β_S recorded the elevations. In this case, the fit improves, with a global R^2 of 0.81. Finally, we focus on the second period with high discharge, from 15-February 2010 and 13-March 2010. The recorded subtidal elevations in β_S were higher than 0.4 m. The performance of the observations and the predictions is $R^2=0.87$. Thus, the regression model can fairly predict the subtidal elevations in flooding. From a management point of view and delimiting, beforehand, the value of the discharge, the model can be used to draw a plan of action against flooding in the riverine communities with 25 hours in advance.

We chose this later discharge to fulfill the short-term analysis. This time, the objective was the assessment of what would have happened if the depth of the navigational channel had been deeper. In this case, the shift is introduced by modifying the harmonics. Figure 4.3.6 shows this, plotting the differences in the subtidal elevations between the current situation and the increased depth scenario. As observed, from pk 35 to the weir, the situation worsen in terms of safety. It must be noticed that this is a subtidal assessment of 25 hours. Probably, the results after accounting for higher frequency motions (discharge regarded as a 'bore') would be more adverse.

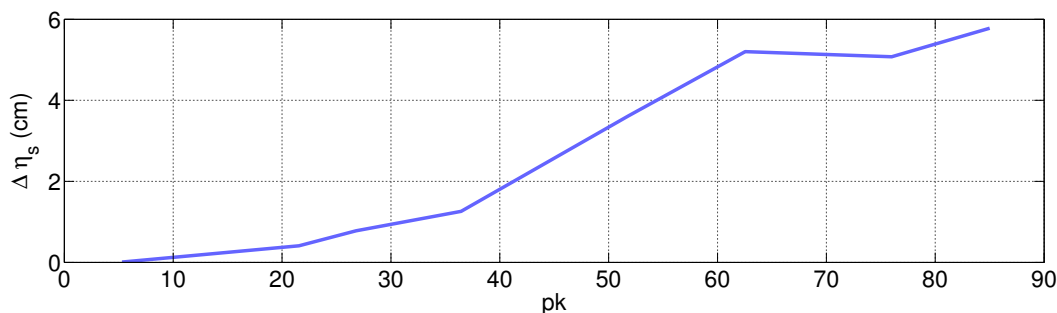


Figure 4.3.6: Computed along channel increase in the subtidal elevations (cm) as a consequence of deepening the navigation channel. The discharges values correspond to the high regime period between 15-February 2010 and 13-March 2010.

4.4 Results & Conclusions

The seasonality of the freshwater discharge in the Guadalquivir was characterized through a non-stationary mixture distribution model, with a Lognormal for the central regime and Generalized Pareto distribution for both upper and lower tails. Though the lower-most part of the discharge distribution is not captured due to the regulation of the dam, quintiles greater than 0.1 are well reproduced.

Since the adjustment of the salt intrusion to changes in the forcings is generally unsteady, a more heuristic, non-stationary approach was applied with a Markovian Chain process. This model accounted for tidal current amplitude and river flow, but also for wind conditions, in contrast to power-law relationships of Chapter 3. The most significant term is the hysteretic, in consonance with the intuitive idea that the intrusion in a tidal cycle strongly depends on the saline intrusion in the preceding cycle. This is followed in importance by the interaction term between tidal currents and freshwater discharge. Easterly winds favors the baroclinic circulation, increasing the injection of saltier water, which replaces the superficial, low-salinity water flushed out of the estuary.

Linear and non-linear regression models were applied to characterize subtidal water levels and currents. These accounted for astronomical tidal range and freshwater discharge. The best fit for elevations corresponds to a linear superposition of tidal range and discharge, while the best fit for currents includes non-linear interaction. In the Guadalquivir, these models capture the elevations better than the currents, thus focusing on the former ones. The elevation signal is better reproduced at the landward-most stations. An analysis of the subtidal levels distribution revealed that the upper tails are better modeled than the lowers, which is a relevant fact when assessing the navigability in the channel. Markov Chain processes were analyzed, but not considered in the simulations: despite the performance of the calibration notably improves with the Markov process, the validation remains the same. Probably, considering other forcings, such as the wind or secondary circulation, would be of interest for the Guadalquivir estuary.

The obtained relationships were used to predict on a medium-term basis the effect of different management strategies. Markov Chain Monte Carlo methods were used on the saline intrusion simulations. Monte Carlo techniques, with regression models, for subtidal water levels simulations. During these simulations, the coefficients that relate each of the processes within the models are fixed. The changes associated to the forcings shift is introduced in their distribution. Two scenarios were analyzed: a freshwater discharge decrease by 15% for the next years, and the deepening of the navigation channel by increasing the water depth 23%. A new non-stationary distribution computed for the freshwater discharge reduction. The shifts associated to the deepening were introduced by changing the amplitude and phase of the semidiurnal component M2 through a one-dimensional tidal model. Results show that the mean intrusion length would increase about 8% for both scenarios, from km 49 to 53. Considering the subtidal elevations simulations, the comparison between the present state and the scenarios revealed that subtidal levels decrease when the freshwater input reduces, and increase as a consequence to deepening the channel. A short term scenario was studied to assess the response of the system in case of flooding. Results point that the increase in the subtidal elevations is more significant from km 35 upstream to the dam. Overall, the simulations with the models can describe the variability in both the saline intrusion and the subtidal water level distributions, in response to the shifts of

the forcing agents regime.

4.A Non-Stationary discharge distribution

The non-stationary model includes intra-annual variations of the order of months. To our purpose, the variability is implemented with a mixture distribution (LN-GPD). The resultant model is designed as LN-GPD-NE. The mean (main-mass) states are fitted to a log-normal (LN) distribution, while the extreme (tails) states to a Generalized Pareto Distribution (GPD). Solari and Losada (2011) presented this model:

$$f(x) = \begin{cases} f_m(x)F_c(u_1) & x < u_1 \\ f_c(x) & u_1 \leq x \leq u_2 \\ f_M(x)(1 - F_c(u_2)) & x > u_2 \end{cases} \quad (4.2)$$

where F_c is the LN distribution, F_m is the GPD of minima, and F_M is the GPD of maxima. When continuity is imposed to the probability density function and the lower bound of the GPD has a value of zero, the GPD distributions are

$$f_m(x | x < u_1) = \frac{1}{\sigma_1} \left(1 - \frac{\xi_1}{\sigma_1} (x - u_1) \right)^{\left(-\frac{1}{\xi_1} - 1\right)} \quad \xi_1 \neq 0 \quad (4.3a)$$

$$f_M(x | x > u_2) = \frac{1}{\sigma_2} \left(1 + \frac{\xi_2}{\sigma_2} (x - u_2) \right)^{\left(-\frac{1}{\xi_2} - 1\right)} \quad \xi_2 \neq 0 \quad (4.3b)$$

with

$$\sigma_1 = -\xi_1 u_1 \quad \xi = -\frac{F_c(u_1)}{u_1 f_c(u_1)} \quad \sigma_2 = \frac{1 - F_c(u_2)}{f_c(u_2)} \quad (4.4)$$

The seasonal variations in the parameters $(\mu_{LN}, \sigma_{LN}, \xi_2)$, where μ_{LN} is the mean and σ_{LN} the deviation of the LN distribution, is approximated using a Fourier series whose main time-period is the year:

$$\theta(t) = \theta_{a0} + \sum_{k=1}^N (\theta_{ak} \cos(2\pi kt) + \theta_{bk} \sin(2\pi kt)) \quad (4.5)$$

where t is the time measured in years. Since the parameters of the central distribution F_c are non-stationary, the thresholds u_1 and u_2 are non-stationary as well. The maximum allowed order of approximation N is limited to 4 (minimum variation period for the parameters limited to 3 months). The parameters of the distribution are derived using maximum likelihood estimation, minimising the negative log-likelihood function Coles et al. (2001). The parameters

are estimated by progressively increasing the order of approximation of the Fourier series. To evaluate the significance of the improvement in the fit obtained when the order of the Fourier series is increased, the Bayesian Information Criterion (BIC) is used (Jianqing Fan, 2005). The chosen model has the lower BIC. Hence, the approximation balances the improvement in the fit and the number of parameters to compute.

4.B Markov Chain Monte Carlo methods

4.B.1 Monte Carlo Simulation

Real-world systems can be studied by physical experiments through replications or models, which are intended to reproduce or simulate the system behavior. The simulation process predicts the response of a system using a set of parameters or variables that describe it. After repeated simulations, the sensitivity of the system's response can be assessed to variations in the parameters that characterize it.

The method of Monte Carlo is intended to simulate random variables. According to the probability distribution of the observations, the procedure is usually repeated to generate a new set of variables that are statistically similar to the experimental samples. As explained in Kottegoda and Rosso (2008), to obtain an outcome x of a variate X with continuous cumulative distribution function CDF $F_X(x)$, one can generate a value u of a $(0, 1)$ uniform random variate U . Then, the required value of X is found by using the inverse ξ CDF as $x = \xi_u$, the u th quantile of the variate.

In decision - making processes, managers frequently demand the assessment of the system behavior in response to different scenarios. This impact is evaluated with trial designs. Without disregarding laboratory experiments, numerical simulations are becoming increasingly extended, particularly when considering large and complex systems.

4.B.2 Autoregressive processes and Markov Chain

A process X_t is said to be an autoregressive process of order p , denoted as $AR(p)$, if (Chatfield, 1975):

$$X_t = \sum_{r=1}^p \phi_r X_{t-r} + \varepsilon_t \quad (4.6)$$

where ϕ_r are fixed constants and ε_t is a purely random process, a sequence of independent (or uncorrelated) variables with zero mean and variance σ^2 (white noise). As can be observed in Equation 4.6, X_t is regressed not on independent variables but on its past value. A first order process $AR(1)$ results in:

$$X_t = \Phi X_{t-1} + E_t \quad (4.7)$$

which is also called the Markov process, where now Φ equals to the assumed lag-1 autocorrelation. Thus, a Markov Chain is a random process with the property that, conditional on

its present value, the future is independent of the past, it only depends on present conditions (Grimmett and Stirzaker, 2001). These Markov process are used to model many geophysical time series (Torrence and Compo, 1998).

Markov Chain are also useful when assessing the time response of a system. Supposing a first order differential equation:

$$\frac{dX}{dt} = aX \quad (4.8)$$

For $a < 0$, then X is subjected to an exponential decay process. The discretization of Equation 4.8 where $dt \approx \Delta t$, $dX \approx X_t - X_{t-1}$ and $X = X_{t-1}$ yields,

$$X_t = (1 + a\Delta t)X_{t-1} \quad (4.9)$$

Relating Equations 4.7 and 4.9, the response time (mean life time) RT of the system can be computed as:

$$RT = \left| \frac{1}{a} \right| = \frac{\Delta t}{1 - \Phi} \quad (4.10)$$

4.C Subtidal regression models

A regression analysis is carried out in the Guadalquivir estuary. Three regression models are applied and compared. Values are subtidally averaged for a time step of 25 hours. Only the currents projected along the channel are fitted. Godin (1999) used a linear combination of tidal contribution (tidal range) and water level variation due to river discharge.

$$\begin{aligned} \bar{\eta}_G &= s_{\bar{\eta},1}^G H + s_{\bar{\eta},2}^G Q_d + s_{\bar{\eta},3}^G \\ \bar{u}_G &= s_{\bar{u},1}^G H + s_{\bar{u},2}^G Q_d + s_{\bar{u},3}^G \end{aligned} \quad (4.11)$$

This regression is applied to all the tidal gauges and current meters installed in the Guadalquivir using the local tidal range and the Q_d realised from the Alcalá del Río dam. Kukulka and Jay (2003) used the following regression (non-linear scaling):

$$\begin{aligned} \bar{\eta}_K &= s_{\bar{\eta},1}^K H_0^2 Q_d^{-4/3} + s_{\bar{\eta},2}^K Q_d^{2/3} + s_{\bar{\eta},3}^K \\ \bar{u}_K &= s_{\bar{u},1}^K H_0^2 Q_d^{-4/3} + s_{\bar{u},2}^K Q_d^{2/3} + s_{\bar{u},3}^K \end{aligned} \quad (4.12)$$

where $s_{\bar{\eta},k}^G$ and $s_{\bar{\eta},k}^K$ in Eq. 4.11 and 4.12 are fitted coefficients, and H_0 is the tidal range (station β_0). The variables are referred to the same time step.

In these expressions, the exponents correspond to the cited authors. The following expression, designed as mixed, is proposed to combine both models without indiscriminately increasing the number of parameters:

$$\begin{aligned}\bar{\eta}_M &= s_{\bar{\eta},1}^M H + s_{\bar{\eta},2}^M Q_d + s_{\bar{\eta},3}^M + s_{\bar{\eta},4}^M H^{s_{\bar{\eta},5}^M} Q_d^{s_{\bar{\eta},6}^M} \\ \bar{u}_M &= s_{\bar{u},1}^M H + s_{\bar{u},2}^M Q_d + s_{\bar{u},3}^M + s_{\bar{u},4}^M H^{s_{\bar{u},5}^M} Q_d^{s_{\bar{u},6}^M}\end{aligned}\quad (4.13)$$

This mixture model intends to find consistent exponents, in the nonlinear term, that better represent the GRE. Regressions are performed with the *nlinfit* proprietary function of MatlabTM.

The influence of long period atmospheric forcings is removed before the regression performance. These include the variations in the atmospheric pressure and the seasonal thermal-steric contribution of the ocean (Laiz et al., 2013; Laiz et al., 2015). The used expression was a sinusoid with a period of a year. This annual variation is especially noticed in β_0 and β_s . Despite nonlinear interactions, since atmospheric pressure and steric contribution are in phase, this work simply removes their contribution by assuming an annual harmonic. This removal is applied to subtidal elevations, but not to subtidal currents since the annual variation is not that marked.

The analysis also incorporates the Markov Chain technique (Section 4.B). For example, the first term of Equation 4.11 results into:

$$\bar{\eta}_G(t) = \Phi \bar{\eta}_G(t-1) + s_{\bar{\eta},1}^{G'} H(t) + s_{\bar{\eta},2}^{G'} Q_d(t) + s_{\bar{\eta},3}^{G'} \quad (4.14)$$

where $s_{\bar{\eta},k}^{G'}$ are different from those in Equation 4.11. The purpose of including this method is to assess the improvement (or not) on the fit in low regime, as occurs with the saline intrusion. Also, it is useful when computing the response time of the variables.

The model performance S_k and correlation R parameters are the selected indexes to evaluate the performance of the models. Considering O_n and P_n the observed and predicted data at N discrete points, the correlation coefficient R is defined by

$$R = \frac{\frac{1}{N} \sum_{n=1}^N (O_n - \bar{O}_n) (P_n - \bar{P}_n)}{\sigma_o \sigma_p} \quad (4.15)$$

where σ_o and σ_p are the standard deviation of the observed and computed data, respectively. The over-bar represents the mean value.

The model performance S_k proposed by Willmott (1981) is given by

$$S_k = 1 - \frac{\sum_{n=1}^N |P_n - O_n|^2}{\sum_{n=1}^N (|P_n - \bar{O}_n|^2 + |P_n - \bar{P}_n|^2)} \quad (4.16)$$

In both coefficients, values ranges from 0 to 1, meaning bad or good correlation and skill, respectively.

Table 4.C.1: Regression coefficients, model performance (S_k) and correlation (R) for the Godin (1999) model (Eq. 4.11) for subtidal elevations (in m) at the tidal gauges. Subscripts indicate error. Discharges are in m^3/s and the tidal range in m.

	$s_{\bar{\eta},1}^G \cdot 10^1$	$s_{\bar{\eta},2}^G \cdot 10^3$	$s_{\bar{\eta},3}^G \cdot 10^1$	S_k	R
β_0	0.57 _{0.036}	0.18 _{0.007}	-1.25 _{0.072}	0.44	0.53
β_1	1.68 _{0.315}	0.68 _{0.170}	-2.60 _{0.453}	0.45	0.54
β_2	1.85 _{0.554}	0.76 _{0.325}	-2.92 _{0.826}	0.35	0.46
β_3	1.57 _{0.515}	0.96 _{0.265}	-2.55 _{0.736}	0.29	0.42
β_4	2.33 _{0.346}	1.17 _{0.169}	-3.81 _{0.517}	0.68	0.72
β_5	2.53 _{0.330}	1.50 _{0.144}	-4.79 _{0.559}	0.71	0.74
β_6	2.22 _{0.302}	1.40 _{0.150}	-4.79 _{0.593}	0.68	0.71
β_S	2.94 _{0.158}	1.16 _{0.020}	-6.28 _{0.297}	0.83	0.84

Table 4.C.2: Regression coefficients, model performance (S_k) and correlation (R) for the Kukulka and Jay (2003) model (Eq. 4.12) for subtidal elevations (in m) at the tidal gauges. Subscripts indicate error. Discharges are in m^3/s and the tidal range in m.

	$s_{\bar{\eta},1}^K \cdot 10^5$	$s_{\bar{\eta},2}^K \cdot 10^3$	$s_{\bar{\eta},3}^K \cdot 10^1$	S_k	R
β_0	1.23 _{0.378}	2.09 _{0.091}	-0.33 _{0.025}	0.34	0.45
β_1	-1.40 _{4.698}	5.84 _{1.335}	-0.55 _{0.166}	0.25	0.38
β_2	2.03 _{6.472}	5.46 _{2.532}	-0.45 _{0.282}	0.12	0.26
β_3	3.18 _{6.905}	7.89 _{1.962}	-0.76 _{0.244}	0.22	0.35
β_4	2399.37 _{3581.493}	8.51 _{1.500}	-0.83 _{0.185}	0.43	0.52
β_5	-0.35 _{4.327}	11.33 _{1.254}	-1.05 _{0.148}	0.53	0.60
β_6	-3.49 _{4.177}	10.70 _{1.211}	-0.98 _{0.143}	0.53	0.60
β_S	7.05 _{0.815}	12.42 _{0.265}	-1.69 _{0.064}	0.75	0.77

Table 4.C.3: Regression coefficients, model performance (S_k) and correlation (R) for the Mixed model (Eq. 4.13) for subtidal elevations (in m) at the tidal gauges. Subscripts indicate error. Discharges are in m^3/s and the tidal range in m.

	$s_{\bar{\eta},1}^M \cdot 10^0$	$s_{\bar{\eta},2}^M \cdot 10^3$	$s_{\bar{\eta},3}^M \cdot 10^0$	$s_{\bar{\eta},4}^M \cdot 10^0$	$s_{\bar{\eta},5}^M \cdot 10^0$	$s_{\bar{\eta},5}^M \cdot 10^3$	S_k	R
β_0	1.37 _{31.963}	0.17 _{0.008}	0.03 _{0.261}	-1.46 _{30.246}	0.94 _{2.496}	-0.49 _{10.838}	0.45	0.54
β_1	0.64 _{0.597}	0.32 _{0.219}	23.74 _{1039.144}	-24.55 _{1014.109}	0.03 _{-22.576}	-1.25 _{52.814}	0.53	0.60
β_2	-2.03 _{230.592}	0.85 _{0.400}	0.05 _{3.906}	1.89 _{228.663}	1.13 _{14.448}	-1.74 _{197.399}	0.36	0.47
β_3	0.18 _{0.442}	0.73 _{0.481}	45.91 _{58706.413}	-46.23 _{58660.223}	0.00 _{-45.339}	-0.40 _{511.850}	0.31	0.43
β_4	0.24 _{0.047}	1.09 _{0.198}	-0.37 _{0.071}	-0.11 _{0.104}	0.67 _{5.801}	-968.67 _{-63.906}	0.69	0.73
β_5	3.07 _{38.545}	1.28 _{0.177}	0.94 _{6.165}	-4.17 _{28.348}	0.77 _{3.061}	-2.78 _{22.832}	0.73	0.76
β_6	2.19 _{15.506}	1.05 _{0.181}	0.98 _{4.753}	-3.32 _{7.772}	0.72 _{1.970}	-4.90 _{18.246}	0.71	0.74
β_S	0.52 _{0.172}	1.18 _{0.021}	-1.34 _{0.815}	0.69 _{1.281}	-1.48 _{1.448}	-18.63 _{11.660}	0.83	0.85

The record in β_0 and β_s is long enough to calibrate and validate the model. In the rest of β and α , no validation is attempted due to the small available data period. In these cases, the models are only calibrated. To unify the results, the performance is shown as the mean of calibration and validation (when available) periods.

Table 4.C.4: Regression coefficients for the Godin (1999) model (Eq. 4.11) for subtidal currents (in m/s) at the current meters. Subscripts indicate error. Discharges are in m^3/s and the tidal range in m.

	$s_{\bar{u},1}^G \cdot 10^2$	$s_{\bar{u},2}^G \cdot 10^3$	$s_{\bar{u},3}^G \cdot 10^2$
α_0	2.58 _{5.320}	-0.25 _{0.062}	5.32 _{8.673}
α_1	-5.83 _{1.980}	-0.40 _{0.017}	-1.32 _{2.965}
α_2	-1.14 _{2.968}	-0.13 _{0.020}	5.95 _{4.163}
α_3	6.40 _{3.204}	-0.32 _{0.021}	0.07 _{4.362}
α_4	-0.27 _{3.072}	-0.45 _{0.014}	-7.74 _{4.312}
α_5	3.27 _{2.372}	-0.36 _{0.014}	-5.01 _{4.104}

Table 4.C.5: Regression coefficients for the Kukulka and Jay (2003) model (Eq. 4.12) for subtidal currents (in m/s) at the current meters. Subscripts indicate error. Discharges are in m^3/s and the tidal range in m.

	$s_{\bar{u},1}^K \cdot 10^4$	$s_{\bar{u},2}^K \cdot 10^3$	$s_{\bar{u},3}^K \cdot 10^1$
α_0	0.61 _{0.578}	-2.95 _{0.816}	1.07 _{0.244}
α_1	-0.15 _{0.169}	-5.05 _{0.214}	-0.63 _{0.078}
α_2	0.27 _{0.241}	-1.60 _{0.252}	0.52 _{0.104}
α_3	-0.14 _{0.214}	-4.09 _{0.259}	1.16 _{0.096}
α_4	-0.03 _{0.165}	-5.82 _{0.173}	-0.39 _{0.071}
α_5	-0.04 _{0.150}	-4.61 _{0.173}	0.37 _{0.066}

Table 4.C.6: Regression coefficients for the Mixed model (Eq. 4.13) for subtidal currents (in m/s) at the current meters. Subscripts indicate error. Discharges are in m^3/s and the tidal range in m.

	$s_{\bar{u},1}^M \cdot 10^0$	$s_{\bar{u},2}^M \cdot 10^3$	$s_{\bar{u},3}^M \cdot 10^0$	$s_{\bar{u},4}^M \cdot 10^0$	$s_{\bar{u},5}^M \cdot 10^0$	$s_{\bar{u},5}^M \cdot 10^3$
α_0	0.20 _{0.631}	-0.25 _{0.066}	0.54 _{0.898}	0.01 _{0.098}	10.04 _{54.153}	-53.07 _{214.048}
α_1	-0.37 _{0.337}	-0.40 _{0.017}	-0.39 _{0.438}	-0.00 _{0.000}	176.49 _{429.610}	-11.39 _{27.278}
α_2	-0.08 _{0.311}	-0.13 _{0.023}	0.50 _{0.533}	0.01 _{0.073}	-0.71 _{30.900}	-46.99 _{107.654}
α_3	-171.21 _{59380.741}	-0.30 _{0.027}	1.64 _{4.828}	17.04 _{5954.773}	10.08 _{36.251}	-0.04 _{13.418}
α_4	-0.53 _{2.821}	-0.42 _{0.024}	-975.95 _{1654122.119}	97.59 _{165509.793}	0.01 _{991.555}	-0.01 _{18.045}
α_5	-28.29 _{2312.822}	-0.35 _{0.017}	1.90 _{10.080}	2.65 _{233.016}	10.54 _{53.651}	-0.10 _{8.585}

4.D Regression models associated results

Some of the graphics of the current chapter are gathered in this Section.

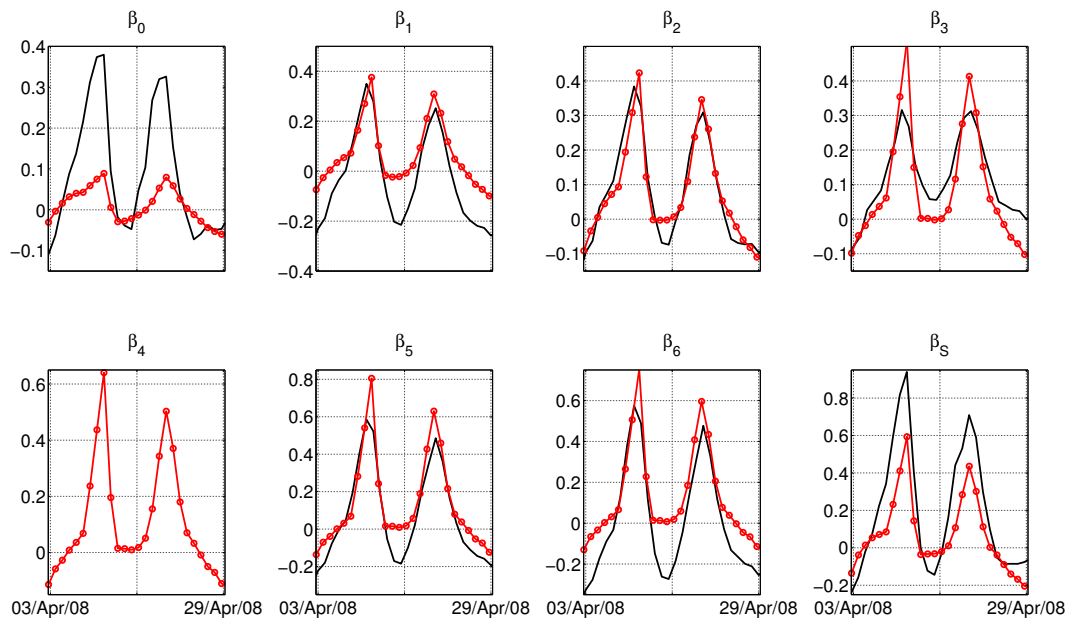


Figure 4.D.1: Observed (black line) and modelled (red dotted line) subtidal levels (m) during the discharges of April 2008 (peak values of $550 \text{ m}^3/\text{s}$) in the indicated tidal gauges.

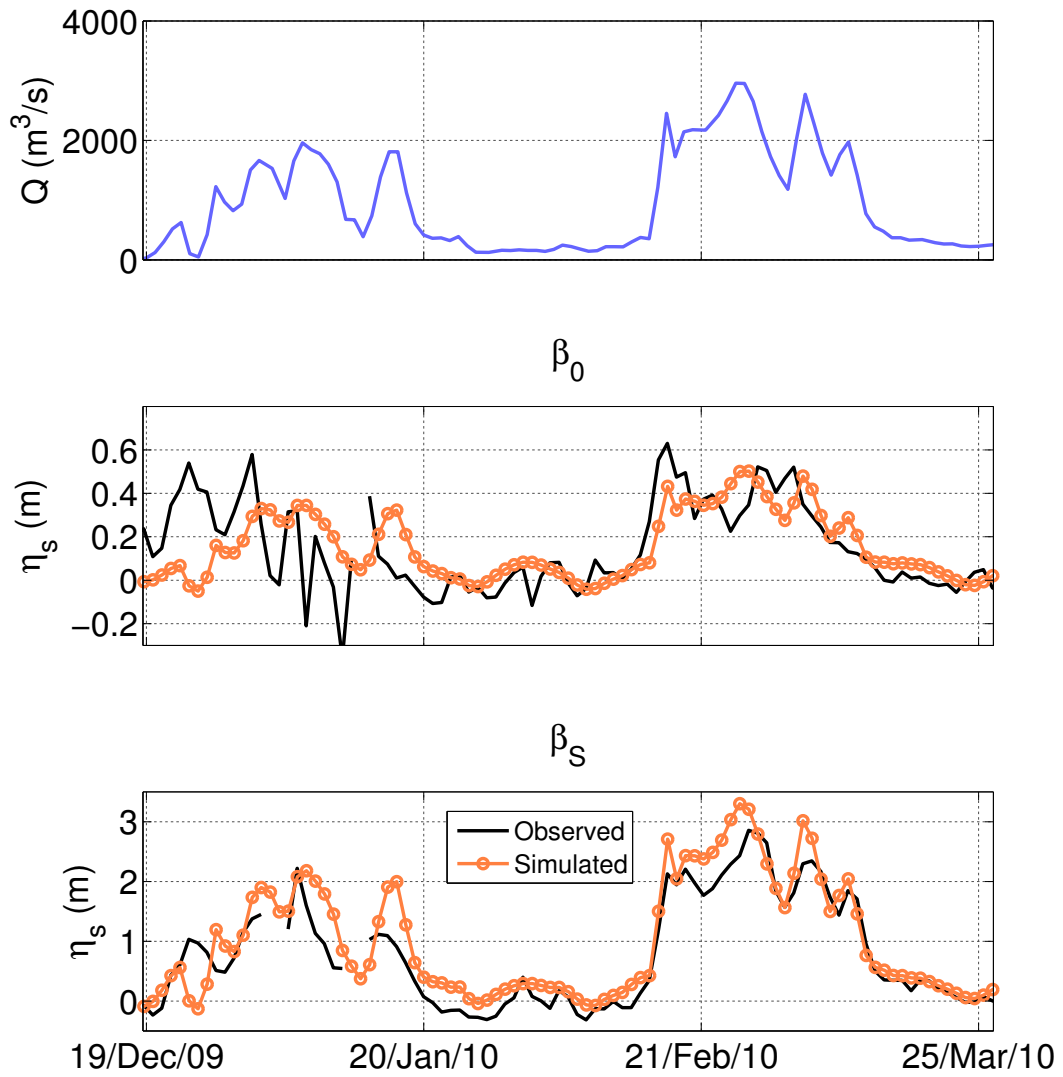


Figure 4.D.2: River discharge (upper panel) and observed (black) and modelled (orange) subtidal elevations in β_0 (middle panel) and β_S (lower panel).

ANALYSIS OF PROCESSES AND DREDGING ALTERNATIVES IN THE PUNTA UMBRÍA INLET

The Punta Umbría inlet on the Spanish southern Atlantic coast exhibit constant changes in the morphology as a result of natural forcing dynamics and dredging activities. A deep analysis of the dredging projects in the ports managed by the Regional Government pointed the Punta Umbría inlet as an especially problematic port; with one of the highest average prices per intervention and where the volume of mobilized sediment is the second highest. Between 2002–2015, three different navigation channel designs were performed to ensure the operational capacity and security through the inlet to the inland port. Since the economic and environmental impacts are elevated, regional managers are demanding a more efficient alternative.

Section 5.1 review the techniques to study the tidal inlets morphodynamics. Section 5.2 presents case of the Punta Umbría inlet. A monitoring network was installed all along the channel and the continental shelf between one and six months, while the evolution of the bed morphological activity was assessed with 18 detailed bathymetries performed in the past decade, as presented in Section 5.3. In Section 5.4, these observations were used to identify and quantify different states of the inlet regarding the dredging activities. To better understand bathymetric complexities and their interrelation to hydrodynamics, a numerical model was calibrated and validated. Both the tidal and wave energy fluxes and their relative importance were computed. The divergence of these energy fluxes was related to the morphological activity. Results indicated that the locations with greater observed sedimentation tendency correspond to those with higher divergence in the energy fluxes. Thus, Section 5.5 proposed an alternative management strategy to the present navigation channel designs, minimizing the divergence of the energy fluxes responsible of the sedimentation tendency in the inlet.

5.1 Tidal inlets: A management approach

The management of coastal environments is complex due to the dynamic and frequently changes in the forcings and physical features, the presence of valuable ecosystems of great productivity and biodiversity, and the numerous human activities depending on the coastal area for their operation (Cicin-Sain et al., 1998). In this framework, estuaries and tidal inlets play a significant environmental role and provide many benefits to human activities, such as navigational access for commercial, fishing and recreational purpose (Dean and Dalrymple, 2004).

For the maintenance and extension of these environments, particularly considering erosive and sedimentation processes, dredging interventions and/or engineer structures are frequently required (Van Rijn, 2005). Furthermore, there is a growing concern regarding the short- and medium-term effects of these interventions. Thus, both deeper evaluation of the environmental impact of these activities and more sustainable strategies are being demanded (Bray, 2008).

Tidal hydrodynamics and wave climate are the two main agents responsible of the coastal inlet morphodynamics (FitzGerald and Buynevich, 2003; De Swart and Zimmerman, 2009). The assessment of the mechanisms that control the long-term exchange of sediments in tidal inlets traditionally focused on the size of the inlet cross-section and the total water volume exchanged between the tidal basin and the sea (D'Alpaos et al., 2009). This concept is the basis for well-known empirical relations (O'Brien, 1931; O'Brien, 1969; Jarret, 1976). To account for the influence of wave action, Bruun and Gerritsen (1966) introduced the annual rate of littoral drift in the stability analysis. These relations has proven to be a useful tool for developing conceptual models that link the observed evolution of inlet long-term morphodynamics with forcings. However, these do not account for the human interventions, such us dredging activities, as a direct forcing to be considered.

In addition to these, there is an extensive list of process-based models that study the estuarine and inlet morphodynamic evolution and equilibrium (Schuttelaars and Swart, 1996; Lanzoni and Seminara, 2002; Stive and Wang, 2003). Considering the improvement in computing capabilities, complex 3D models were developed to study the morphological changes of these environments (Wang, Louters, and Vriend, 1995; Cayocca, 2001; Hibma, Stive, and Wang, 2004; Bertin et al., 2005; Elias et al., 2006; Wegen and Roelvink, 2008; Ridderinkhof et al., 2014; Prumm and Iglesias, 2016). These models are used to predict the estuarine and inlet response to a shift in the regime of its forcing agents (Grunnet, Ruessink, and Walstra, 2005), the effects of the sea level rise (Dissanayake, Ranasinghe, and Roelvink, 2012) and the implications of management interventions in the system (Elias and Spek, 2006; Moreno, Ávila, and Losada, 2010; Winterwerp and Wang, 2013; Maren et al., 2015). Despite these studies and to the authors knowledge, a method that infers the bed evolution directly from the hydrodynamic magnitudes is still lacking. One of the aims of this study is to relate the observed morphological activity to the forcings with numerical models, without coupling both, in order to quantitatively assesses the morphological response of the tidal inlet.

5.2 The Punta Umbría inlet: Study Area

The Punta Umbría inlet (PUI) is located in the south western part of the Iberian Peninsula, facing to the Gulf of Cádiz (Figure 5.2.1), and it is part of the so-called Ría de Huelva estuary.

The maximum transgression reached in the Flandrian (6500 BP) shaped this coastal area. Based on morphological observations, Rodríguez Vidal (1987) and Lario (1996) suggest that during this period a spit barrier arose in Punta Umbría that was cut through in 2500 BP. The resultant natural inlet originated the channel of Punta Umbría, and favoured the formation of barrier islands, sandy capes and littoral bars. In contrast, Morales, Borrego, and Jr. (2014) document that the most significant evolution of the sedimentary environment of the PUI occurred during the past 200 years. Observations prior to profound human interventions identified the estuary as an ebb-tidal delta system, with minor ebb channels, shoals and frontal lobes.

Three main port areas are established in the Ría de Huelva (Figure 5.2.1): i) the port of Punta Umbría (P.1), inside the inlet, with fisheries and recreational activities distributed in three different wharf zones, ii) the marina of Mazagón (P.2), southeastward the PUI and iii) the Huelva harbour, inside the main channel of the Ría (P.3). The pressure of these activities forced the construction of a large jetty (Juan Carlos I, Figure 5.2.1), to guarantee safety access to the Port of Huelva. This infrastructure blocked the eastern connection between PUIs channel and the Ría de Huelva, cutting the predominant northwest-to-southeast littoral drift. This resulted in accretion nearby the jetty and the generation of a new coastal area. The presence of these structures, in combination with the natural dynamics of the system, caused the PUI to be no longer in balance, with a high tendency to close. Hence, managers built a curved jetty (Figure 5.2.1) in mid 80's at the entrance of the inlet. In combination, three different types of navigational channel have been designed in the past decade: Central-drift (Cd), Down-drift (Dd) and Up-drift (Ud) (Figure 5.2.1).

PUIs channel is 5.7 km long with an approximately constant width of 250 m and mean water depth of 8.5 m in the thalweg. The morphology of the PUI is characterized by a submerged sandbar leeside the curved jetty, herein referred as shoaling area or shoal (Figure 5.2.1). This shoal is defined as the zone with water depths ≤ 1 m referred to the Lowest Astronomical Tide, ~ 3 m below the Mean Sea Level (MSL). The nearshore slope in the inlet and surroundings is smooth with values $\leq 1/100$. In the tidal flat area the material vary from fine/medium sand, with organic-rich muddy matrix, to medium/very coarse sand (Morales, Borrego, and Jr., 2014). In the inlet, medium sand ($D_{50} \sim 0.25$ mm) is the dominant. Finer sands are located southwestern the entrance, changing to coarser material (including gravels) when getting closer to the mouth.

Figure 5.A.1 shows the wave and wind rose in the area. Prevailing winds come from the west-to-north sector (54.4%), dominant direction is SW (12.8%); eastern winds are also noticeable (10.3%). Regarding deep water waves, the main incoming directions are W (43%) and SW (29.2%); waves from the SE (10.9 %) are relevant too. The estuary is mesotidal and the most energetic tidal constituent is the semidiurnal M_2 (12.42 h) (See Appendix 5.B). Tidal range varies from 1.1 to 3.2 m during neap and spring tides. Depth average currents near the mouth vary from 0.9 to 0.6 m/s, depending on ebb/flood phase. The tidal prism in PUI is $\sim 2 \times 10^7$ m³ (Reyes-Merlo et al., 2015). The fresh water discharge is not considered in this study, since it represents around 10% of the global estuarine tidal prism in the Ria de Huelva (Borrego, 1992).

5.3 Materials and Methods

The methodology is based on bathymetric field data, survey measurements and process based modeling to relate the morphology and the hydrodynamics. The bathymetric data was used to evaluate the bed activity in time and to classify the system in different states regarding the

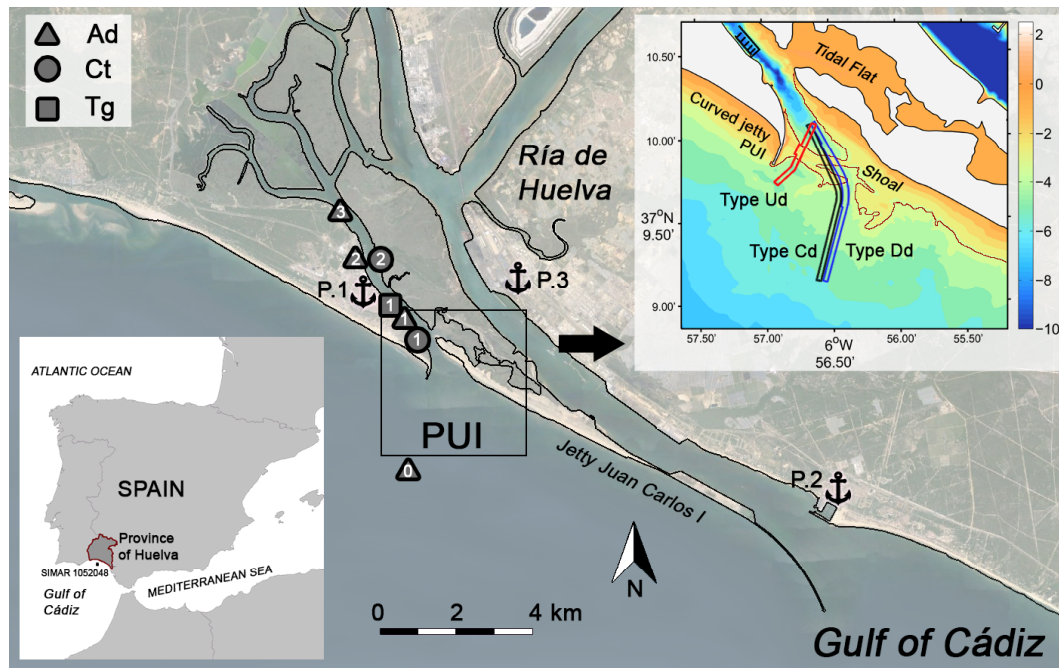


Figure 5.2.1: Overview of the Ría de Huelva estuary, including the monitoring network along the Punta Umbría channel with current meters (triangles, number 0 correspond to Ad_{ext}), environmental quality stations (circles) and tidal gauge (square). The inset includes the Punta Umbría inlet (PUI) bathymetry referred to the Mean Sea Level, pointing with the brown line the location of the shoaling area. The different designs of the navigational channels are also plotted: Up-drift (Up, red line) Central-drift (Cd, black line) and Down-drift (Dd, blue line).

dredging works. Field survey measurements were used to characterize the hydrodynamics of the PUI and to calibrate and validate the process-based model. The model enabled the computation of the divergence of tidal and wave energy fluxes, which are indicative of the erosion/sedimentation patterns. Then, these patterns were quantitatively linked to the observed bed activity. Once this relationship was established, an optimum management scenario that minimizes the bed activity in the inlet was designed.

5.3.1 Data

Hydrodynamics

Seven instruments were deployed along the main channel of the PUI and the inner continental shelf (Figure 5.2.1) between May and October 2014. A tidal gauge (Tg_1) and an environmental quality station (Ct_1), that recorded salinity and temperature, stored data during the whole period. From May 29 to June 3 another environmental quality station (Ct_2) and four acoustic doppler current profilers (Ad) were deployed. The sampling periods were 5 min for Tg_1 , and 10 min for Ct s and Ad s. The monitoring program was completed with sea level and wave information provided by Puertos del Estado (Ministerio de Fomento). The wave data correspond to the point SIMAR 1052048 (Figure 5.2.1). Data cover 57 years of wave climate sea states (1958-2015), with sample periods between 3 to 1 hour. The considered deep water variables were the wave height H_s , wave direction θ_H , wave peak period T_p , wind speed W_s , and wind direction θ_W .

Bathymetry and Topography

For the topography, land information corresponded to the digital elevation model of the Spanish Geographic Institution (IGN). Grid sizes were 5 m x 5 m in tidal flat area and 25 m x 25 m in the rest. For the bathymetry two different sources were used: continental shelf depths were provided by the Hydrographic Marine Institute of Spain (IHM), and detailed bathymetry in the PUI was supplied by the Regional Government through the Agencia Pública de Puertos de Andalucía (APPA). APPA provided a total of 18 bathymetries covering the period between 2002-2015 (Table 5.4.1). The spatial resolution in the PUI were 2 m x 2 m. The data were corrected and referenced to the MSL of the zone.

5.3.2 Numerical Model

Delft3D model was used to investigate the morphodynamics of Punta Umbría. This model is based on the three-dimensional Navier-Stokes equations under the shallow-water and Boussinesq assumptions. The Flow module (Lesser et al., 2004) with 2DH (depth-averaged) approximation was used to describe the tidal motion. The wave processes were characterized through the Wave module (Booij, Ris, and Holthuijsen, 1999).

The cartesian computational grid covered an extension of $1.3 \times 10^9 \text{ m}^2$. In the Flow module, the domain was decomposed into four parts. Cell size varied from 200 m x 200 m in the coarsest grid to 20 m x 20 m in the PUI grid. The input boundary condition corresponded to astronomic level forcing in five different locations, obtained with regional models of barotropic tide (Egbert and Erofeeva, 2002). In the Wave module, three nested grids were designed, with cell size ranging from 440 m x 220 m to 40 m x 40 m in the finest grid closer to the coast. Three boundary orientation were selected (SW-W-SE) with uniform conditions along the mesh. The input wave climate information corresponded to deep water states in the point SIMAR 1052048.

Calibration and testing

The calibrated and tested magnitudes were the elevations (η), averaged currents (eastward u , and north v) and the significant wave height H_s . Depending on the measurements, the calibration/validation periods varied from 3 to 11 days. The specific dates and the fit between the observed and modelled magnitudes, in Ad_1 and Ad_{ext} , are depicted in Figure 5.3.1.

The computed indicators to assess the correspondence between the observed and predicted values were the correlation coefficient (R , Equation 4.15), the model performance (skill, S_k , Equation 4.16) (Willmott, 1981) and the coefficient of determination (R^2). The presented values are the mean between the calibrated and the testing period.

Regarding the elevations, R , S_k and R^2 were greater than 0.9 in all the deployed instruments. The best currents fit (u,v) was found in Ad_1 ($R=(0.65,0.8)$, $S=0.9$, $R^2=(0.6,0.7)$). Northwards currents are better captured by the model than eastwards. The currents performance in the inner instruments worsen due to their proximity to the wharf zones. For H_s , the indicators R , S_k and R^2 were greater than 0.85. These results, which are in agreement with similar field studies (Zarzuelo et al., 2015), support using this model when assessing the hydrodynamics of different study site configurations in the PUI.

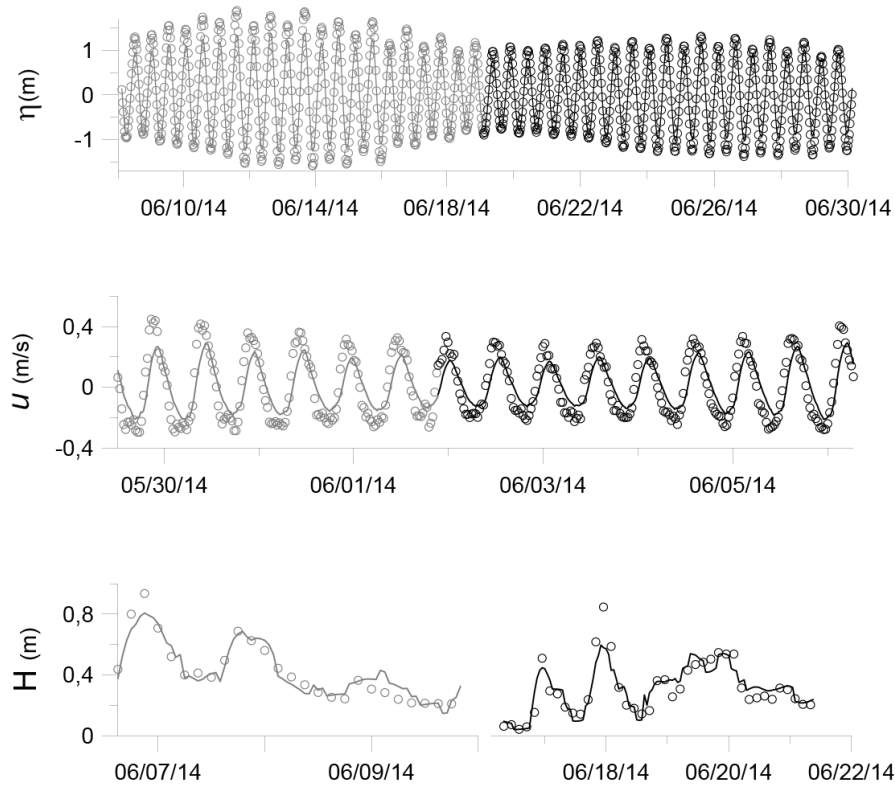


Figure 5.3.1: Predicted (line) and observed (dots) values, during calibration (gray) and validation (black) periods, for elevations in Ad_1 (top panel), eastward current u , in Ad_1 (middle panel) and significant wave height H_s , in Ad_{ext} (down panel).

5.3.3 Morphodynamics

The observed morphodynamics of the PUI were linked to the forcing agents with the following heuristic equation:

$$\frac{\partial z}{\partial t} + \alpha \vec{\nabla} \cdot \vec{F} = 0 \quad (5.1)$$

where z is the bottom depth, t time, \vec{F} the tidal and wave energy fluxes, and α is a variable that relates both terms. This coefficient implicitly accounts for the sediment properties and possible energetic dissipation not considered in the hydrodynamic computations (Section 5.3.3).

Bed evolution

The bed level evolution, evaluated in a given surface area, was defined as the Morphological Activity Index (MAI) in Eelkema et al. (2013).

$$MAI(t) = \frac{\sum_{i=1}^n |z_{t_2}(x_i, y_i) - z_{t_1}(x_i, y_i)|}{n \cdot (t_2 - t_1)} \quad (5.2)$$

where t_1 and t_2 represent two successive periods of time, and n the total number of locations with coordinates x_i and y_i where the bottom depths are compared. Equation 5.2 can be rewritten

as follow:

$$MAI(t) = \frac{1}{S} \int_S \frac{\partial |Z(S,t)|}{\partial t} \Big|_{t_1}^{t_2} dS \quad (5.3)$$

where Z is the bottom depth referred to the MSL measured inside the domain S . Previous equations do not distinguish erosion or sedimentation tendency. However, when accounting for scouring and accretion cells, both the erosive (MAI_E) and the sedimentation (MAI_S) activity can be assessed.

To explore the bed activity in the full domain, we use Equation 5.3 to define the following expression:

$$MAI(S,t) = \frac{\partial |Z|}{\partial t} \Big|_{t_1}^{t_2} \quad (5.4)$$

Energy fluxes and Divergence

The tidal depth-integrated energy flux per unit length \vec{F}_t was computed as (Zhong and Li, 2006):

$$\vec{F}_t = \rho g h \langle \vec{U} \eta \rangle \quad (5.5)$$

where ρ is the water density, h is the water depth, \vec{U} the depth-averaged velocity and η the sea level elevation. $\langle \vec{U} \eta \rangle$ is an average value over the tidal cycle. In here, \vec{F}_t is the mean of all the cycles during the referenced period. One month is simulated with the process-based model to represent the tidal behaviour, capturing the main variability due to tides in the PUI. For the computations June 2014 was chosen, with data representative of the natural state of the system (Section 5.4.3) and coinciding with the deployment of the monitoring network.

The mean wave energy flux was obtained as (Dean and Dalrymple, 1991):

$$\vec{F}_w = E \cdot \vec{c}_g \quad (5.6)$$

where E is the mean spatial energy in the water column, and \vec{c}_g is the speed of wave propagation. Applying the shallow water approximation, Equation 5.6 is expressed as:

$$\vec{F}_w = \frac{1}{8} \rho g^{3/2} H^{5/2} \quad (5.7)$$

To obtain a representative mean value of \vec{F}_w comparable to \vec{F}_t , a subset of climate states were chosen with the maximum dissimilarity algorithm described in Camus et al. (2011) and then simulated with the model. Five hundred deep water states $\{H_s, T_p, \theta_H\}$ were used. Then, all the deep water climate information (57 years of record) was related to each cell of the process-based model domain. According to the main wave directions and the computational grid, θ_H is restricted to values between 135° and 270° , covering more than the 80% of data.

The divergence of the sediment transport is commonly used to determine the erosive and sedimentation patterns (De Swart and Zimmerman, 2009). We link these patterns to the gradients of both tidal and wave energy fluxes (Equation 5.1), which are implicitly connected to common volumetric sediment transport formulation (Bagnold, 1966). No frictional dissipation is considered. Positive (negative) values for the divergence indicates erosive (accretion) tendency.

5.4 Morphology and tidal-wave competition

5.4.1 Forcings hydrodynamics

A tidal harmonic analysis (Pawlowicz, Beardsley, and Lentz, 2002) was performed to the elevation signal in the instruments. The most significant constituents in the PUI are semidiurnal, considering that the ratio between the main diurnal to the semidiurnal constituents is ≈ 0.1 . The asymmetry of the tidal wave along the estuary and the relative elevation phase (Friedrichs and Aubrey, 1988) indicate that the estuary is ebb dominated, with a greater distortion in the tidal signal up-estuary.

The tidal wave character was evaluated by means of the phase lag ϵ , defined as the difference between the time of high water slack and high water, which is closely linked to the wave celerity and the convergence (morphology) of the banks (Dronkers, 1986; Savenije, 2005). Computed ϵ values in Ad₁ and Ad₂ are close to zero, with maximum peaks of -0.2π , implying that the M_2 tidal current is $\pi/2$ out of phase with the M_2 tidal elevation. The Punta Umbría channel with a length $L \approx 6$ km, a spatial rate of change in tidal phase $k \approx 1/64$ (1/km) and length scale for along-channel variation in the M_2 tidal amplitude $|L_a^{-1}| \sim 1/115$; is dynamically short in terms of tides ($kL \ll 1$; $L/L_a \ll 1$). This behavior is rather associated with the reduced length of the estuary instead of a prominent tidal wave reflection (Friedrichs, 2010).

The tidal hydrodynamics in the inlet is characterized with the process-based model. Three significant magnitudes were calculated, depicted in Figure 5.4.1: maximum flood/ebb and residuals currents. It can be seen that Ud channel experience higher floods than types Cd and Dd, but not the higher ebbs. That may affect, indeed, the filling capacity of the navigational channel. Besides, channel Ud residual currents are, in general, smaller than in the other types. Thus, stronger floods and weaker ebbs and residual currents, may cause type Ud to silt faster than other alternatives, as observed and explained in next sections.

Regarding wind and wave climate, for H_s the most common values are between 0.5 and 1 m, for T_p from 4 to 6 s. Wind speed is between 4 to 5 m/s. The most intense and frequent waves comes from the SW. Comparing the observed values in the field survey and in deep waters, H_s in Ad_{ext} (Figure 5.2.1) was usually smaller than the one in the SIMAR, with a mean decrease of the spatial energy in the water column of 33%.

5.4.2 Navigational channels and natural state

The geometric characteristics of the main navigational channels are gathered in Table 5.4.1. The table includes the dates when the bathymetries were performed (Section 5.3.1), the different states and the morphological activity (Section 5.4.3). In the past years, Cd dredge was performed 3 times, while both Dd and Ud once. Cd and Dd are longer than Ud and have distinct dredged volume, depicted in Figure 5.4.2. In the Cd and Dd designs, the dredged volume in the shoaling

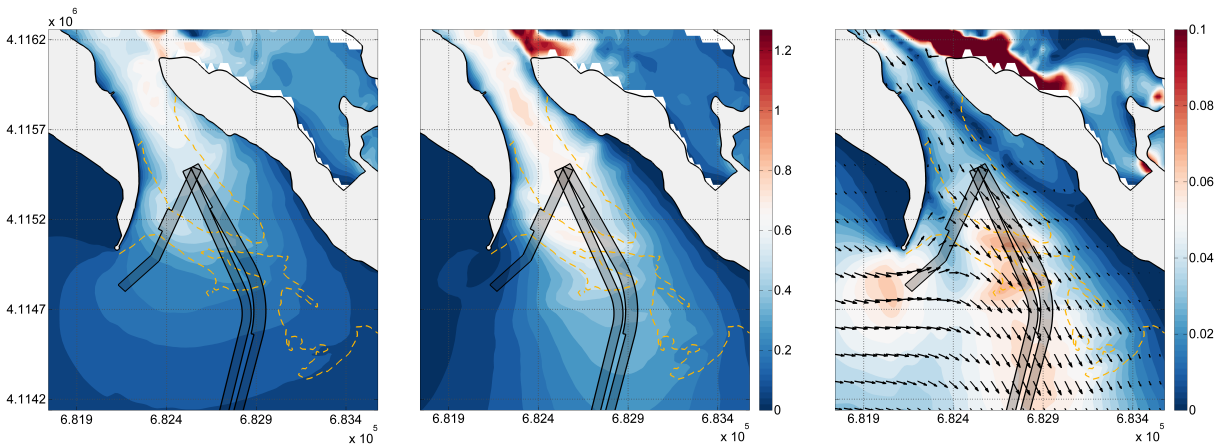


Figure 5.4.1: In m/s: panel a) mean of maximum flood currents, panel b) mean of maximum ebb currents and panel c) residual currents.

area represents $\sim 30\%$ of all the mobilized material. In type Ud, though the overall dredged volume is lower than half the other navigational channels, the extracted material in the shoal represents 65% (Figure 5.4.2). Cd and Dd channels are designed to avoid the shallowest part of the submerged sandbar of the PUI. As a result, their length is greater but their interference with the sandbar is lower. The opposite occurs with Ud type, that is intended to provide a short-cut access to the open sea; however, it crosses the most active part of the shoal in terms of sedimentation activity (Section 5.4.3).

The morphology in the PUI is subjected to this periodic dredging works. After the dredgings, the system evolves towards its previous natural state (denoted as N in Table 5.4.1). We selected as representative of this state the bathymetry of 11-Jun-2014 (Figure 5.2.1), since the previous dredging work occur ~ 4 years ago and the sampling area covers all the inlet, including the shoaling area. In addition, the morphological activity between this and the previous natural state is the lowest in the record ($MAI_T=0.2$). The analysis of the bathymetries shows that the position of the submerged sandbar does not significantly differ between natural states.

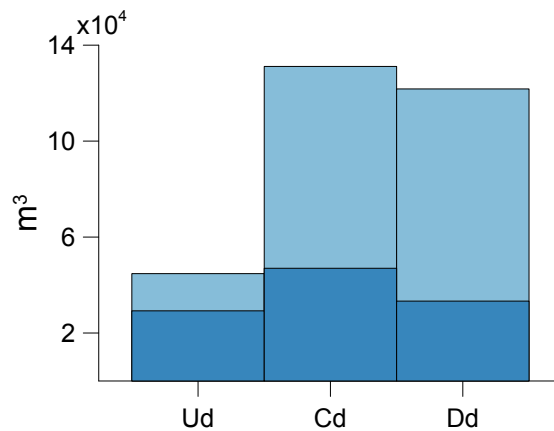


Figure 5.4.2: Total dredged volume (m³) in the channels (light blue), including the dredged volume in the shoal region (dark blue).

Table 5.4.1: Navigational channel design (1st column) at the specified dates (2nd column) corresponding to the different states at the PUI (3rd column): N: natural; dD: during Dredging; D: Dredged; aD: after Dredge. The size of the channels (in meters) is in the form of Length × Width × Depth, being Depth referred to the Lowest Astronomical Tide. The total, erosive and sedimentation MAI between successive bathymetries are computed inside the dredged area of the channel (4th, 5th and 6th columns).

Central drift	Date	State	MAI_T	MAI_E	MAI_S
[1650,1825]x[50,78]x3	01-Apr-2002	aD	4.8	1.9	5.3
	23-May-02	N	2.7	3.0	0.3
	13-Sep-02	dD	4.1	4.9	2.1
	04-Nov-02	D	2.7	1.9	3.0
	31-Jan-2003	aD	0.4	0.5	0.3
	26-Oct-04	D	0.4	0.0	0.5
	09-May-07	N	0.5	0.1	0.5
	14-Jul-08	N	3.6	3.6	0.1
	15-Dec-2008	D	0.3	0.1	0.4
Down drift					
[1870]x[50,70]x2	01-Jul-11	N/aD	0.6	0.0	0.6
	23-Jun-13	N	0.2	0.2	0.3
	11-Jun-14	N	0.5	0.7	0.3
Upper drift					
[800]x[55,80]x2.5	26-Dec-2014	N/dD	4.0	5.9	1.6
	12-Jan-2015	dD	2.1	2.9	0.9
	12-Mar-15	dD	4.0	3.4	5.2
	26-Mar-15	dD	1.4	1.9	0.6
	17-Jun-15	D	1.5	0.1	1.5
	29-Oct-15	aD			

5.4.3 Morphological activity index and states

The indexes showed in Table 5.4.1 correspond to the total (MAI_T), erosive (MAI_E) and sedimentation (MAI_S) morphological activity values inside the navigational channels. These indexes, together with a careful assessment of the observations in time, were used to define the following states in the PUI (Table 5.4.1 and Figure 5.4.3): *natural state*, *during Dredging*, *Dredged* and *after Dredged*.

In the *natural state* (N), the last dredging work was reported at least ~ 6 months before the bathymetry was collected. Between consecutive N, both the erosive and sedimentation processes are partially in balance and are less significant than in the rest of states, where the mean MAI_T is 0.4 m/year. The *during Dredging* (dD) represent the system during the dredging work, where the erosive (human-forced) processes are dominant. The duration of this activity is comprised between 2-5 months with mean MAI_T of 3 m/year. The *Dredged* (D) state corresponds to the bathymetry performed just when the dredging finishes. Finally, the *after Dredging* (aD) state indicates the situation where the system's behaviour is still controlled by the effects of the last

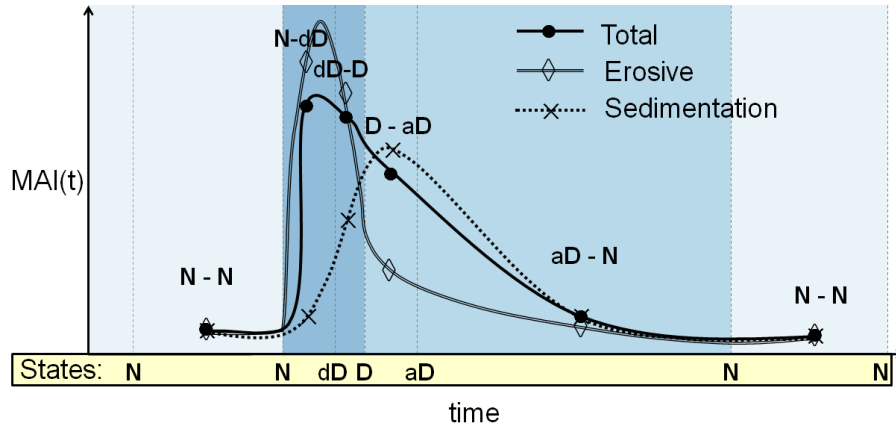


Figure 5.4.3: Diagram based on PUI observations relating the morphological activity (total, erosive and sedimentation) to different states. Dark blue includes the period where human-made processes are dominant (N-dD, dD-D). Medium blue region occurs after the dredge is ended, where sedimentation processes rise higher values (D-aD, aD-N). Light blue takes place when sedimentation and erosive process reach lower values and tend to balance (N-N).

dredging work, reported between 2-4 months after the dredge. The observed effects correspond to a rapid increase in the accretion activity in comparison with the rest of states, where the mean MAI_T is 1.6 m/year. The transition bathymetries from one channel to another (Table 5.4.1, 11-Jul-11 and 26-Dec-15) report two states. The morphological activity of similar states is in consonance but for the record between the 26th and 12th of March 2015 in Ud channel. In dD states the erosive activity is higher than the sedimentation except in this case, where a partial collapse in the navigational channel caused the MAI_S to reach 5.2 m/year.

In comparison with Eelkema et al. (2013), the morphological activity in the PUI is higher than in their case study. Apart from the differences in the forcings, it must be noticed that their MAI_T is assessed in a larger area, with lower spatial (20 m x 20 m) and temporal resolution (four years). Their observed long-term values before the construction of the storm surge barrier are consistent with our $MAI_T=0.3$ m/year, value computed for natural states in all the PUI extension (not only in the channels). Thus, the higher spatial and temporal resolution in our data enables the definition of the proposed states in the PUI.

The spatial MAI distribution derived from Equation 5.4 and depicted in Figure 5.4.4 was used to identify the most active areas in the bed. It was obtained averaging the states D-aD, aD-N, D-N and N-N, since N-dD, dD-dD and dD-D are highly affected by the dredging work (Figure 5.4.3 and MAI_T in Table 5.4.1).

Part of the channels present elevated MAI values, since they are the most altered region during the dredging processes and this influence still remain in time. Nevertheless, it can be observed in Figure 5.4.4 several active zones outside the channels domain. Then, a high active region with values greater than ~ 1.5 m/year is defined.

The assessment of the observations, together with the computation of the morphological activity index, enabled the classification of the inlet in different states regarding the dredging works. Then, the most direct effects of human-made processes on the morphology were removed from the analysis. Resulted showed that not only human interventions, but also the natural

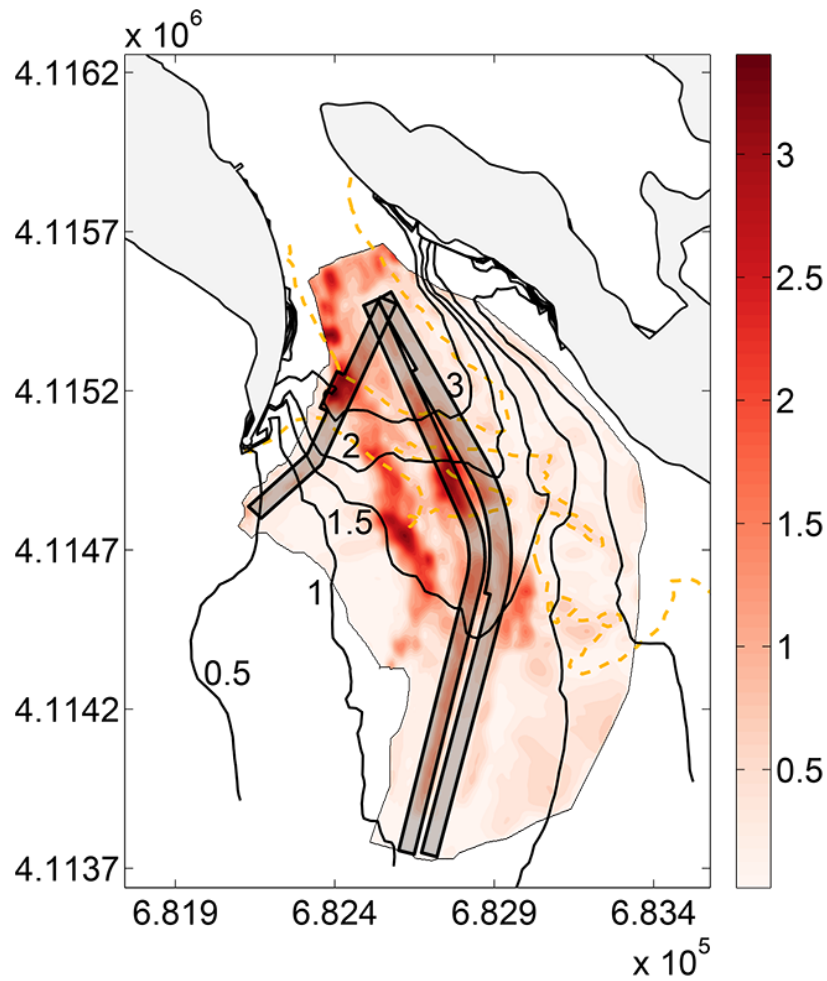


Figure 5.4.4: Average MAI index in Punta Umbría as mean of D-aD, aD-N, D-N and N-N states. Channels are depicted in black patches. It can be observed, leaside the jetty, a region close to the mouth and the sandbar (orange dashed line) with high activity (more than ~ 1.5 m/year). The figure also includes the contourlines of $F_{t/w}$ field. Higher activity is enclosed in the area with $\sim F_{t/w} \geq 1.5$.

forcing agents, play a decisive role in the morphological activity distribution inside the inlet, as presented in next sections.

5.4.4 Energy fluxes and Divergence

The results of the tidal energy flux \vec{F}_t with the natural state bathymetry are displayed in Figure 5.4.5 (Panel a). The energy flux vectors are directed landward the channel and get closer when approaching the inlet mouth, reaching maximum incoming flux inside the channel of Punta Umbría. When relating this magnitude to the observations (Figure 5.4.4), the most active zones are those with values higher than $1 \times 10^3 \text{ Wm}^{-1}$. The wave energy flux \vec{F}_w spatial distribution is represented in Figure 5.4.5 (Panel b). This energy flux decreases when approaching the PUI, with values in the navigational channels between $0.2\text{-}1 \times 10^3 \text{ Wm}^{-1}$. Predominant wave direction near the mouth is almost constant ($\sim 220^\circ$), except leeward the jetty, that diffracts.

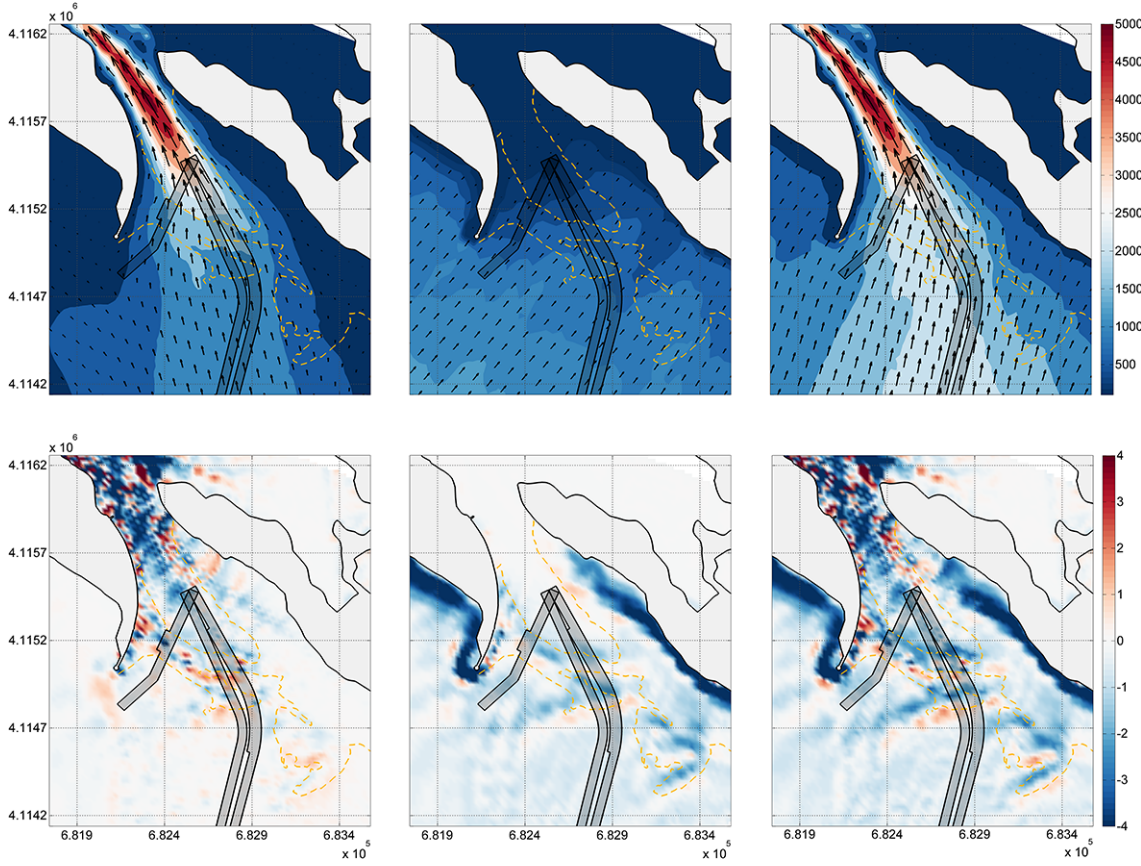


Figure 5.4.5: In Wm^{-1} : panel a) Tidal energy flux \vec{F}_t , panel b) Wave energy flux \vec{F}_w and panel c) \vec{F}_{t+w} . In Wm^{-2} : panel d) $\nabla \vec{F}_t$, panel e) $\nabla \vec{F}_w$. panel f) $\nabla \vec{F}_{t+w}$. In panels d), e) and f) positive colours mean erosion and negative sedimentation tendency.

Both tidal and wave energy fluxes are compared in Figure 5.4.4 (contour lines) in terms of their relative magnitude defined as $F_{t/w} = |\vec{F}_t|/|\vec{F}_w|$. Values higher than 1 encloses the area where dredging activities have been taking place since 2002. Then and in terms of energy, these are located inside the tidally dominated domain, since $F_{t/w}$ is indicative of the forcings prevalence. In relation with the observed morphology, the activity is more intense where $F_{t/w} \gtrsim 1.5$. With $F_{t/w} \geq 3$, contour lines rapidly strengthen and reach values in the mouth in the order of $1-10 \times 10^2$, being at the entrance of the tidal flat around 1×10^3 . This tidal-wave competition coefficient is representative of the mean hydrodynamics conditions in the inlet (See Appendix 5.B).

The other computed magnitude was the sum of both fields \vec{F}_{t+w} , represented in Figure 5.4.5 (panel c). Comparing this to \vec{F}_t , close to the mouth and southern the submerged sandbar is where the wave influence is more significant. Similar analysis was done with the model implementing each channel's bathymetry as input, presenting in Figure 5.4.6 the results of \vec{F}_{t+w} (panels a, b and c). The patterns are similar to natural state case (Figure 5.4.5 panel c) except in the deepest part of the channels and surroundings, where the values are higher. This behavior is especially noticeable in Ud, where values greater than $\sim 2000 \text{ Wm}^{-1}$ spread in a larger area. According to the results, the most active zones in the PUI are in the tidally dominated region where wave action is relevant, delimited by $1 \lesssim F_{t/w} \lesssim 3$.

Figure 5.4.5 (panels d,e,f) shows the divergence of tidal, wave and the sum of both energy fluxes with the natural state bathymetry. Negative $\nabla \vec{F}_t$ gradients are higher in the main channel between the inlet mouth and the tidal flat entrance $\sim -4 \text{ Wm}^{-2}$. Negative values of $\nabla \vec{F}_w$ in the shoreline, eastward and westward the entrance, point strong sedimentation in the coast. The divergence of both fields (Figure 5.4.5 panel f) revealed that the sedimentation in the mouth, particularly in the shoal, is stronger than the erosion. This is in consonance with the periodic dredgings. In the tidally dominated region, the contribution of waves to the sedimentation represents the 70%.

The values of $\nabla \vec{F}_{t+w}$ computed with each channel's bathymetry are depicted in Figure 5.4.6. Though the gradients show similar features as in Figure 5.4.5, they are more intense in and in the vicinity of the navigational channels. Moreover, the negative divergence in the shoaling area is higher for all the designs, particularly in Ud. These results suggest that the inlet is not in balance. Similar conclusion were revealed in Reyes-Merlo et al. (2015), as the long term stability analysis relating littoral drift and tidal prism demonstrated.

The general hydrodynamic behavior in the inlet is well represented with process-based model using the natural state bathymetry, though more accurate tendencies inside the channels are obtained when implementing each correspondent bathymetry. In the following sections both alternative calculation procedures (natural state and each channels' bathymetry) are used, being duly indicated in the text.

5.4.5 Morphodynamics

The divergence of the energy fluxes were linked to the morphological activity as proposed with Equation 5.1 and depicted in Figure 5.4.7. Sedimentation and erosive processes were studied separately. The divergence and MAI were calculated in the following regions of interest: i) Tidally dominated (T), ii) Shoaling area (S), iii) navigational Channels (C), iv) the intersection $T \cap S$, and v) the intersection $S \cap C$. The computations were assessed with Dd, Ud and two designs for Cd channel.

Focusing on the accretion in Figure 5.4.7 (panel a) it was obtained that the larger the gradients are, the larger the sedimentation activity is. The tidally dominated region presents lower activity and energy gradients. This is consistent, since the values are averaged in a larger area. If these computations are performed in this region but focusing in the shoaling area ($T \cap S$), the MAI and the divergence increases. The same occurred with the navigational channels: when averaging inside the shoaling area ($S \cap C$), both the activity and gradients are higher. Cd and Dd points present similar tendency, while the trend for Ud points in T, S and $S \cap C$ regions differs. Since Ud is in the most active part of the shoal, results suggest that another α , or a distribution of this value along the domain, could better represent the observations.

Considering only Cd and Dd, the expression that best fits the divergence of the energy fluxes (x , in Wm^{-2}) with the MAI (y , in m/year) was $y = ax + b$, ($\vec{\nabla} \cdot \vec{F}$ negative in the sedimentation case). This expression differs from Equation 5.1 in the presence of term b . The fit and the 95% confidence interval are depicted in Figure 5.4.7, with $\alpha = 0.18$, $b = 0.23$ and $R^2 = 0.6$. Then, if the negative divergence of the energy fluxes is reduced, less sedimentation activity in the bed is expected.

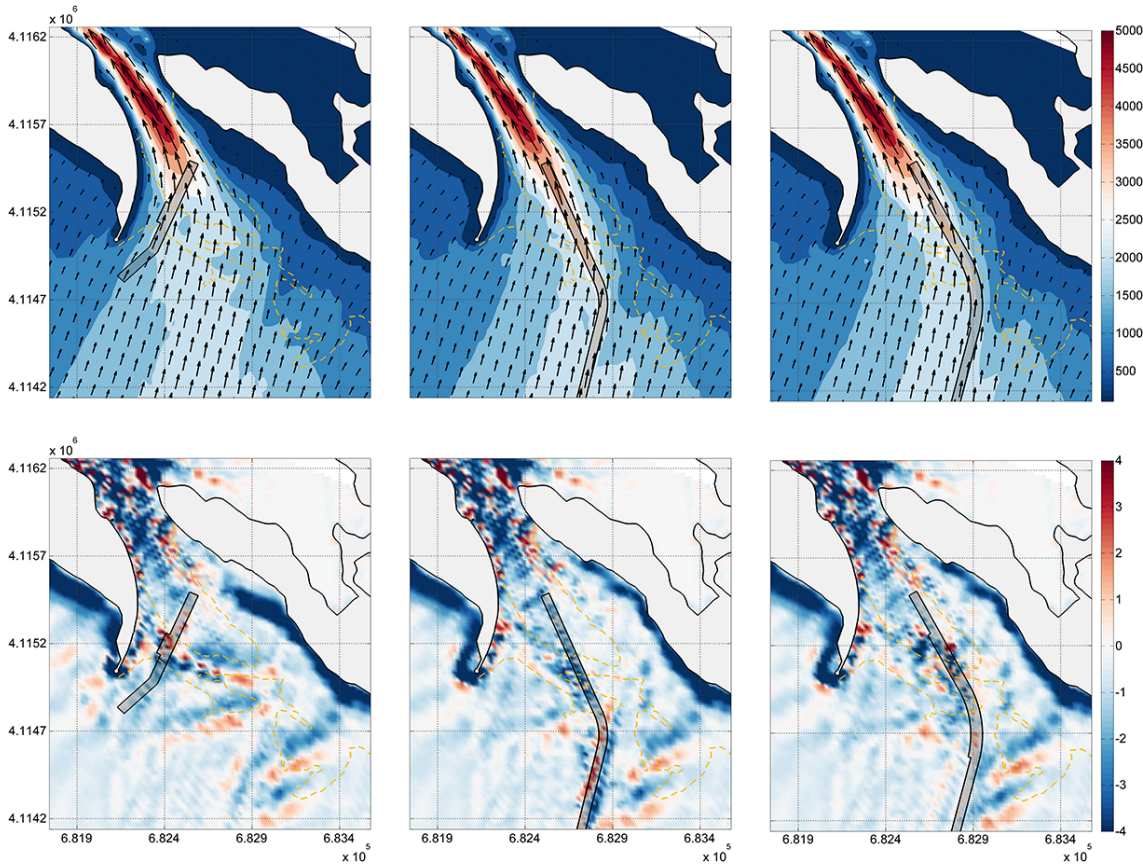


Figure 5.4.6: Total energy flux F_{t+w} (upper row, in Wm^{-1}) and its divergence ∇F_{t+w} (down row, in Wm^{-2}) of Ud (panels a,d), Cd (panels b,e) and Dd (panels c,f) channel designs.

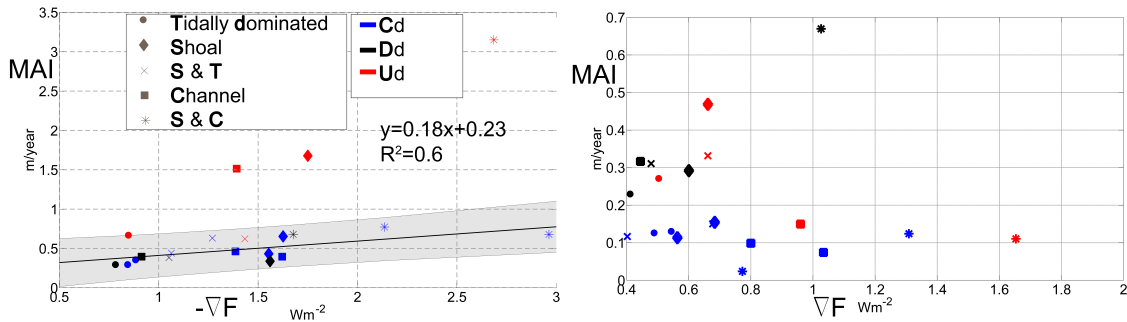


Figure 5.4.7: Comparison between MAI and negative (sedimentation, panel a) and positive (erosive, panel b) divergence of energy fluxes.

This behavior is not that clear with the erosive processes (Figure 5.4.7, panel b). Overall, the activity and gradients are less significant compared to the sedimentation case, confirming that in the PUI the accretion is stronger than the erosion. The reduced range in the MAI and gradients in the erosive input data can explain the spreading in the results. Nevertheless, these results suggest that there is a constant/linear trend between the activity and the divergence of the energy fluxes, in the same terms of the accretion tendency.

Then, reducing the energy flux gradients would result in a decrease in the bed activity in the inlet. This is the basis used to present an alternative to actual dredging works in the PUI, which focused on decreasing the sedimentation activity.

5.5 Dredging alternative in the Punta Umbría inlet

Present interventions in the PUI consist of dredging relatively narrow channels in the shoaling area, which is the most active region in the inlet. These channels do not modify the natural sedimentation tendency and they periodically collapses due to the shoal effects, as observed in the period 2002-2015. Then, in order to reduce the energy flux gradients and improve the operational capacity in the PUI, in this work we proposed to level and partially remove the shoal lee-side of the jetty instead of excavating a channel as usual.

The modified bathymetry of the alternative is depicted in Figure 5.5.1. The water depths are consistent with the requirements (~ 4 m below MSL) and the maximum differences between the initial and final profiles are ~ 2 m. The total affected region covers 7.4×10^5 m². The volume of mobilize material is 2×10^5 m³. This alternative was forced and analysed as detailed in Section 5.4.4. The results for the residual currents, total energy flux F_{t+w} and its divergence $\vec{\nabla} \cdot F_{t+w}$, are depicted in Figure 5.5.2.

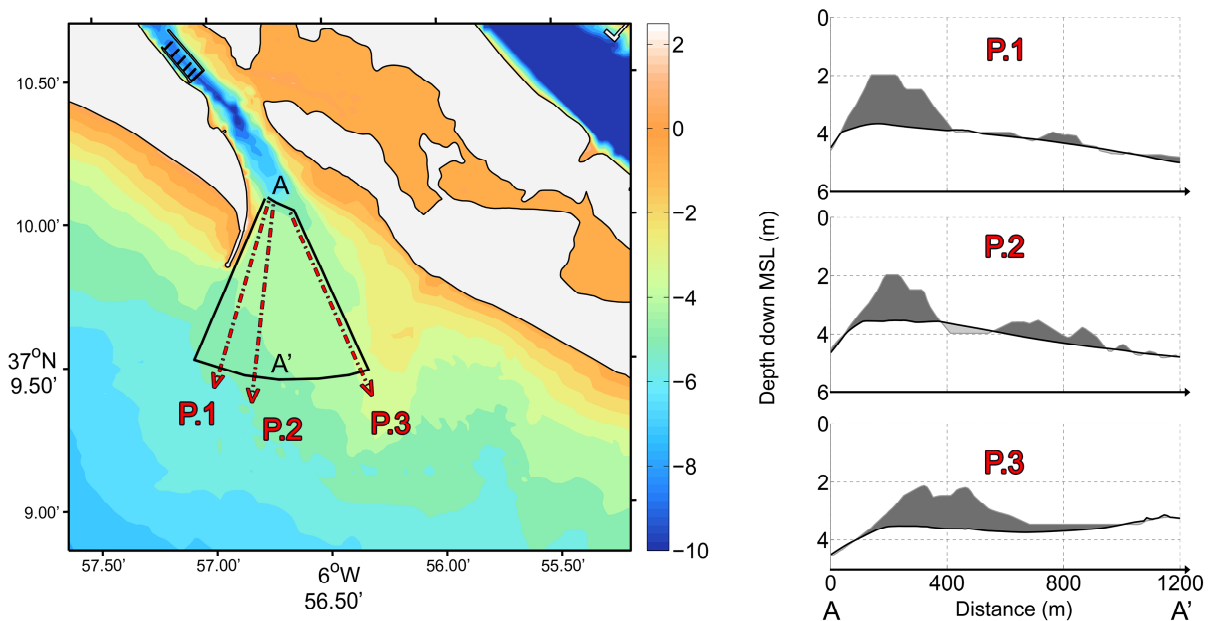


Figure 5.5.1: Proposed intervention in the PUI, consisting of removing the shoal and level the bathymetry leeside the jetty (area delimited with black line). Specific profiles are plotted (red dashed lines), where coloured dark and light gray regions represent cut and fill areas, respectively.

As a response to flattening the bathymetry and in comparison to the natural state with the presence of the sandbar (Fig 5.4.5), the residual currents decrease in the entrance of the PUI. The energy fluxes do not significantly change except at the locations close to Ud channel, with a rise of 7%, specially in the term \vec{F}_t . As expressed in Equation 5.5, this flux is proportional to the currents but also to the water depth, that notably increases. Comparing the divergences depicted

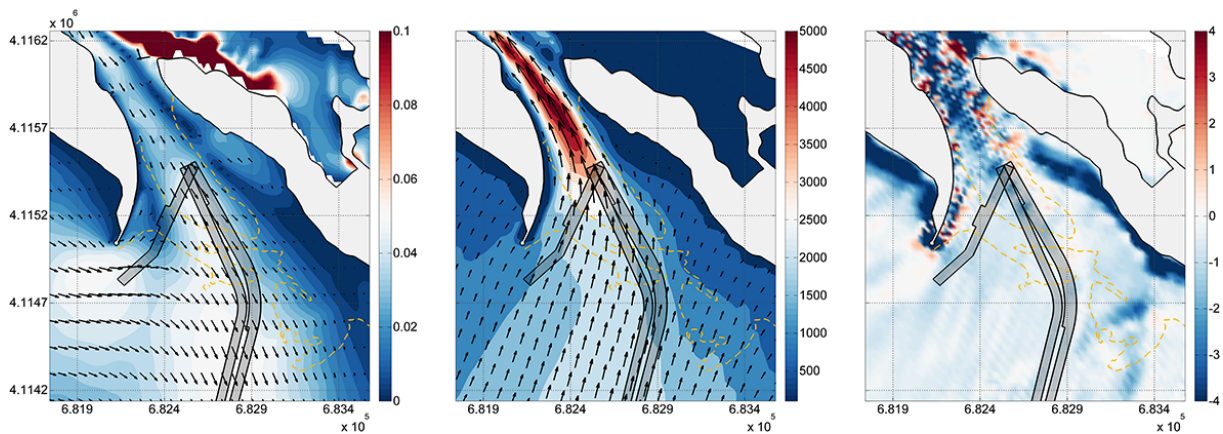


Figure 5.5.2: For the alternative scenario in the PUI: residual currents (in ms^{-1} , panel a), total energy flux $F_{t+w}^{\vec{}}$ (in Wm^{-1} , panel b) and its divergence $\nabla F_{t+w}^{\vec{}}$ (in Wm^{-2} , panel c), where positive colours mean erosion and negative sedimentation tendency.

on Figure 5.4.6 (each channels' bathymetry) to Figure 5.5.2, the proposed alternative reduces the negative gradients inside Cd, Dd and Ud channels a 60, 44 and 45%, respectively.

Then, removing the shoal to a large extent at the entrance of the PUI, instead of the local navigational channels design, will reduce the sedimentation tendency. This alternative, in combination with the morphological activity relationship described in Section 5.4.5, is presented as a more natural-adapted and sustainable strategy.

5.6 Results & Conclusions

The assessment of the evolution of tidal inlet morphodynamics, as a consequence of shifting the regime of natural conditions or due to human activities, is a constant issue in coastal management. Hydrodynamics measurements and 18 detailed bathymetries were used to identify different states of the Punta Umbría inlet. Each state was obtained considering the duration of dredging interventions and the Morphological Activity Index MAI; that is, a value that accounts for the bathymetrical bed-changes in time. The spatial distribution of this index revealed that in the most active zones the MAI is above 1.5 m/year. These locations are not only confined to the navigation channels but to a wider extension in the inlet.

To better understand bathymetric complexities and their interrelation to hydrodynamics, a numerical model was calibrated and validated. Both the tidal \vec{F}_t , and wave energy \vec{F}_w , fluxes were computed. The relative importance of both fields was assessed with the coefficient $F_{t/w} = |\vec{F}_t|/|\vec{F}_w|$. Results showed that the areas where $F_{t/w}$ is above 1.5 are in a close match to the most active zones.

To characterize the sedimentation and erosive bed patterns in the inlet, the divergence of the tidal and wave energy fluxes were related to the morphological activity. A relationship between the observed bed activity and the computed divergence of the energy fluxes was found, where the locations with greater sedimentation tendency correspond to those with larger divergence values.

Thus, this study proposed an alternative management strategy. The current channels designs are in the most active region in the inlet, fitted in a shoaling area. A scenario where this shoal is removed was computed with the numerical model, considering similar forcings to present situation. The results indicate that the divergence of the energy fluxes notably decrease within this scenario, proposing this as a more efficient alternative in the Punta Umbría inlet.

5.A Wave and tidal description

Pressure and level information were recorded in the four current-meters and in the tidal gauge, respectively. The results of a tidal harmonic analysis performed to the elevations signal (Pawlowicz, Beardsley, and Lentz, 2002) are shown in Table 5.A.1:

Table 5.A.1: Amplitude and phase of the elevation in the indicated instruments. Lower-case is the error of the analysis.

AMPLITUDE (cm)	M2	S2	N2	K1	O1	Q1	M4
AQDV	103.60 _{0.6}	27.93 _{0.6}	21.61 _{0.5}	9.81 _{0.3}	6.04 _{0.3}	1.94 _{0.4}	2.20 _{0.2}
AQD1	106.24 _{0.5}	28.51 _{0.5}	22.69 _{0.3}	10.86 _{0.6}	6.54 _{0.7}	2.14 _{0.8}	3.42 _{0.3}
TG1	105.37 _{0.2}	36.60 _{0.2}	24.22 _{0.2}	7.46 _{0.1}	5.65 _{0.6}	1.95 _{0.5}	3.00 _{0.3}
AQD2	109.26 _{1.3}	29.04 _{1.3}	22.90 _{1.1}	10.70 _{1.2}	6.19 _{1.1}	1.31 _{1.2}	4.83 _{0.5}
AQD3	109.04 _{0.8}	28.18 _{0.9}	22.64 _{0.8}	10.53 _{0.2}	5.60 _{0.2}	1.96 _{0.2}	5.78 _{0.8}
PHASE (°)	M2	S2	N2	K1	O1	Q1	M4
AQDV	55.68 _{0.4}	82.89 _{1.15}	49.96 _{1.5}	41.06 _{1.9}	309.13 _{3.2}	266.80 ₁₁	160.08 _{6.1}
AQD1	60.36 _{0.3}	89.40 _{1.25}	54.13 _{1.5}	46.71 _{2.9}	311.71 _{5.2}	275.33 ₂₀	185.81 _{5.4}
TG1	59.58 _{1.0}	90.25 _{3.35}	46.74 _{4.7}	60.88 _{4.2}	315.99 _{5.6}	272.25 ₁₅	189.40 _{6.0}
AQD2	62.05 _{0.7}	92.68 _{2.43}	58.56 _{2.6}	51.23 _{5.9}	319.98 ₁₁	293.02 ₅₈	194.28 _{6.8}
AQD3	63.05 _{0.44}	94.23 _{1.51}	59.04 _{2.0}	55.62 _{0.9}	314.57 _{2.1}	279.29 _{5.4}	202.56 _{7.5}

Values of Table 5.A.1 indicate that Punta Umbría is a mesotidal estuary, where the most

energetic tidal constituent is the semidiurnal M_2 with a period of ≈ 12.42 h.

Wave climate information is depicted in Figure 5.A.1

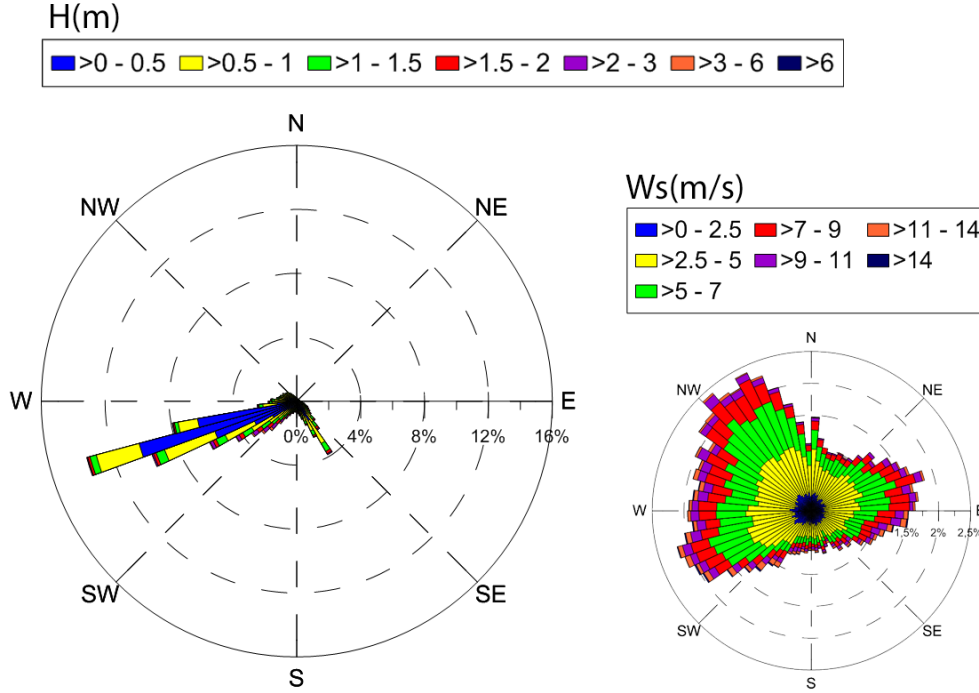


Figure 5.A.1: Wave (H_s , left panel) and Wind (W_s wind speed, right panel) roses in the SIMAR 1052048, located 20 km southwestward the estuary mouth.

5.B Tidal wave interaction: Wave seasonal variability and tidal effects

The present study indicates that, despite different scale, the computed tidal and energy fluxes are representative of mean conditions, thus comparable. To this, the interaction of both fields should be assessed. Then, Wave and Flow module of Delft3D are coupled, re-calibrating and validating both tidal and wave signal. Two wave states and three characteristic tides are selected to run simultaneously during one tidal cycle (12.42h).

The characteristic propagated wave states $[\theta_{ch}, T_{ch}, H_{ch}]$ correspond to winter and summer seasons. Firstly, θ_{ch} is limited to the most frequent value during the season. Then, the characteristic peak period T_{ch} , is the mean of T_s , during the selected interval. As a result, the characteristic wave height H_{ch} , to propagate in the model for the n states during the season is defined as 5.8:

$$H_{ch} = \frac{\sum_{i=1}^n H_s^2 \cdot T_p}{n \cdot T_{ch}} \quad (5.8)$$

Not all the n states from the SIMAR 1052048 are used in Equation 5.8, only the combinations of H_s and T_s that are above the threshold of wave transport for the inlet according to Soulsby (1998). For winter, [$\theta_{ch} = 253^\circ$, $T_{ch}=9.3$ s, $H_{ch}=1.2$ m], while for summer [$\theta_{ch} = 253^\circ$, $T_{ch}=5.5$ s, $H_{ch}=0.5$ m]. The analyzed tides correspond to neap, spring and mean conditions. Choosing as the reference year 2014, three tidal cycles whose tidal range correspond to percentile 5 %, 95 % and 50% were selected.

Then, there are six possible combinations of wave and tidal states. Similar results to those of Section 5.4.4 were computed. For the sake of simplicity and to the aim of this section, only $F_{t/w}$ is shown in Figure 5.B.1. The interaction of tides and waves in different seasons results in different patterns for $F_{t/w}$. The contour line for $F_{t/w}=1$ for the interaction in each scenario (yellow line) is compared to the computed in Figure 5.4.4 (here with gray line), calculated as a ratio of both fields. During winter, tidal influence is closer to the mouth than in summer, due to wave energy. During Summer and with mean and spring tides, the area where the tidal influence is dominant exceed the estuary mouth considerably, spreading at both sides of it.

The same procedure was done with mean tide and the complete wave climate record, with a wave state according to Equation 5.8 of [$\theta_{ch} = 253^\circ$, $T_{ch}=4.5$ s, $H_{ch}=1.0$ m]. Results for $F_{t/w}$ distribution are shown in Figure 5.B.2. It can be observed that the region with $F_{t/w}=1$ are similar in both cases. Values inside this region also behave the same, though in the tidal-wave competition higher values are achieved slightly closer to the mouth with respect to the case of tidal-wave interaction. Despite obvious differences when running the models including coupled hydrodynamics (Figure 5.B.1), the results suggest that tidal-wave competition runs are representative of mean conditions, with a similar distribution to the one that could be obtained with tidal-wave interaction runs (Figure 5.B.2).

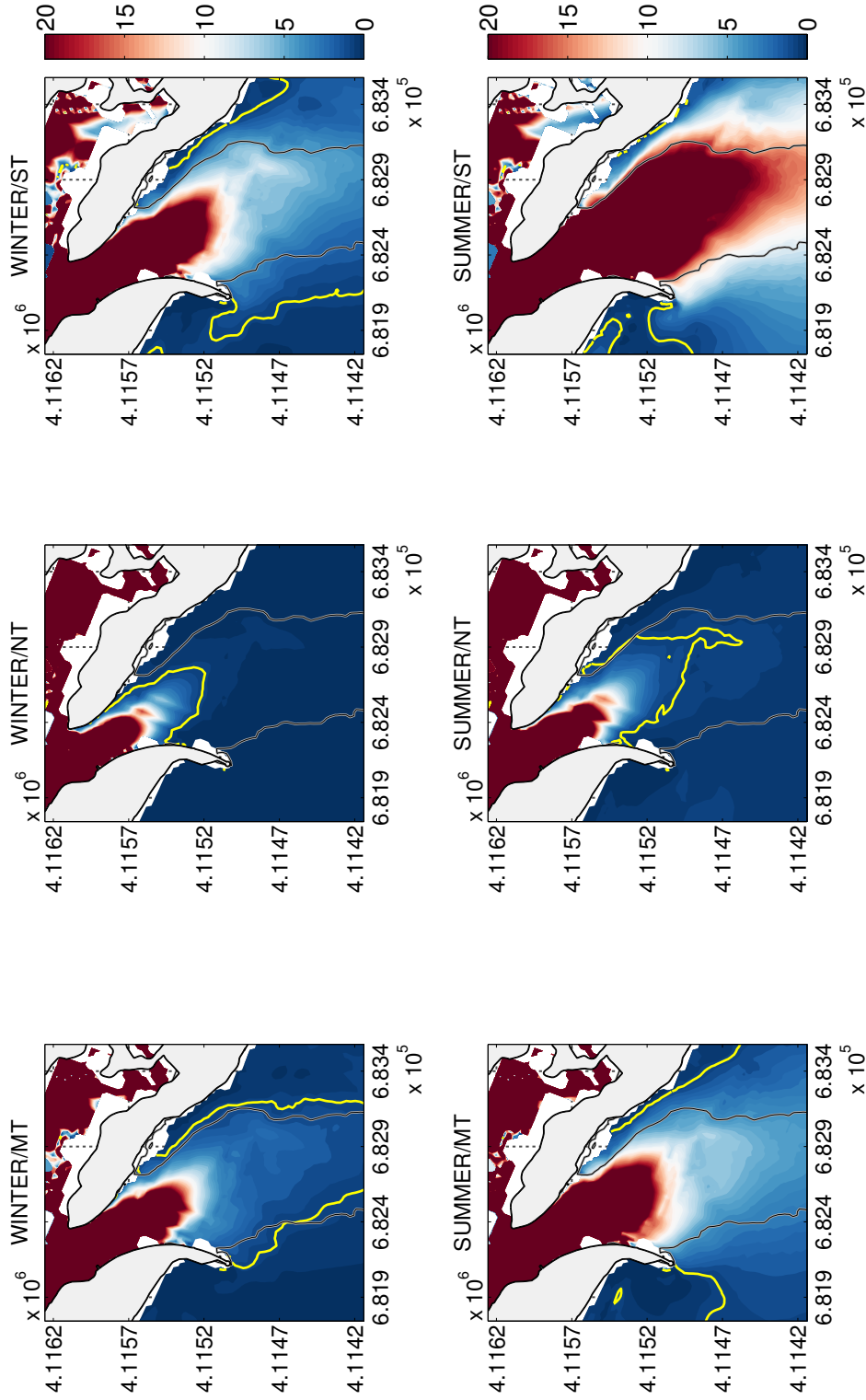


Figure 5.B.1: Relative magnitude $F_{t/w}$ for Winter and Summer wave states and mean (MT), neap (NT) and spring (ST) tides. Each panel is labeled according to the combinations. The color-bar indicate different values for $F_{t/w}$. The yellow line corresponds to $F_{t/w}=1$ for each scenario, while the gray line correspond to the showed in Figure 5.4.4.

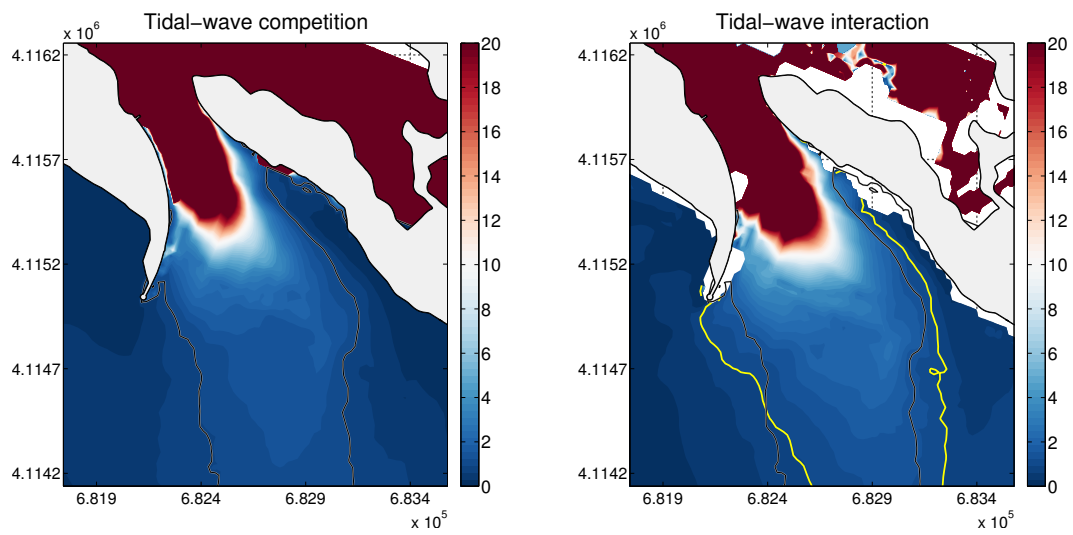


Figure 5.B.2: Relative magnitude $F_{t/w}$ for competed trough tidal-wave competition (Section W, left panel) and tidal-wave interaction with the numerical model (right panel). The color-bar indicate different values for $F_{t/w}$. In both panels, the gray line correspond to the computed $F_{t/w}=1$ showed in Figure 5.4.4. The yellow line in right panel corresponds to the same value but for tidal-wave interaction.

GENERAL CONCLUSIONS AND FUTURE RESEARCH

6.1 General conclusions

Estuaries are crucial areas from environmental and socio-economic point of view. These systems are frequently subjected to dredging interventions, intended to provide access to inland ports. The global assessment of the impact of these activities on the system is still, at present, difficult to quantify and predict. It is the aim of this thesis to develop different techniques, able to quantify and predict the impacts of dredging projects in the main estuarine processes and morphodynamics. Due to the complexity of these processes and their relation with dredging, this assessment should consider multiple spatio-temporal scales.

This section is an overview of the Thesis, gathering the most significant conclusions and results associated with this work. Detailed conclusions are at the end of each Chapter. This study uses the most actual and extended models, implementing and combining techniques of different fields of knowledge, such as those related to estuarine dynamics and statistics. Apart from these, this dissertation incorporates certain forcings in the models to gain physical insight to understand better the effects of management strategies in estuaries, such as deepening navigation channels.

This Thesis is a scientific work based on the current state of knowledge, using multiple techniques to understand, reproduce and simulate the physics of estuaries. Moreover, this work is based on specific measurements and observations of two estuaries of interest for the region of Andalusia: the Guadalquivir estuary and the Punta Umbría inlet. That social and economic relevance, at different scale, is the common link between them; as both the main processes that control their morphodynamics and dredging strategies differ. The Guadalquivir estuary with more than 100 km long, where the dynamics are highly influenced by the freshwater discharge from the head dam and where the complexity of the impacts of dredging projects is related to the presence of multiple stakeholders, contrast to the Punta Umbría inlet. In here, the estuary is relatively small with 6 km long, where the main management concern is related to the navigability through the inlet to inland ports. Also, tidal and wave processes control the morphodynamics. While some of the techniques can be extended to the other area, neither the

forcings, scales, processes nor the length or type of the observations match. Hence, their exchange should be carefully assessed. Therefore, different methodologies were used for each estuary.

In the case of the Guadalquivir, these are highly subjected to freshwater discharge regime, shifting from well mixed under normal conditions to stratified states during high flow regime, particularly closer to the mouth. The derivation of a simple but robust formulation, under common gravitational circulation considerations, enabled the estimation of the eddy viscosity coefficient. Other mechanisms, relative to the saline intrusion, were evaluated with power-law relationships. All previous results pointed the relevance of the freshwater discharge in the estuarine dynamics. Instead of using typical stationary harmonic analysis intended for tidal predictions, non-stationary techniques such as short-time harmonic and wavelet analyses were performed, giving more insight into the physics that govern this interaction. This interaction is relevant in the Guadalquivir estuary, but not in the Punta Umbría inlet, where the influence of the freshwater discharge is minimal. In the Guadalquivir estuary, the analysis revealed that the high sediment concentrations, triggered by discharge events, increase the stratification, shifting the structure of the water column, thus affecting the global morphodynamics of the system, similar to the feed-back loop that occurs in other estuaries after deepening the navigation channel.

To quantify the effect of deepening and other management scenarios in the Guadalquivir, different simulations techniques were used. The management scenarios correspond to a freshwater discharge decrease for the next decades and the deepening of the navigation channel. The models vary from deterministic for tides to non-stationary distributions for river discharge, heuristic Markov process for the saline intrusion and regression models for subtidal water levels and currents. The simulation techniques are Monte Carlo and Markov Chain Monte Carlo methods. The temporal scope for the simulations is, mainly, mid-term. The considered forcings were the freshwater discharge, tidal current amplitude, astronomical tidal range, wind and the deepening of the navigation channel; the latter one by shifting the water depth. The quantified variables were the saline intrusion and the subtidal motion, namely the subtidal water levels. The main advantage of the presented work is that it directly links the observed variables and forcings, considering their stochastic nature when necessary, particularly in the freshwater discharge. Also, the heuristic models are inspired on the observed phenomenology in the Guadalquivir and the simulations are efficient from a computational point of view. In addition, these models highlight the role of each forcing under different conditions, being of potential interest for a scientific and management purpose. Future work could use analytical models, accounting for the main processes revealed with the heuristic models developed in this dissertation, to perform the simulations.

The second study area is the Punta Umbría inlet, in where the main morphodynamics and their relation to dredging projects notably differ from the Guadalquivir estuary. Apart from the role of tides, the occurrence of the dredging interventions in the inlet is triggered by wave climate events. Bathymetric data pointed that not only the effects of dredging interventions but the role of other hydrodynamic processes, should be considered to understand the morphodynamics of the inlet. The requirement to include wave climate, tidal motion and bathymetric complexities, led to the implementation of a numerical model. To that, both the representative tidal and wave energy fluxes were computed and compared, where their ratio enabled the identification of the most active areas in the inlet. This dissertation found that the divergence of these fluxes is the

responsible, to a large extent, of the observed erosion and sedimentation patterns. This energetic approach can be potentially extended to other study areas, including the Guadalquivir estuary. The reason is that different forcings can be properly parameterized by means of energetic terms.

6.2 Future research

The above-mentioned conclusions led to the following lines for future research:

- To include the effects of the suspended matter concentration in the subtidal regression models in the Guadalquivir. This could be achieved with the Richardson number, and assessed from an energetic point of view.
- Tidal-wave interaction runs with the numerical model in the Punta Umbría inlet, including coupled hydrodynamics and morphodynamic module. An analysis to select the adequate number of runs to represent statistically the behaviour of the inlet should be performed, in order to limit the computation time of the simulations. These could be used to compute the evolution in time of the operativity, capacity and sedimentation areas for different dredging designs.

BIBLIOGRAPHY

- Alebregtse, NC and HE de Swart (2016). “Effect of river discharge and geometry on tides and net water transport in an estuarine network, an idealized model applied to the Yangtze Estuary”. In: *Continental Shelf Research* 123, pp. 29–49. DOI: <http://dx.doi.org/10.1016/j.csr.2016.03.028>.
- Álvarez, Manuel Jesús Parodi (2011). “El Guadalquivir: puerta de entrada de civilizaciones”. In: *El río Guadalquivir, del mar a la marisma: Sanlúcar de Barrameda*. Consejería de Obras Públicas y Transportes, pp. 109–117.
- Alvarez, O et al. (1999). “The influence of sediment load on tidal dynamics, a case study: Cádiz Bay”. In: *Estuarine, Coastal and Shelf Science* 48.4, pp. 439–450.
- Athané, José González (2012). “La influencia del río Guadalquivir en la imagen de la ciudad de Sevilla a lo largo de los siglos”. In: *Paisajes modelados por el agua: Entre el arte y la ingeniería*. Editora Regional de Extremadura, pp. 97–109.
- Bagnold, R. A. (1966). “An approach to the sediment transport problem from general physics”. In: *U. S. Geol. Surv. Prof. Pap.* 422-I.
- Banas, NS et al. (2004). “Dynamics of Willapa Bay, Washington: A highly unsteady, partially mixed estuary”. In: *Journal of Physical Oceanography* 34.11, pp. 2413–2427.
- Benjamin, Jack R and C Allin Cornell (2014). *Probability, statistics, and decision for civil engineers*. Courier Corporation.
- Berg, Bernd A (2005). “Introduction to Markov chain Monte Carlo simulations and their statistical analysis”. In: *Markov Chain Monte Carlo, Lect. Not. Ser* 7, p. 1.
- Bertin, Xavier et al. (2005). “Tidal inlet response to sediment infilling of the associated bay and possible implications of human activities: The Marennes-Oléron Bay and the Maumusson Inlet, France”. In: *Continental Shelf Research* 25.9, pp. 1115–1131. ISSN: 02784343. DOI: 10.1016/j.csr.2004.12.004. URL: <http://www.sciencedirect.com/science/article/pii/S0278434305000026>.
- Booij, N., R. C. Ris, and L. H. Holthuijsen (1999). “A third-generation wave model for coastal regions: 1. Model description and validation”. In: *Journal of Geophysical Research: Oceans* 104.C4, pp. 7649–7666. ISSN: 2156-2202. DOI: 10.1029/98JC02622. URL: <http://dx.doi.org/10.1029/98JC02622>.
- Borrego, J (1992). “Sedimentología del estuario del río Odiel (Huelva, SO España)”. PhD thesis. Universidad de Sevilla, Spain.
- Bowden, KF, LA Fairbairn, and P Hughes (1959). “The distribution of shearing stresses in a tidal current”. In: *Geophysical Journal International* 2.4, pp. 288–305.
- Bray, Nick and Marsha Cohen (2010). *Dredging for development*. International Association of Dredging Companies.
- Bray, Richard Nicholas (2008). *Environmental aspects of dredging*. Taylor & Francis.

- Bruun, Per and Franciscus Gerritsen (1966). “Stability of coastal inlets”. In: *Amsterdam: North-Holland Pub. Co.*
- Burchard, Hans and Richard Hofmeister (2008). “A dynamic equation for the potential energy anomaly for analysing mixing and stratification in estuaries and coastal seas”. In: *Estuarine, coastal and shelf Science* 77.4, pp. 679–687.
- Buschman, FA et al. (2009). “Subtidal water level variation controlled by river flow and tides”. In: *Water Resources Research* 45.W10420, p. 12.
- CEDA (2012). *Climate change adaptation as it affects the dredging community*. Central Dredging Association.
- CEDEX (2007). *Materiales de dragado*. Clave 6.1. Centro de Estudios y Experimentación de Obras Públicas.
- (2011). *Evaluación del Impacto del Cambio Climático en los Recursos Hídricos en Régimen Natural*. Centro de Estudios y Experimentación de Obras Públicas, p. 22.
- (2013). *Materiales de dragado*. Clave 6.1. Centro de Estudios y Experimentación de Obras Públicas.
- CJEU (2015). *Judgment in Case C-461/13 Bund für Umwelt und Naturschutz Deutschland eV v Bundesrepublik Deutschland*. Luxembourg.
- Caballero, I et al. (2014). “The influence of the Guadalquivir river on spatio-temporal variability in the pelagic ecosystem of the eastern Gulf of Cádiz”. In: *Mediterranean Marine Science* 15.4, pp. 721–738.
- Cai, Huayang, Marco Toffolon, and Hubert HG Savenije (2016). “An Analytical Approach to Determining Resonance in Semi-Closed Convergent Tidal Channels”. In: *Coastal Engineering Journal*, p. 1650009.
- Camus, Paula et al. (2011). “Analysis of clustering and selection algorithms for the study of multivariate wave climate”. In: *Coastal Engineering* 58.6, pp. 453–462. ISSN: 0378-3839. DOI: 10.1016/j.coastaleng.2011.02.003. URL: <http://www.sciencedirect.com/science/article/pii/S0378383911000354>.
- Carrera-Hernández, JJ and SJ Gaskin (2008). “The Basin of Mexico Hydrogeological Database (BMHDB): Implementation, queries and interaction with open source software”. In: *Environmental Modelling & Software* 23.10, pp. 1271–1279.
- Cayocca, Florence (2001). “Long-term morphological modeling of a tidal inlet: the Arcachon Basin, France”. In: *Coastal Engineering* 42.2, pp. 115–142. ISSN: 0378-3839. DOI: 10.1016/S0378-3839(00)00053-3. URL: <http://www.sciencedirect.com/science/article/pii/S0378383900000533>.
- Chatfield, C (1975). “The analysis of time series: theory and practice”. In: *Chapman Hall*.
- Chawla, Arun and James T Kirby (2002). “Monochromatic and random wave breaking at blocking points”. In: *Journal of Geophysical Research: Oceans (1978–2012)* 107.C7, pp. 4–1.
- Cicin-Sain, Biliiana et al. (1998). *Integrated coastal and ocean management: concepts and practices*. Island Press.
- Coles, Stuart et al. (2001). *An introduction to statistical modeling of extreme values*. Vol. 208. Springer.
- Contreras, E and MJ Polo (2012). “Measurement frequency and sampling spatial domains required to characterize turbidity and salinity events in the Guadalquivir estuary (Spain)”. In: *Natural Hazards and Earth System Sciences* 12.8, pp. 2581–2589.
- Contreras, EP and MJ Polo (2010). “Capítulo 2: Aportes desde las cuencas vertientes”. In: *Propuesta metodológica para diagnosticar y pronosticar las consecuencias de las actuaciones*

- humanas en el estuario del Guadalquivir. Group of Fluvial Dynamic and Hydrology, University of Córdoba, Córdoba.*
- D'Alpaos, Andrea et al. (2009). "On the O'Brien–Jarrett–Marchi law". In: *Rendiconti Lincei* 20.3, pp. 225–236. ISSN: 1720-0776. DOI: 10.1007/s12210-009-0052-x. URL: <http://dx.doi.org/10.1007/s12210-009-0052-x>.
- Dalrymple, Robert W, Brian A Zaitlin, and Ron Boyd (1992). "Estuarine facies models: conceptual basis and stratigraphic implications: perspective". In: *Journal of Sedimentary Research* 62.6.
- De Jonge, VN (1995). "Wind-driven tidal and annual gross transport of mud and microphytobenthos in the Ems Estuary and its importance for the ecosystem". In: *OLSEN & OLSEN, FREDENSBORG, DENMARK*. Pp. 29–40.
- De Swart, H. E. and J. T. F. Zimmerman (2009). "Morphodynamics of Tidal Inlet Systems". In: *Annual Review of Fluid Mechanics* 41.1, pp. 203–229. DOI: 10.1146/annurev.fluid.010908.165159. URL: <http://dx.doi.org/10.1146/annurev.fluid.010908.165159>.
- Dean, Robert G and Robert A Dalrymple (2004). *Coastal processes with engineering applications*. Cambridge University Press. ISBN: 0511037910.
- Dean, Robert George and Robert A Dalrymple (1991). *Water wave mechanics for engineers and scientists*. World Scientific. ISBN: 9810204205.
- Díez-Minguito, M et al. (2013). "Spatio-temporal distribution, along-channel transport, and post-riverflood recovery of salinity in the Guadalquivir estuary (SW Spain)". In: *Journal of Geophysical Research: Oceans* 118.5, pp. 2267–2278.
- Díez-Minguito, M et al. (2014). "Structure of the turbidity field in the Guadalquivir estuary: Analysis of observations and a box model approach". In: *Journal of Geophysical Research: Oceans* 119.10, pp. 7190–7204.
- Díez-Minguito, Manuel et al. (2012). "Tide transformation in the Guadalquivir estuary (SW Spain) and process-based zonation". In: *Journal of Geophysical Research: Oceans (1978–2012)* 117(C3).
- Dissanayake, D. M. P. K., R. Ranasinghe, and J. A. Roelvink (2012). "The morphological response of large tidal inlet/basin systems to relative sea level rise". In: *Climatic Change* 113.2, pp. 253–276. ISSN: 1573-1480. DOI: 10.1007/s10584-012-0402-z. URL: <http://dx.doi.org/10.1007/s10584-012-0402-z>.
- Dronkers, J. (1986). "Tidal asymmetry and estuarine morphology". In: *Netherlands Journal of Sea Research* 20.2, pp. 117–131. ISSN: 0077-7579. DOI: 10.1016/0077-7579(86)90036-0. URL: <http://www.sciencedirect.com/science/article/pii/0077757986900360>.
- Dronkers, JJ (1964). "Tidal computations in rivers and coastal waters". In: *Tidal computations in rivers and coastal waters*. North-Holland.
- Dyer, K. R. (1997). *Estuaries: A physical introduction*. 2nd. John Wiley & Sons, Chichester, UK. ISBN: 0-471-97471-4.
- Eelkema, Menno et al. (2013). "Morphological Effects of the Eastern Scheldt Storm Surge Barrier on the Ebb-Tidal Delta". In: *Coastal Engineering Journal* 55.03, p. 1350010. ISSN: 0578-5634. DOI: 10.1142/S0578563413500101. URL: <http://www.worldscientific.com/doi/10.1142/S0578563413500101>.
- Egbert, Gary D and Svetlana Y Erofeeva (2002). "Efficient inverse modeling of barotropic ocean tides". In: *Journal of Atmospheric and Oceanic Technology* 19.2, pp. 183–204. DOI: 10.1175/1520-0426(2002)019<0183:EIMOB0>2.0.CO;2.
- Elias, E. P. L. and Ad J. F. van der Spek (2006). "Long-term morphodynamic evolution of Texel Inlet and its ebb-tidal delta (The Netherlands)". In: *Marine Geology* 225.1–4, pp. 5–21. ISSN:

- 0025-3227. DOI: 10.1016/j.margeo.2005.09.008. URL: <http://www.sciencedirect.com/science/article/pii/S002532270500304X>.
- Elias, E. P. L. et al. (2006). "Field and model data analysis of sand transport patterns in Texel Tidal inlet (the Netherlands)". In: *Coastal Engineering* 53.5–6, pp. 505–529. ISSN: 0378-3839. DOI: 10.1016/j.coastaleng.2005.11.006. URL: <http://www.sciencedirect.com/science/article/pii/S0378383905001729>.
- Ensing, Erik, Huib E. de Swart, and Henk M. Schuttelaars (2015). "Sensitivity of tidal motion in well-mixed estuaries to cross-sectional shape, deepening, and sea level rise". In: *Ocean Dynamics* 65.7, pp. 933–950. ISSN: 1616-7228. DOI: 10.1007/s10236-015-0844-8. URL: <http://dx.doi.org/10.1007/s10236-015-0844-8>.
- Estévez-Ortega, Juan Carlos (2016). *Evaluación de consecuencias en la hidrodinámica del estuario del Guadalquivir por actuaciones humanas*. Bachelor's thesis. In Spanish.
- Fernández, Juan B Gallego and Francisco García Novo (2007). "High-intensity versus low-intensity restoration alternatives of a tidal marsh in Guadalquivir estuary, SW Spain". In: *Ecological Engineering* 30.2, pp. 112–121.
- Fernández-Delgado, C. et al. (2007). "Effects of the river discharge management on the nursery function of the Guadalquivir river estuary (SW Spain)". In: *Hydrobiologia* 587, pp. 125–136.
- FitzGerald, Duncan M. and Ilya V. Buynevich (2003). "Tidal inlets and deltas". In: *Sedimentology*. Dordrecht: Springer Netherlands, pp. 1219–1224. ISBN: 978-1-4020-3609-5. DOI: 10.1007/978-1-4020-3609-5_237. URL: http://dx.doi.org/10.1007/978-1-4020-3609-5_237.
- Flinchem, EP and DA Jay (2000). "An introduction to wavelet transform tidal analysis methods". In: *Estuarine, Coastal and Shelf Science* 51.2, pp. 177–200.
- Friedrichs, CT, BD Armbrust, and HE De Swart (1998). "Hydrodynamics and equilibrium sediment dynamics of shallow, funnel-shaped tidal estuaries". In: *Physics of Estuaries and Coastal Seas*, pp. 315–327.
- Friedrichs, Carl T. (2010). "Barotropic tides in channelized estuaries". In: *Contemporary Issues in Estuarine Physics*. Ed. by Arnoldo Valle-Levinson. Cambridge University Press, pp. 27–61. ISBN: 9780511676567. DOI: 10.1017/CB09780511676567.004.
- Friedrichs, Carl T. and David G. Aubrey (1988). "Non-linear tidal distortion in shallow well-mixed estuaries: a synthesis". In: *Estuarine, Coastal and Shelf Science* 27.5, pp. 521–545. ISSN: 0272-7714. DOI: 10.1016/0272-7714(88)90082-0. URL: <http://www.sciencedirect.com/science/article/pii/0272771488900820>.
- Friedrichs, Carl T and Ole S Madsen (1992). "Nonlinear diffusion of the tidal signal in frictionally dominated embayments". In: *Journal of Geophysical Research* 97.N3C4, pp. 5637–5650.
- Gallo, Marcos Nicolás and Susana Beatriz Vinzon (2005). "Generation of overtides and compound tides in Amazon estuary". In: *Ocean Dynamics* 55.5-6, pp. 441–448.
- García-Contreras, Darío (2009). "Estuario del Guadalquivir: tramificación, pérdidas de carga y modelo lineal de propagación de onda de marea". In Spanish. MA thesis. University of Granada.
- García-Lafuente, Jesús et al. (2012). "About the tidal oscillations of temperature in a tidally driven estuary: The case of Guadalquivir estuary, southwest Spain". In: *Estuarine, Coastal and Shelf Science* 111, pp. 60–66.
- General Secretary of the Environment (2003). *Resolution of 26 September 2003, the General Secretariat of the Environment, for Which Environmental Impact Statement on the -Actions to Improve Access Port Maritime of Seville Formula- Project*. Seville, Spain.

- Geyer, W. R. (2010). “Contemporary Issues in Estuarine Physics”. In: ed. by A. Valle-Levinson. Cambridge University Press, New York. Chap. Estuarine salinity structure and circulation, pp. 12–26.
- Geyer, W Rockwell (1993). “The importance of suppression of turbulence by stratification on the estuarine turbidity maximum”. In: *Estuaries* 16.1, pp. 113–125.
- Geyer, W Rockwell and Heidi Nepf (1996). “Tidal pumping of salt in a moderately stratified estuary”. In: *Buoyancy Effects on Coastal and Estuarine Dynamics*, pp. 213–226.
- Giese, BS and DA Jay (1989). “Modelling tidal energetics of the Columbia River estuary”. In: *Estuarine, Coastal and Shelf Science* 29.6, pp. 549–571.
- Girard, Albert (2006). *La rivalidad comercial y marítima entre Sevilla y Cádiz: hasta finales del siglo XVIII*. Vol. 4. Editorial Renacimiento.
- Godin, G (1999). “The propagation of tides up rivers with special considerations on the upper Saint Lawrence River”. In: *Estuarine, Coastal and Shelf Science* 48.3, pp. 307–324.
- Godin, Gabriel (1983). “On the predictability of currents”. In: *International Hydrographic Review*. — (1985). “Modification of river tides by the discharge”. In: *Journal of Waterway, Port, Coastal, and Ocean Engineering* 111.2, pp. 257–274. — (1991). “Frictional effects in river tides”. In: *Tidal hydrodynamics* 379, p. 402.
- Godin, Gabriel and Guillermo Gutiérrez (1986). “Non-linear effects in the tide of the Bay of Fundy”. In: *Continental Shelf Research* 5.3, pp. 379–402.
- Gómez-Enri, J et al. (2015). “Heavy Guadalquivir River discharge detection with satellite altimetry: The case of the eastern continental shelf of the Gulf of Cadiz (Iberian Peninsula)”. In: *Advances in Space Research* 55.6, pp. 1590–1603.
- Granado-Lorencio, Carlos (1991). “The effect of man on the fish fauna of the River Guadalquivir, Spain”. In: *Fisheries research* 12.2, pp. 91–100.
- Grimmett, Geoffrey and David Stirzaker (2001). *Probability and random processes*. Oxford university press.
- Grinsted, Aslak, John C Moore, and Svetlana Jevrejeva (2004). “Application of the cross wavelet transform and wavelet coherence to geophysical time series”. In: *Nonlinear Processes in Geophysics* 11.5/6, pp. 561–566.
- Grunnet, Nicholas M., B. G. Ruessink, and Dirk-Jan R. Walstra (2005). “The influence of tides, wind and waves on the redistribution of nourished sediment at Terschelling, The Netherlands”. In: *Coastal Engineering* 52.7, pp. 617–631. ISSN: 0378-3839. DOI: 10.1016/j.coastaleng.2005.04.001. URL: <http://www.sciencedirect.com/science/article/pii/S0378383905000463>.
- Guerreiro, Catarina et al. (2013). “The role of estuarine discharges on the biogeochemical characteristics of the nearby continental shelf ecosystem. The Guadalquivir-Gulf of Cádiz case study”. In: *EGU General Assembly Conference Abstracts*. Vol. 15, p. 8361.
- Guo, Leicheng et al. (2015). “River-tide dynamics: Exploration of nonstationary and nonlinear tidal behavior in the Yangtze River estuary”. In: *Journal of Geophysical Research: Oceans* 120.5, pp. 3499–3521.
- Gust, Giseller and Eckart Walger (1976). “The influence of suspended cohesive sediments on boundary-layer structure and erosive activity of turbulent seawater flow”. In: *Marine Geology* 22.3, pp. 189–206.
- Hansen, Donald V and Maurice Rattray (1966). “New dimensions in estuary classification”. In: *Limnology and Oceanography*, pp. 319–326.

- Herckenrath, Daan, Christian D Langevin, and John Doherty (2011). “Predictive uncertainty analysis of a saltwater intrusion model using null-space Monte Carlo”. In: *Water Resources Research* 47.5.
- Hibma, A., M. J. F. Stive, and Z. B. Wang (2004). “Estuarine morphodynamics”. In: *Coastal Engineering* 51.8–9. Coastal Morphodynamic Modeling, pp. 765–778. ISSN: 0378-3839. DOI: 10.1016/j.coastaleng.2004.07.008. URL: <http://www.sciencedirect.com/science/article/pii/S037838390400081X>.
- Hoitink, A. J. F. and D. A. Jay (2016). “Tidal river dynamics: Implications for deltas”. In: *Reviews of Geophysics* 54.1, pp. 240–272. DOI: 10.1002/2015RG000507.
- Horrevoets, AC et al. (2004). “The influence of river discharge on tidal damping in alluvial estuaries”. In: *Journal of Hydrology* 294.4, pp. 213–228.
- IADC (2014). *Dredging in figures*. International Association of Dredging Companies.
- (2015). *Beyond sand & sea*. The Hague, The Netherlands: International Association of Dredging Companies.
- Jalón-Rojas, Isabel et al. (2016). “Tracking the turbidity maximum zone in the Loire Estuary (France) based on a long-term, high-resolution and high-frequency monitoring network”. In: *Continental Shelf Research* 117, pp. 1–11.
- Jäppinen, Sakari, Tuuli Toivonen, and Maria Salonen (2013). “Modelling the potential effect of shared bicycles on public transport travel times in Greater Helsinki: An open data approach”. In: *Applied Geography* 43, pp. 13–24.
- Jarret, JT (1976). “Tidal prism inlet area relationships. GITI Report 3”. In: *US Army Coastal Engineering Research Center*.
- Jassby, Alan D et al. (1995). “Isohaline position as a habitat indicator for estuarine populations”. In: *Ecological Applications* 5.1, pp. 272–289.
- Jay, David A and Edward P Flinchem (1997). “Interaction of fluctuating river flow with a barotropic tide: A demonstration of wavelet tidal analysis methods”. In: *Journal of Geophysical Research: Oceans (1978–2012)* 102.C3, pp. 5705–5720.
- Jay, David A and Jeffery D Musiak (1994). “Particle trapping in estuarine tidal flows”. In: *Journal of Geophysical Research: Oceans* 99.C10, pp. 20445–20461.
- Jay, David A et al. (2014). “Tidal-fluvial and estuarine processes in the lower Columbia River: I. Along-channel water level variations, Pacific Ocean to Bonneville Dam”. In: *Estuaries and Coasts* 38.2, pp. 415–433.
- Jianqing Fan, Qiwei Yao (2005). *Nonlinear Time Series. Nonparametric and Parametric Methods*. 1st ed. Springer Science.
- Jonge, Victor N de et al. (2014). “The influence of channel deepening on estuarine turbidity levels and dynamics, as exemplified by the Ems estuary”. In: *Estuarine, Coastal and Shelf Science* 139, pp. 46–59.
- Kineke, GC et al. (1996). “Fluid-mud processes on the Amazon continental shelf”. In: *Continental Shelf Research* 16.5, pp. 667–696.
- King, B and E Wolanski (1996). “Bottom friction reduction in turbid estuaries”. In: *Mixing in Estuaries and Coastal Seas*, pp. 325–337.
- Kottegoda, Nathabandu T and Renzo Rosso (2008). *Applied statistics for civil and environmental engineers*. Blackwell Chichester, UK.
- Kukulka, Tobias and David A Jay (2003). “Impacts of Columbia River discharge on salmonid habitat: 2. Changes in shallow-water habitat”. In: *Journal of Geophysical Research: Oceans (1978–2012)* 108.C9.

- Laiz, I et al. (2013). “Seasonal sea level variations in the gulf of Cadiz continental shelf from in-situ measurements and satellite altimetry”. In: *Continental Shelf Research* 53, pp. 77–88.
- Laiz, Irene et al. (2015). “Steric contribution to the long-term sea level variations within the Gulf of Cadiz continental shelf”. In: *EGU General Assembly Conference Abstracts*. Vol. 17, p. 3577.
- (2016). “Contributions to the sea level seasonal cycle within the Gulf of Cádiz (Southwestern Iberian Peninsula)”. In: *Journal of Marine Systems*. DOI: <http://dx.doi.org/10.1016/j.jmarsys.2016.03.006>.
- Lanzoni, Stefano and Giovanni Seminara (1998). “On tide propagation in convergent estuaries”. In: *Journal of Geophysical Research* 103.C13, pp. 30–793.
- (2002). “Long-term evolution and morphodynamic equilibrium of tidal channels”. In: *Journal of Geophysical Research: Oceans* 107.C1, pp. 1–1–1–13. ISSN: 2156-2202. DOI: 10.1029/2000JC000468. URL: <http://dx.doi.org/10.1029/2000JC000468>.
- Lario, Javier (1996). “Último y Presente Interglacial en el área de conexión Atlántico-Mediterráneo: variaciones del nivel del mar, paleoclima y paleoambientes”. In: (*Ph. D. Thesis*) *Universidad Complutense de Madrid, Spain*.
- Le Provost, Christian (1991). *Generation of overtides and compound tides, review*. John Wiley & Sons.
- LeBlond, Paul H (1978). “On tidal propagation in shallow rivers”. In: *Journal of Geophysical Research: Oceans* 83.C9, pp. 4717–4721.
- (1979). “Forced fortnightly tides in shallow rivers”. In: *Atmosphere-ocean* 17.3, pp. 253–264.
- Lerczak, James A, W Rockwell Geyer, and David K Ralston (2009). “The temporal response of the length of a partially stratified estuary to changes in river flow and tidal amplitude”. In: *Journal of Physical Oceanography* 39.4, pp. 915–933.
- Lesser, G. R. et al. (2004). “Development and validation of a three-dimensional morphological model”. In: *Coastal Engineering* 51.8–9. Coastal Morphodynamic Modeling, pp. 883–915. ISSN: 0378-3839. DOI: 10.1016/j.coastaleng.2004.07.014. URL: <http://www.sciencedirect.com/science/article/pii/S0378383904000870>.
- Losada, Miguel Ángel (2011). “La puerta del mar”. In: *El río Guadalquivir, del mar a la marisma: Sanlúcar de Barrameda*. Consejería de Obras Públicas y Transportes, pp. 28–35.
- MacCready, Parker (2004). “Toward a unified theory of tidally-averaged estuarine salinity structure”. In: *Estuaries* 27.4, pp. 561–570.
- MacWilliams, Michael L et al. (2015). “Three-Dimensional Modeling of Hydrodynamics and Salinity in the San Francisco Estuary: An Evaluation of Model Accuracy, X2, and the Low-Salinity Zone”. In: *San Francisco Estuary and Watershed Science* 13.1.
- Magaña, Pedro (2015). “Knowledge representation in the domain of environmental dynamics”. PhD thesis. University of Granada.
- Magaña, Pedro et al. (2014). “A public, open Western Europe database of shoreline undulations based on imagery”. In: *Applied Geography* 55, pp. 278–291.
- Maren, D. S. van et al. (2015). “The impact of channel deepening and dredging on estuarine sediment concentration”. In: *Continental Shelf Research* 95, pp. 1–14. ISSN: 0278-4343. DOI: 10.1016/j.csr.2014.12.010. URL: <http://www.sciencedirect.com/science/article/pii/S0278434314003720>.
- Maren, Dirk S van, Johan C Winterwerp, and Julia Vroom (2015). “Fine sediment transport into the hyper-turbid lower Ems River: the role of channel deepening and sediment-induced drag reduction”. In: *Ocean Dynamics* 65.4, pp. 589–605.
- Masselink, Gerd and Roland Gehrels (2014). *Coastal environments and global change*. John Wiley & Sons.

- Matte, Pascal, Yves Secretan, and Jean Morin (2014). “Temporal and spatial variability of tidal-fluvial dynamics in the St. Lawrence fluvial estuary: An application of nonstationary tidal harmonic analysis”. In: *Journal of Geophysical Research: Oceans* 119.9, pp. 5724–5744.
- McCool, Jon-Paul P (2014). “PRAGIS: a test case for a web-based archaeological GIS”. In: *Journal of Archaeological Science* 41, pp. 133–139.
- Meade, Robert H (1969). “Landward transport of bottom sediments in estuaries of the Atlantic coastal plain”. In: *Journal of Sedimentary Research* 39.1.
- Medio Ambiente, Agencia Andaluza. Consejería de (2009). *Boletín del Estuario del Guadalquivir*. Newsletter.
- Mink, Frederik et al. (2006). “Impact of European Union environmental law on dredging”. In: *Terra et Aqua* 104, p. 3.
- Monismith, S. G. et al. (2002). “Structure and flow-induced variability of the subtidal salinity field in northern San Francisco bay”. In: *Journal of Physical Oceanography* 32, pp. 3003–3019.
- Morales, Juan A., José Borrego, and Richard A. Davis Jr. (2014). “A new mechanism for chenier development and a facies model of the Saltés Island chenier plain (SW Spain)”. In: *Geomorphology* 204, pp. 265–276. ISSN: 0169-555X. DOI: 10.1016/j.geomorph.2013.08.011. URL: <http://www.sciencedirect.com/science/article/pii/S0169555X13004169>.
- Moreno, Isabel María, Alberto Ávila, and Miguel Ángel Losada (2010). “Morphodynamics of intermittent coastal lagoons in Southern Spain: Zahara de los Atunes”. In: *Geomorphology* 121.3–4, pp. 305–316. ISSN: 0169-555X. DOI: 10.1016/j.geomorph.2010.04.028. URL: <http://www.sciencedirect.com/science/article/pii/S0169555X10002199>.
- Navarro, G. et al. (2011). “Temporal and spatial variability in the Guadalquivir Estuary: A challenge for real-time telemetry”. In: *Ocean Dynamics* 61.6, pp. 753–765.
- Navarro, Gabriel et al. (2012). “Use of a real-time remote monitoring network (RTRM) to characterize the Guadalquivir estuary (Spain)”. In: *Sensors* 12.2, pp. 1398–1421.
- O’Brien, Morrrough P (1931). “Estuary Tidal Prisms Related to Entrance Areas”. In: *Civil Engineering* 1.8, pp. 738–739.
- (1969). “Equilibrium flow areas of tidal inlets on sandy coasts”. In: *J. Waterw. Port Coast. Ocean Eng.* Pp. 43–52. ISSN: 2156-1028.
- Ortega-Sánchez, M et al. (2014). “The influence of shelf-indenting canyons and infralittoral prograding wedges on coastal morphology: The Carchuna system in Southern Spain”. In: *Marine Geology* 347, pp. 107–122.
- Padilla, Enrique M et al. (2015). “A Subtidal Model of Temperature for a Well-Mixed Narrow Estuary: the Guadalquivir River Estuary (SW Spain)”. In: *Estuaries and Coasts*, pp. 1–16.
- Parker, Bruce B (1991). “The relative importance of the various nonlinear mechanisms in a wide range of tidal interactions”. In: *Tidal hydrodynamics*, pp. 237–268.
- Pawlowicz, Rich, Bob Beardsley, and Steve Lentz (2002). “Classical tidal harmonic analysis including error estimates in MATLAB using T_TIDE”. In: *Computers & Geosciences* 28.8, pp. 929–937. ISSN: 0098-3004. DOI: 10.1016/S0098-3004(02)00013-4. URL: <http://www.sciencedirect.com/science/article/pii/S0098300402000134>.
- Peregrine, DH (1976). “Interaction of water waves and currents”. In: *Advances in Applied Mechanics*. 16, pp. 9–117.
- Prandle, D and M Rahman (1980). “Tidal response in estuaries”. In: *Journal of Physical Oceanography* 10.10, pp. 1552–1573.
- Prumm, Matthew and Gregorio Iglesias (2016). “Impacts of port development on estuarine morphodynamics: Ribadeo (Spain)”. In: *Ocean & Coastal Management* 130, pp. 58–72. ISSN:

- 0964-5691. DOI: 10.1016/j.ocecoaman.2016.05.003. URL: <http://www.sciencedirect.com/science/article/pii/S096456911630093X>.
- Rabobank (2013). *Dredging; Profit margins expected to remain fairly healthy until 2018*.
- Ralston, David K, W Rockwell Geyer, and James A Lerczak (2010). "Structure, variability, and salt flux in a strongly forced salt wedge estuary". In: *Journal of Geophysical Research: Oceans* 115.C6.
- Reyes-Merlo, Miguel Ángel et al. (2015). "Morphodynamic evolution and influence of dredging activities in small-scale mesotidal estuaries: the case of Punta Umbría (Southwestern Spain)". In: *Proceedings of the 36th IAHR-International Association for Hydro-Environment Engineering and Research World Congress*. URL: <http://89.31.100.18/~iahrpapers/87184.pdf>.
- Ridderinkhof, Wim et al. (2014). "Influence of the back-barrier basin length on the geometry of ebb-tidal deltas". In: *Ocean Dynamics* 64.9, pp. 1333–1348. ISSN: 1616-7228. DOI: 10.1007/s10236-014-0744-3. URL: <http://dx.doi.org/10.1007/s10236-014-0744-3>.
- Rioul, Olivier and Martin Vetterli (1991). "Wavelets and signal processing". In: *IEEE signal processing magazine* 8.LCAV-ARTICLE-1991-005, pp. 14–38.
- Rodríguez Vidal, J. (1987). "Recent geomorphological evolution in the Ayamonte-Mazagon sector of the south Atlantic coast (Huelva, Spain)". In: *Trab.Neóg.Cuatern.* 10, pp. 259–264. URL: www.scopus.com.
- Rozenstein, Offer and Arnon Karnieli (2011). "Comparison of methods for land-use classification incorporating remote sensing and GIS inputs". In: *Applied Geography* 31.2, pp. 533–544.
- Ruiz, J. and Miguel Á Losada (2010). *Propuesta metodológica para diagnosticar y pronosticar las consecuencias de las actuaciones humanas en el estuario del Guadalquivir*. Tech. rep. Universidad de Córdoba (UCO) y Universidad de Granada (UGR) bajo los auspicios Andalucía (CSIC).
- Ruiz, J et al. (2013). "A simple biogeochemical model for estuaries with high sediment loads: Application to the Guadalquivir River (SW Iberia)". In: *Ecological Modelling* 265, pp. 194–206.
- Ruiz, Javier et al. (2015). "The Guadalquivir estuary: a hot spot for environmental and human conflicts". In: *Environmental Management and Governance*. Springer, pp. 199–232.
- Sassi, MG and AJF Hoitink (2013). "River flow controls on tides and tide-mean water level profiles in a tidal freshwater river". In: *Journal of Geophysical Research: Oceans* 118.9, pp. 4139–4151.
- Savenije, H.H.G. (1993). "Predictive model for salt intrusion in estuaries". In: *J. Hydrol.* 148.1-4, pp. 203–218.
- Savenije, Hubert H. G. (2005). *Salinity and tides in alluvial estuaries*. Elsevier. ISBN: 978-0-444-52107-1.
- Savenije, Hubert HG and Ed JM Veling (2005). "Relation between tidal damping and wave celerity in estuaries". In: *Journal of Geophysical Research: Oceans* 110.C4.
- Savenije, Hubert HG et al. (2008). "Analytical description of tidal dynamics in convergent estuaries". In: *Journal of Geophysical Research: Oceans (1978–2012)* 113.C10.
- Schuttelaars, H M and H E de Swart (1996). "An idealized long term morphodynamic model of a tidal embayment". In: *Eur. J. Mech., B/Fluids* 15, pp. 55–80. ISSN: 09977546.
- Scully, Malcolm E, Carl Friedrichs, and John Brubaker (2005). "Control of estuarine stratification and mixing by wind-induced straining of the estuarine density field". In: *Estuaries* 28.3, pp. 321–326.
- Sheehan, C, J Harrington, and JD Murphy (2010). "An environmental and economic assessment of topsoil production from dredge material". In: *Resources, Conservation and Recycling* 55.2, pp. 209–220.

- Simpson, JH, R Vennell, and AJ Souza (2001). "The salt fluxes in a tidally-energetic estuary". In: *Estuarine, Coastal and Shelf Science* 52.1, pp. 131–142.
- Solari, S and MA Losada (2011). "Non-stationary wave height climate modeling and simulation". In: *Journal of Geophysical Research: Oceans* 116.C9.
- Solari, Sebastián (2011). "Metodologías de simulación de agentes naturales y desarrollo de sistemas. Modelo de verificación y gestión de terminales portuarias. Aplicación al puerto de la Bahía de Cádiz". PhD thesis. University of Granada. ISBN: 9788469511657. URL: <http://hdl.handle.net/10481/20322>.
- Soulsby, Richard (1997). *Dynamics of marine sands: a manual for practical applications*. Thomas Telford.
- (1998). "Dynamics of Marine Sands (HR Wallingford Titles): A Manual for Practical Applications". In:
- Souza, AJ and JH Simpson (1996). "The modification of tidal ellipses by stratification in the Rhine ROFI". In: *Continental Shelf Research* 16.8, pp. 997–1007.
- Speer, PE and DG Aubrey (1985). "A study of non-linear tidal propagation in shallow inlet/estuarine systems Part II: Theory". In: *Estuarine, Coastal and Shelf Science* 21.2, pp. 207–224.
- Stive, Marcel J. F. and Z. B. Wang (2003). "Chapter 13 Morphodynamic modeling of tidal basins and coastal inlets". In: *Advances in Coastal Modeling*. Ed. by V. C. Lakhan. Vol. 67. Elsevier Oceanography Series. Elsevier, pp. 367–392. DOI: 10.1016/S0422-9894(03)80130-7. URL: <http://www.sciencedirect.com/science/article/pii/S0422989403801307>.
- Supreme Court (2015). *Chamber of Administrative Litigation Section. Fourth Sentence, Judicial Review. Challenging Hydrological Plan the Guadalquivir River Basin. Nullity of dredging Channel of the Port of Seville and His Character as a Complementary Measure*. Madrid, Spain.
- Talke, Stefan A, Huib E de Swart, and HM Schuttelaars (2009). "Feedback between residual circulations and sediment distribution in highly turbid estuaries: An analytical model". In: *Continental Shelf Research* 29.1, pp. 119–135.
- The European Commission (2009). *Estuaries and coastal zones within the context of the Birds and Habitats Directives*.
- (2012). *Port development and dredging in Natura 2000 estuaries and coastal zones*. DOI: 10.2779/8414.
- Torrence, Christopher and Gilbert P Compo (1998). "A practical guide to wavelet analysis". In: *Bulletin of the American Meteorological society* 79.1, pp. 61–78.
- Uncles, R.J., R.C.A. Elliott, and S.A. Weston (1985). "Observed fluxes of water, salt and suspended sediment in a partly mixed estuary". In: *Estuarine, Coastal and Shelf Science* 20.2, pp. 147–167. ISSN: 0272-7714. DOI: [http://dx.doi.org/10.1016/0272-7714\(85\)90035-6](http://dx.doi.org/10.1016/0272-7714(85)90035-6). URL: <http://www.sciencedirect.com/science/article/pii/0272771485900356>.
- Valle-Levinson, Arnaldo (2010). *Contemporary issues in estuarine physics*. Cambridge University Press.
- Van Rijn, Leo C. (2005). "Estuarine and coastal sedimentation problems". In: *International Journal of Sediment Research* 20.1, pp. 39–51. ISSN: 10016279 (ISSN).
- Vanderostyne, Mon and Marsha Cohen (1999). "From hand-drag to jumbo: A millennium of dredging". In: *Terra et Aqua* 77, pp. 1–48.
- Vanney, Jean-René (1970). *L'hydrologie du bas Guadalquivir*. Inst. de Geografía Aplicada.
- Vargas, Jesús and Pilar Paneque (2015). "Major Hydraulic Projects, Coalitions and Conflict. Seville's Harbour and the Dredging of the Guadalquivir (Spain)". In: *Water* 7.12, pp. 6736–6749.

- Wang, Z. B., T. Louters, and H. J. de Vriend (1995). "Large-Scale Coastal Behavior Morphodynamic modelling for a tidal inlet in the Wadden Sea". In: *Marine Geology* 126.1, pp. 289–300. ISSN: 0025-3227. DOI: 10.1016/0025-3227(95)00083-B. URL: <http://www.sciencedirect.com/science/article/pii/002532279500083B>.
- Wang, Z.B et al. (2002). "Morphology and asymmetry of the vertical tide in the Westerschelde estuary". In: *Continental Shelf Research* 22.17, pp. 2599–2609. ISSN: 0278-4343. DOI: [http://dx.doi.org/10.1016/S0278-4343\(02\)00134-6](http://dx.doi.org/10.1016/S0278-4343(02)00134-6). URL: <http://www.sciencedirect.com/science/article/pii/S0278434302001346>.
- Wang, Zheng Bing and Mario Fernández Bermejo (2010). "Impact of fluvial sediment input to tidal amplification in an estuary". In: *EGU general assembly conference abstracts*. Vol. 12, p. 4868.
- Wang, Zheng Bing, Johan C Winterwerp, and Qing He (2014). "Interaction between suspended sediment and tidal amplification in the Guadalquivir Estuary". In: *Ocean Dynamics* 64.10, pp. 1487–1498.
- Warner, John C, W Rockwell Geyer, and James A Lerczak (2005). "Numerical modeling of an estuary: A comprehensive skill assessment". In: *Journal of Geophysical Research: Oceans* 110.C5.
- Wegen, M. van der and J. A. Roelvink (2008). "Long-term morphodynamic evolution of a tidal embayment using a two-dimensional, process-based model". In: *Journal of Geophysical Research: Oceans* 113.C3. C03016. ISSN: 2156-2202. DOI: 10.1029/2006JC003983. URL: <http://dx.doi.org/10.1029/2006JC003983>.
- Willmott, Cort J. (1981). "On the validation of models". In: *Physical Geography* 2.2, pp. 184–194. DOI: 10.1080/02723646.1981.10642213. URL: <http://www.tandfonline.com/doi/abs/10.1080/02723646.1981.10642213>.
- Winterwerp, Johan C, Marieke Lely, and Qing He (2009). "Sediment-induced buoyancy destruction and drag reduction in estuaries". In: *Ocean Dynamics* 59.5, pp. 781–791.
- Winterwerp, Johan C. and Zheng Bing Wang (2013). "Man-induced regime shifts in small estuaries - I: Theory". In: *Ocean Dynamics* 63.11, pp. 1279–1292. ISSN: 1616-7228. DOI: 10.1007/s10236-013-0662-9. URL: <http://dx.doi.org/10.1007/s10236-013-0662-9>.
- Zaruelo, Carmen et al. (2015). "Hydrodynamics response to planned human interventions in a highly altered embayment: The example of the Bay of Cádiz (Spain)". In: *Estuarine, Coastal and Shelf Science* 167, Part A, pp. 75–85. ISSN: 0272-7714. DOI: 10.1016/j.ecss.2015.07.010. URL: <http://www.sciencedirect.com/science/article/pii/S0272771415300184>.
- Zentar, R et al. (2009). "Beneficial use of dredged sediments in public works". In: *Environmental technology* 30.8, pp. 841–847.
- Zhang, Lijing and Jing Yi (2010). "Management methods of spatial data based on postgis". In: *Circuits, Communications and System (PACCS), 2010 Second Pacific-Asia Conference on*. Vol. 1. IEEE, pp. 410–413.
- Zhong, Liejun and Ming Li (2006). "Tidal energy fluxes and dissipation in the Chesapeake Bay". In: *Continental Shelf Research* 26.6, pp. 752–770. ISSN: 0278-4343. DOI: 10.1016/j.csr.2006.02.006. URL: <http://www.sciencedirect.com/science/article/pii/S0278434306000410>.